# Effect of Strain Rate on Adhesively Bonded Lap Joints with Similar and Dissimilar Adherends

**by**

**Sree Sruthi Modala**

**A thesis submitted in partial fulfillment**
**of the requirements for the degree of**
**Master of Science in Engineering**
**(Mechanical Engineering)**
**in the University of Michigan-Dearborn**
**2019**

**Master's Thesis Committee:**

**Associate Professor German Reyes-Villanueva, Chair**
**Professor Hong-Tae Kang**
**Assistant Professor Tanjore V Jayaraman**

# Dedication

To my family, Dr. Venugopal Modala, Mrs. Padmaja Sanigepalli
Pooja Modala, Keerthivasan and Viaan Vasan
For their loving support

## Acknowledgements

I would first like to thank my thesis advisor German Reyes-Villanueva for being a tremendous mentor for me. I would like to thank him for giving me this opportunity to pursue my research interest and for motivating me throughout my research period. I owe special depth of gratitude to him for his rich expertise and his encouragement throughout the work and its successful completion.

I would like to thank Dr. Tanjore V. Jayaraman for taking time to evaluate my thesis and for creating a room of enthusiasm, appreciation for growing during my Master's tenure. I would also like to thank Dr. Hong-Tae Kang for taking time to evaluate my thesis and for being a part of the thesis committee.

I would like to express my profound gratitude to my parents and siblings for their unfailing support and encouragement throughout my thesis. I would like to thank my father who introduced me to the world of materials and helped in every possible way to make my life easier during my master's career. His every experience and knowledge shared with me, really helped me to get insights about my research. I would like to express my appreciation to my work partner Saikanth for his utter care for me. Through working together over the last two years, he has become one of my very dearest friends. He deserves enormous credit for putting up with me and all my quirks. I would like to thank Mallik Pariti who helped and encouraged at every hardship faced during the thesis. He is the best senior I could ever ask for. I also would like to thank the office staff of the mechanical engineering department whose assistance helped me along the way. Also, to my friends: Rakesh, Sandeep, Tejaswini, Sandhya, and Manasa and my seniors at UM-Dearborn for all the good times we had and being tolerant enough during my two years at the graduate school.

# Table of Contents

# List of Figures

# List of Tables

# Abstract

Adhesively bonded joints provide several benefits, such as uniform stress distribution than conventional methods such as mechanical fastening. Hence, the knowledge of stresses inside the adhesive layer of an adhesively-bonded joint is essential for design analysis and joint strength prediction. In this thesis, the effect of strain rate on adhesively bonded single lap joints of similar and dissimilar adherends (Aluminum and Carbon fiber composites) with a number of adhesives was investigated. The experiments were conducted based on three different sets of substrate combinations that included 1) Al6061 – Al6061, 2) Al6061–CFRP and, 3) CFRP-CFRP using three different adhesives that included a high strength epoxy, a quick set epoxy, and a urethane-based adhesive. The manufactured single lap joints were initially tested under tensile loading conditions using a screw-driven universal tensile machine to achieve strain rates of 0.0015 $s^{-1}$ and 0.15 $s^{-1}$. Furthermore, these joints were subjected to dynamic loading conditions at strain rates of 15 $s^{-1}$ and 150 $s^{-1}$ on a servo-hydraulic universal testing machine. Here, the bond strength and peak loads were determined. Furthermore, using the digital image correlation (DIC) system, the local and global strain distributions were investigated within the adhesive bond line. Finally, low magnification and optical microscopy analyses were conducted to identify the resulting failure modes. Initial results revealed a clear effect of strain rate on the peak load and shear lap strength. In addition, DIC analysis revealed evidence of strain concentrations at the lap ends as well as major strain distributions within the bondline. Furthermore, a combination of adhesive and cohesive failure modes was evident after low magnification analysis. Finally, it is clear that these results can be utilized for comparative analysis and design purposes of adhesive joints of similar and dissimilar materials that may be subjected to various strain rates.

# Chapter 1. Introduction

## 1.1 Composite Materials

Composite materials along with nanomaterials are considered as the most advanced materials currently in use for various industries, i.e., automotive, aerospace, marine and sports and many common applications. They provide ample scope into design changes, materials, and processes. The main advantage of composites materials is their high strength to weight ratio when compared to other metals, stiffness and cost-effectiveness make them an easy choice in various industrial applications [1]. Detailed advantages of composites are stated below. Depending upon the shape of reinforcement the composites are classified into fiber composite, flake composite, particulate composite, and laminate composite.

## 1.2 Advantages of composite

Strength to weight ratio:

The primary advantage of composite materials is their strength to weight ratio compared to most wood and metals. Their lightness is important in most automotive and aircraft as less body weight significantly decreases fuel consumption and aerodynamically increase the speed it can reach. Most of the automotive and aerospace applications are built more with composites than metals [2]. In addition, by combining resins and reinforcements at different placements and layers stacking provides engineering flexibility so engineers can tailor properties of the PMCs. Their structural integrity and strength are determined by four kinds: specific strength (strength to weight ratio), tensile strength, compressive strength and lastly shear strength. So, these composites can be manufactured to have very high strength compared to metals and wood. Though metals are equally strong in all the directions, composites can be tailored to have a good strength property in a specific direction as per the applications [3].

Corrosion Resistance:

Composite materials have good resistance to damage from weather and most of the harsh materials when compared to most of the metals, and hence their application in such environments has been increased recently. Aluminum alloys are considered to have very good corrosion resistance in metals. In industrial and marine applications, due to the presence of aggressive salts their resistance deteriorates and hence use of metal matrix composites has increased [4] [5].

High-Impact Strength:

Composites can be manufactured to resist high impact energies. As a result, some composites are used in bulletproof vests and panels and shields for a number of military vehicles. Many researchers are focused on the fundamental parameters determining the impact resistance of reinforced composites in various applications have been investigated [6] [7].

Design Flexibility:

Composites can be formed into complex shapes more effectively than most different materials. This gives designers the opportunity to make practically any shape or structure. Most marine applications, for instance, are worked from fiberglass composites because these materials can without much of a stretch be formed into complex shapes, which enhance structural integrity while bringing down expenses. Other Advantages include part consolidation, dimensional stability. nonconductive, nonmagnetic, radar transparent, low thermal conductivity, durable [8].

### 1.3 Types of composite materials

Composite materials are commonly classified at following distinct levels:

- The first level is matrix-based composites. The matrix binds the fiber reinforcement, gives the composite component its shape and determines its surface quality. Figure 1.1 shows the classification of composites based on matrices. A composite matrix may be a polymer, ceramic, metal, or carbon. The classes in matrix-based composites are Metal Matrix Composites, Metal Matrix Composites (MMCs) and Ceramic Matrix Composites (CMCs), Polymer Matrix Composites (PMCs), and carbon matrix composites.

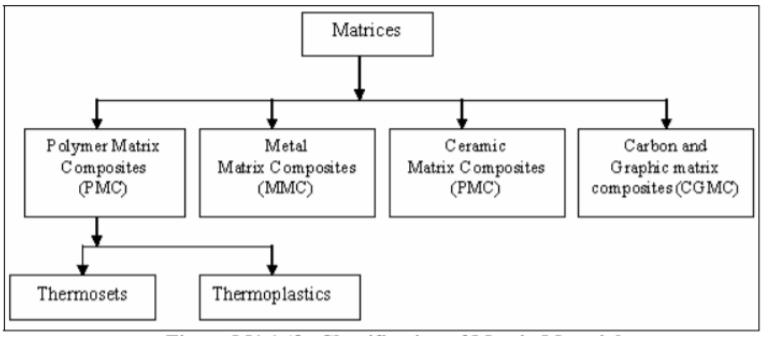


Figure 1.1 Classification of composites based on matrices.

- The second level is the reinforcements composites fiber reinforced composites, laminar composites, and particulate composites. Figure 1.2 shows classification of reinforcements [9]. The fiber reinforced composite can be further distinguished in the form of continuous and discontinuous fibers. Fiber reinforced composites are composed of fiber embedded in a matrix. These fibers can be continuous long fibers or discontinuous short fibers. Fibers are small in diameter, and when pushed axially, they bend easily although they have excellent tensile properties. These fibers must be supported to keep individual fibers from bending and buckling. There are many commercials available such as fibers glass and carbon as well as Kevlar 49. Other fibers, such as boron, silicon carbide, and aluminum oxide, are used in limited quantities [10]. Some of the composites are introduced in more detail.

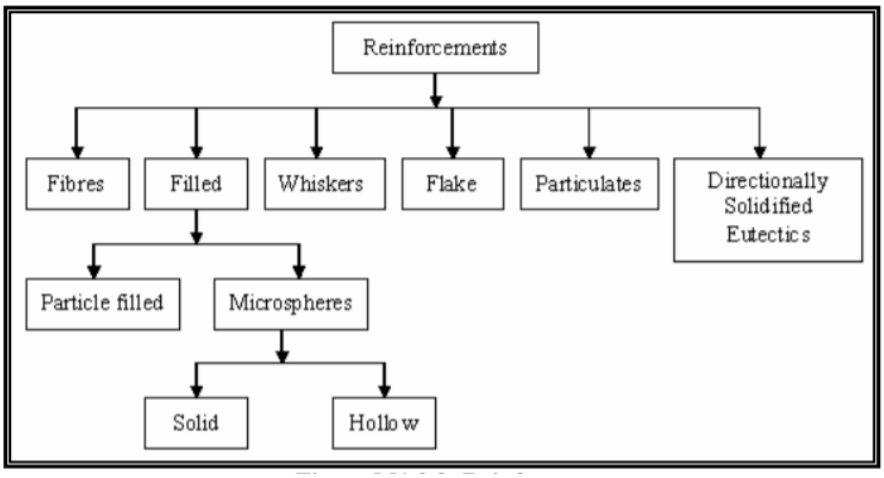


Figure 1.2 Classification of reinforcements.

### 1.3.1 Matrix Based Composites

#### 1.3.1.1 Metal matrix composites

Metal matrix composites consists of less than two constituent parts, one being a metal fundamentally, the other material might be an alternate metal or another material, for example, ceramics or carbon fiber. The processing methods utilized to manufacture MMCs can be grouped depending on the matrix during processing and are classified into three categories: (a) liquid phase processes, (b) solid-state processes, and (c) two-phase (solid-liquid) processes [11]. Aluminum matrix composites (PMCs) are potential materials for different applications because of their high structural integrity and good mechanical properties. The reinforcements into the metallic matrix improve the stiffness, specific strength, wear, creep and fatigue properties compared to other metals [12]. Other common metal matrix composites are magnesium matrix, titanium matrix, copper matrix, and super alloy matrix.

#### 1.3.1.2 Polymer Matrix Composites

Polymer Matrix Composite (PMC) consists of a polymeric matrix combined with a fibrous reinforcing dispersed phase. In the polymer matrix composite materials, there are two types of materials which are thermosetting resin-based composite materials and thermoplastic resin-based composite materials [13].

#### 1.3.1.3 Thermoplastic polymer

Thermoplastic polymers are usually a polymer that is moldable above its glass transition temperature and returns to its solid state upon cooling [14]. Thermoplastics have a high molecular weight with polymer chains which bind together with intermolecular forces and hence permits to be remolded into a variety of shapes depending on the mold. The examples of thermoplastic polymers are polycarbonate, acrylic, nylon, polyethylene, polypropylene, polystyrene, teflon, and polyvinyl chloride [15].

### 1.3.1.4 Thermosetting polymer

Thermosetting polymers are synthetic materials which strengthen during heating and curing process and cannot be remolded or reheated after initial setting. Thermosetting polymers are quoted to make permanent bonds and large solid shapes. Though these polymers have high strength attributes, they cannot withstand high temperatures. The examples of thermosetting polymers are mostly resin of polyester, polyurethanes, vulcanized rubber, bakelite, duroplast, epoxy resin.

Adhesives based on thermoset chemistry play a major role in many bonding applications. The most common thermoset adhesives are epoxy, acrylic, and polyurethane. When exposed to the cure temperature of the particular thermoset, a permanent bond is formed between the two substrates as they will undergo a chemical curing reaction. These thermoset bonds exhibit high load bearing capacities and high creep resistance under constant and varying loading conditions. Today the toughened variants of these thermoset adhesives are replacing the using of traditional joining methods such as welding, riveting and bolting.

**Epoxy-based thermosets**

Epoxy-based thermosets adhesives are mainly characterized by high strength, its excellent resistance to chemicals and higher temperatures and excellent adhesion to many metallic and non-metallic substrates. Epoxy-based thermosets are classified based on oxirane content. The oxirane content educts cure at high temperatures which offer high strength and excellent adhesion to a wide range of different substrates [16]. Figure 1.3 shows the chemical formula of epoxide [17].

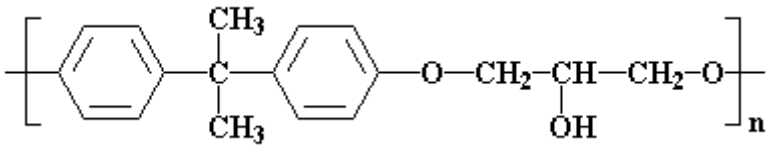


Figure 1.3 Chemical Formula of epoxide.

Hengshi proposed a new method to prepare a rubber toughened epoxy with high modulus and high impact strength and he concluded that irrespective of the curing agent, the composites prepared by

the new method always exhibit much higher impact strength, yield strength, and Young's modulus than the corresponding traditional composites [18].

**Polyurethane adhesive**

Urethane adhesives are produced by reacting isocyanates R—N=C=O with alcohols H—O—R. Alternatively, isocyanates can react with water or moisture and an unstable carbamide acid is formed which again decomposes to form an amine and carbon di oxide, and this $CO_2$ released will foam into polyurethane system. Polyurethane adhesives show excellent adhesion to many materials such as glass, wood, plastics, metals, and composites. The chemical bonding occurs when a covalent bond is formed between polyurethane and the substrate due to the reaction between the isocyanates and active hydrogen [16]. Figure 1.4 shows the chemical formula of polyurethane [19]. Figure 1.5 shows an overview of different areas of application.

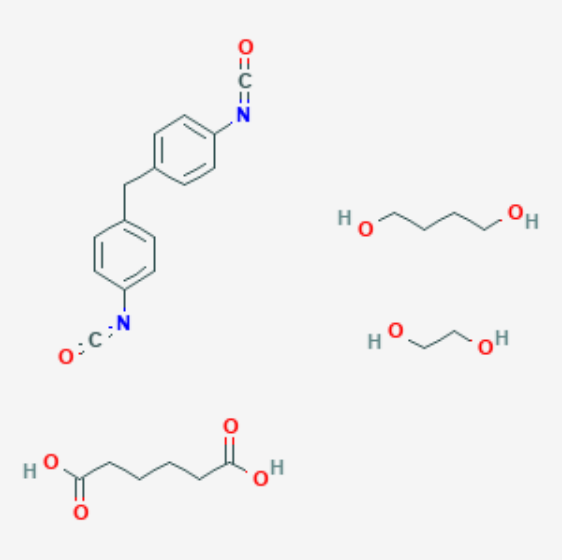

Figure 1.4 Chemical formula of polyurethane.

Table 1.1 Overview of different areas of application

| Application | Function | Material basis |
|---|---|---|
| Structural bonding | Joining of different substrates<br>• semistructural<br>• structural<br>• crash-resistant | Modified silane (MS)-polymer<br>Elastomer<br>(Meth)acrylic<br>Epoxy<br>Polyurethane |
| Structural foams | Local reinforcements | Epoxy<br>Polyurethane |
| Sealing | Protection against corrosion, water and dust, isolation of noise propagation | PVC<br>Elastomer<br>EVA |
| Panel damping | Reduction of noise, vibrations and harshness (NVH) | PVC<br>Epoxy<br>Elastomer |

### 1.3.2 Fiber reinforced polymers

Fiber reinforced polymers consists of fibers of high strength and modulus embedded in or bonded to a matrix with distinct interfaces. Unique characteristics of fiber reinforced composites are their internal damping which leads to better vibrational energy. These high damping capacities are very useful in automotive applications in which noise, vibration, and harshness are critical for passenger safety. The most common fibers used in the manufacturing of fiber reinforced composites are glass fibers, carbon fibers, Kevlar fibers, and boron fibers.

**Glass fibers:** The common advantages of glass fibers are low cost, high tensile strength, high chemical resistance, and excellent insulating properties. The disadvantages include low tensile modulus and high density compared to other commercially available fibers. Two types of glass fibers used in industry are E-Glass fiber, S-Glass fibers, and C-Glass fibers. Commercially, these fibers are available in strand or roving form. Glass fibers are also available in the woven roving form, and the bidirectional properties change with the style of weaving along the length (warp), and crosswise are (fill) [10]. Figure 1.5 shows the tensile strength of commercially available fibers [10].

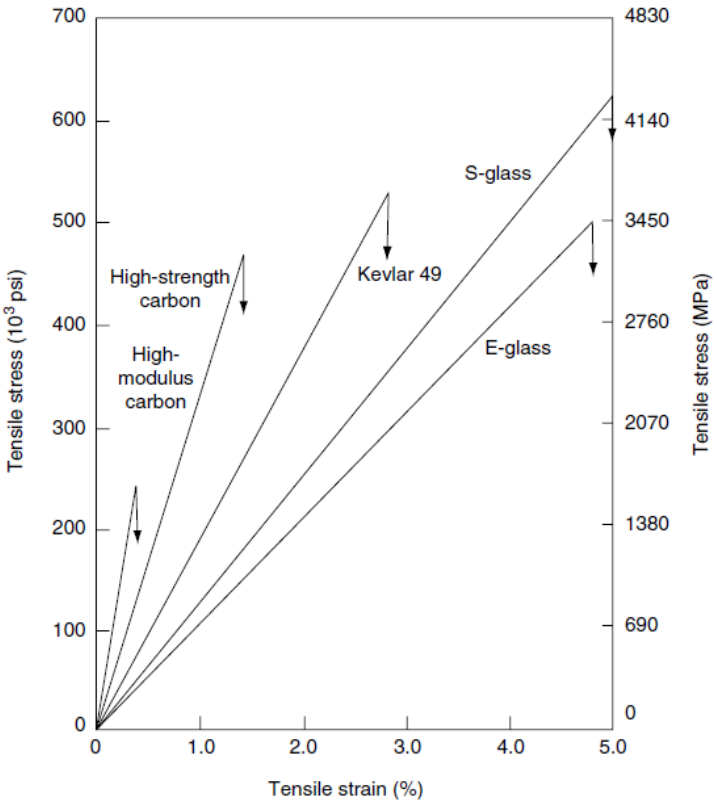


Figure 1.5 Tensile strength of commercially available fibers.

**Carbon Fibers** are commonly used reinforcements with excellent mechanical performance to weight ratio are preferred in most of the applications. A good interfacial adhesion between carbon fibers and polymer molecules is required for better surface energy property. The carbon fibers play a crucial role in a variety of specialized applications such as aerospace, automobiles, chemical industry, missiles, and other industries. The main advantages of carbon fibers, owing to their inherent properties, are high strength and stiffness, dimensional stability, low coefficient of thermal expansion, and fatigue resistance. Commercially available carbon fibers are classified based on general-purpose (GP), high-performance (HP) and activated carbon fibers (ACF). They have been used commercially in the form of woven, roving, prepregs and chopped fibers. Most of the manufacturing procedures include filament winding, pultrusion, compression molding, vacuum bagging, and injection molding. Figure 1.6 shows the manufacturing process for PAN-based carbon fibers [20].

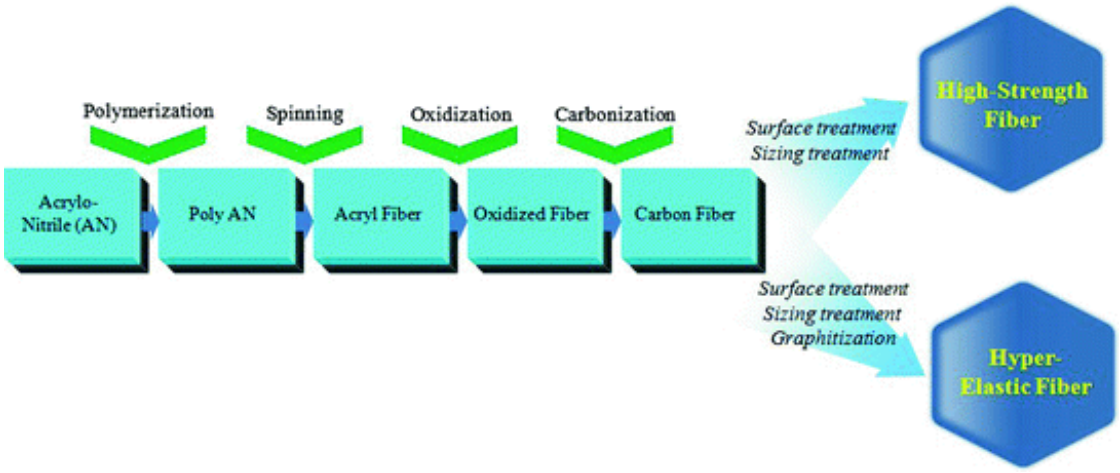


Figure 1.6 Manufacturing process for PAN-based carbon fibers.

**Kevlar Fibers** are usually known as aramid fibers which are a class of heat resistant and strong synthetic fibers. Kevlar fiber is commercially available in a variety of types, and the most common ones are Kevlar® 29 (K29) and Kevlar® 49 (K49). Most of the Kevlar fibers are used in ballistics applications and protective apparel such as cut resistant gloves, helmets, armoring.

**Boron fibers** were used for specific aeronautic composites, for example in the wings of the F14 by Grumman, for their structural properties [21]. Boron fibers have high performances such as thermal resistance, High Modulus, High compression strength.

### 1.4 Aluminum Alloys

Aluminum, the second largest possible element on the earth and is highly demanded in engineering applications. It could be divided into two major categories: casting composition and wrought composition. Wrought alloys are pure aluminum which are strain hardenable, high formability, corrosion resistance but the strength cannot be a prime consideration. Common applications of wrought aluminum are food packaging trays of pure aluminum, decorated foil pouches for food and drink. Aluminum is basically classified into different categories as per the composition which are Al-Cu alloys, Al-Mn alloys, Al-Si alloys, Al-Mg alloy, Al-Si-Mg alloy, Al-Zn alloy [22].

Al- Cu alloys are represented as Al 2014, 2024, 2195, etc. Most of these alloys are heat treatable, and high strength at room and elevated temperatures and a good combination of toughness and weldability can be seen in these alloys. The higher strength of this aluminum is used in aircrafts internal structure such as extrusions and plate. The fuel tanks and booster rockets of

the space shuttle are also made of aluminum 2000 series.

Al-Mn alloys are represented as Al 3000 series which have their primary application in roofing and packaging. These alloys are mainly used in cooking utensils and chemical equipment as they can be readily brazed, welded, and soldered and have excellent corrosion resistant properties.

Al-Si alloys are represented as Al 4000 series, which have medium strength but good flow characteristics. Since it can be heat treated, it is principally used for casting aircrafts pistons. Specific applications include refrigerant coolant system in a brazed unit of Si alloy sheet [22].

Al-Mg alloys are represented with 5000 series, and they have very high toughness at cryogenic temperature. They can be easily weldable even for higher thickness values — these specialty alloys. Specialty alloys can be used as the beverage can end alloy, for automotive body panel and frame applications and bright trim applications.

Al-Mg-Si alloys are represented as 6000 series, and they are heat treatable and have moderately high strength coupled with excellent corrosion resistance. The unique feature of 6000 series is their extrudability making them open to broad applications, particularly where strength- or stiffness is essential. Roof structures for arenas and gymnasiums are mainly made of Al 6063 and Al 6061. The extruded alloys make the entire frame of motorcycles and cars. In specific, the BMW Model 5 front and rear axles are made up of aluminum 6061.

Al-Zn have very high strength and are the most robust versions of wrought aluminum and are represented as 7000 series. The most comprehensive applications of 7xxx alloys are in aircraft industries, and lightweight alloys in this series are used to build bumper structures, which increase the fuel economy [22].

## 1.5 Joining Methods of single lap joints

There are two types of joining methods for structural and assembly joining in aerospace and automotive industry. They are mechanical fastening and adhesive bonding:

### 1.5.1 Mechanical Fastening

Many commercial aircraft contain millions of fasteners (e.g., bolts, rivets) for composite aircraft. Fasteners are less expensive in comparison to adhesive bonding, but the stress concentration in mechanical fasteners in the bolt-region and weight added to the structure is significant. Figure 1.7 shows the bolted joints in a marine application. Hence, efficiency of bolted joints design for composite aircraft, in terms of maximizing joint strength while simultaneously minimizing fastener requirements, presents a significant technical challenge to aircraft manufacturers. Mechanical fasteners are simple and efficient ways of bonding joints in various industries. Figure 1.8 shows various mechanical fastening systems used in the industries. The fasteners are straightforward to assemble, have low component costs, and are easy to inspect; all of which are important for construction, repair, and maintenance. A typical bolted assembly in a marine structure can be seen in Figure 1.9 is showing the bolted attachment of a stiffener web to a secondary structure, and the bolted attachment of the secondary structure to the main component.

Figure 1.7 Bolted joints in a marine application

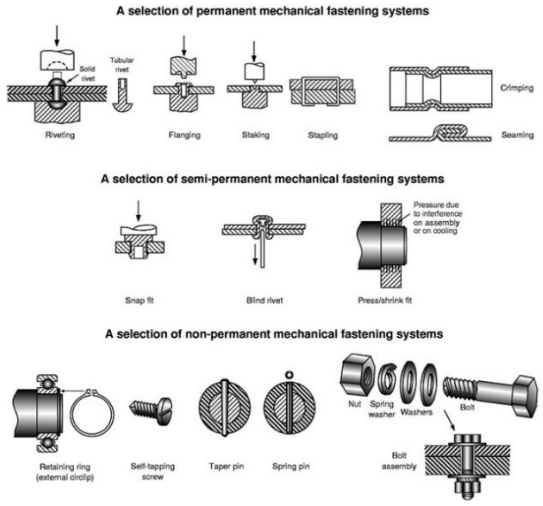


Figure 1.8 Various mechanical fastening systems [23]

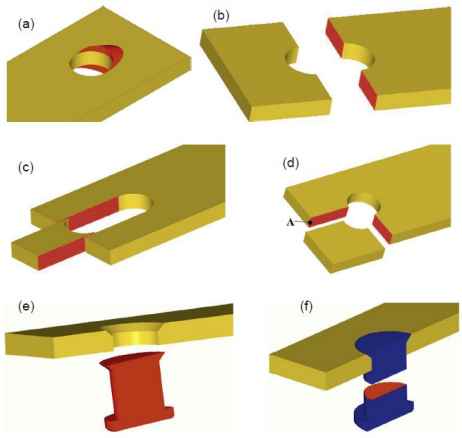


Figure 1.9 Failure modes in composite bolted joints: (a) bearing failure, (b) net-tension failure (c) shear-out failure, (d) cleavage failure, (e) fastener pull-through, (f) bolt failure [24].

Many papers have presented about the local and global finite element approaches to assist the design and failure analysis of composite bolted joints. McCarthy discussed the effect of bolt-hole clearance on ultimate peak load and three-dimensional stresses, and he found that bolt-hole clearance did not have a significant effect on the ultimate failure load of joints, but it induces significant three-dimensional stresses into the composite laminates [24]. The location and failure mode is essential in the analysis and design of mechanically fastened joints because these can be

factored in the empirical analysis. The typical analysis of mechanically fastened bolted joints is the empirical correlation factor which is a ply-level criterion. The difference in materials properties of composite and metal determines the joint strength, failure mode, and failure mechanism. Since composites are brittle and lack ductility of metals to minimize the stress concentration around the holes. Delamination is present in the composite joints which are the primary cause of failure in these type of joints [25]. Although mechanical fasteners provide a reliable joining method, there are many disadvantages of mechanical fastening which are:

1. Considerable stress concentration
2. Prone to fatigue cracking in metallic component
3. Hole formation can damage composite
4. Poor load bearing capacity in composites
5. High corrosion of metal
6. May require extensive shimming

The concentration around the hole produces 3D stresses which produce non-uniform distribution in the joined components promoting the crack initiation [26].

### 1.5.2 Adhesively bonded Joints

Adhesively bonded composite single and double lap joints are widely used in the aerospace industry for structural joining and assembly joining [27]. These joints should be able to resist impact loads, providing high impact strength, and high deformation before failure. The joints must, therefore, be able to absorb substantial amounts of energy during impact, but at the same time be capable of maintaining the integrity of the structures. Adhesive joints are an increasing alternative to mechanical joints in most of the engineering applications as they provide uniform stress distribution along the bonded area which enables to have higher stiffness and load transmission. The strength of the adhesives, varying from 5MPa up to 50 MPa. The research says, larger the bonding area better the strength of the lap joint [28].

In the aerospace industry, any new adhesives or change in primary adhesive base metal of the bonded structure is assessed by a compression and fatigue test of the bonded structure before use on aircraft. It says that the tensile strength across adhesive joints is useful to understand if the structure buckling point is reached. Figure 1.10 shows the usage of adhesive bonding at the Airbus A380. The use of adhesive joints reduced the weight of the fuselage frame by 15 % in airbus 380 which would further affect the size and weight on the engines. The use of adhesive boning for joining CFRP aeronautical structures is driven by need of strong and lightweight structures.

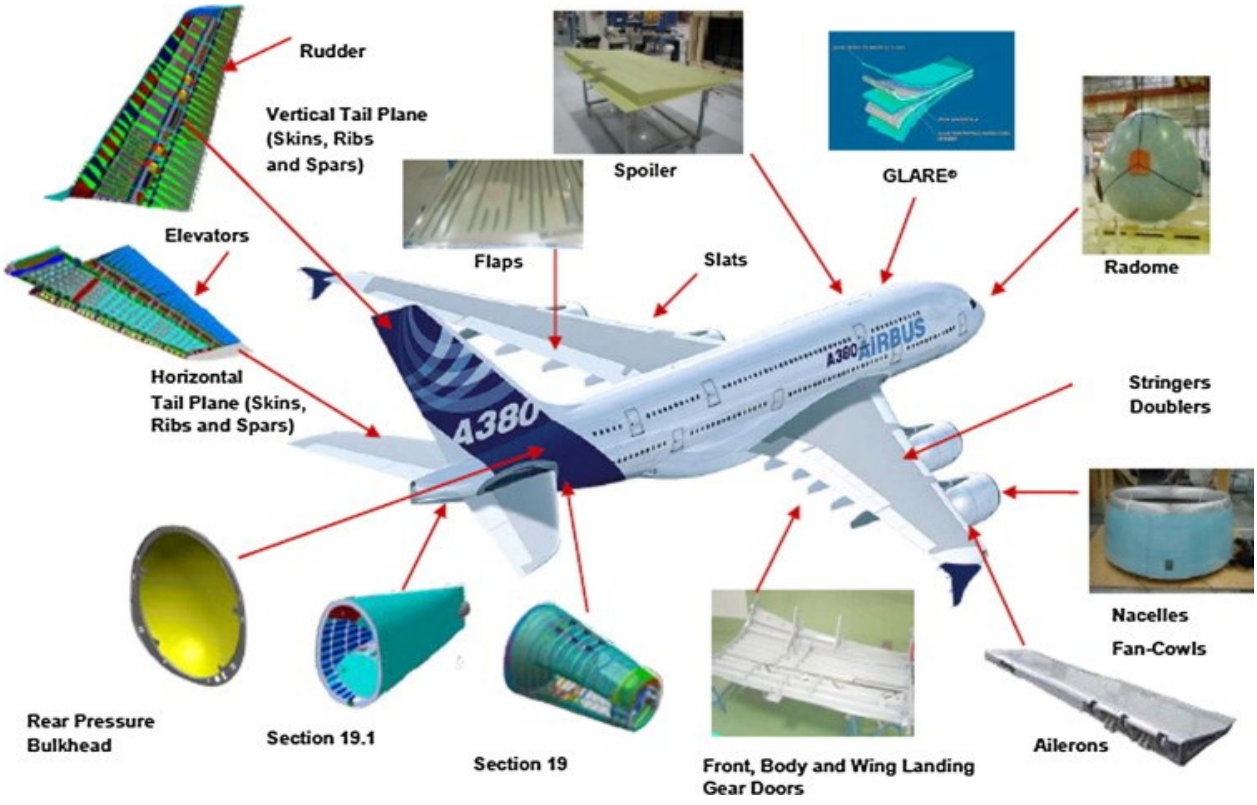


Figure 1.10 Usage of adhesive bonding at the Airbus A380 (photo supplied by Airbus).

In the automotive industry, adhesives must meet a number of requirements, which are less dependent on joint performance. Figure 1.11 shows the body parts were adhesives are used in automotive industry [29]. One of the most common applications of adhesive bonding in automotive is hoods and roofs. Automotive hoods are bonded with adhesives to avoid unsightly weld parts. Structural adhesives like vinyl plastisol, urethanes, epoxies, phenolic, and polyester are

commonly used in automotive and the applications are shown in table 1.2 [30]. The use of adhesives for bonding brakes linings was introduced in 1949. This technique is also used for disk brakes, clutch pads, clutch facings and transmission pads.

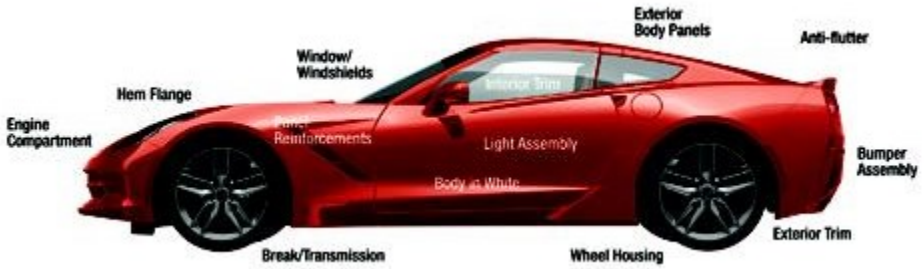


Figure 1.11 Body parts where adhesives are used in the automotive industry.

Table 1.2 Common structural adhesives used in automotive.

| *Use* | *Resin* | *Comments* |
|---|---|---|
| Body and roof reinforcement panels | vinyl plastisol | bonds through oil |
| Double shell roof | vinyl plastisol | bonds through oil; prevents flutter |
| Hood inner and outer panels | vinyl plastisol | bonds through oil; prevents flutter |
| Brake shoes | nitrile-phenolic | resists heat and impact |
| Clutch and transmission bands | nitrile-phenolic | resists heat and impact |
| Window sealants | polysulfides, urethanes | best available method |
| Plastic bumpers | urethanes | improves performance |
| Disc brake pads | phenolic | heat resistant |
| FRP body panels (sports car and truck) | urethane, polyester | used over twenty-five years |
| Radiator tanks | epoxy | replaces solder |
| Plastic load floors | polyolefin | electromagnetic cure |
| Hood hem flanges | vinyl plastisol | reduces flutter |

In marine applications, the adhesives and sealants are used in many applications: to bond hull/deck, [31] the channels running through the teak-made deck staves, the sea chests, the exhaust systems, the air intakes, the portholes, and the windshields, inside the boat the panels of cabins, the toilets and the engine compartment are glued and sealed [32]. Figure 1.12 shows the adhesives and sealant application in marine industry.

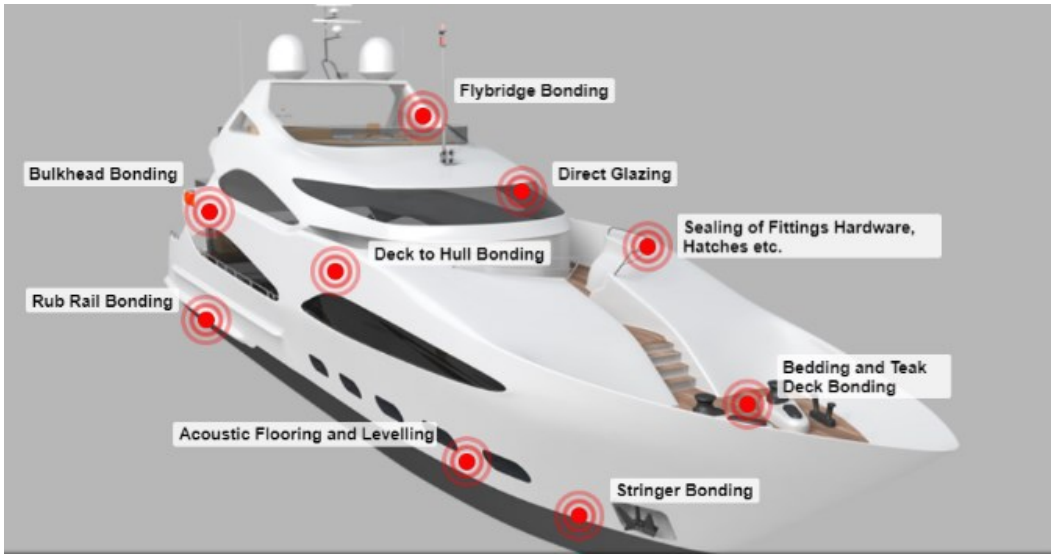


Figure 1.12 Adhesives and sealants application in the marine industry.

## 1.6 Literature survey

In research studies, the joint strength has been determined by the static strength capacity of the adhesive joint. Here, the static strength has been defined as the ability of the joint to withstand an applied load without failure or plastic deformation [33]. Adhesive joints have shown to be a great alternative to mechanical fastening to bond the substrates together. The adhesive forms coherent layer between both the substrates which transfer the load from one adherend to another [34]. The strength of the bond is mainly governed by compatibility of the adhesive and adherend which can be controlled by the surface treatments on the adherends and the joint configuration [35]. To produce a proper adhesive joint that meets desired strength as well as the dimensional repeatability, material, and structural factors have to be considered. Hence, a literature review was performed regarding the surface treatments, preparation of joints and stress analysis.

### 1.6.1 Surface Treatment

Surface treatments are normally used to remove any formation of boundary surface from machine oils, weak oxides, and hydro oxides. In order to maximize the little contact between the substrate and adherend during the curing process as this gives high surface area energy. In addition, they generate a specific structure on the adherend surface for better contact area. Applying a coating to

passivate the adherend surface from corrosion which can be achieved by using conversion coated or anodizing. Manual roughening of the bonding surface and cleaning with a degreaser for the surface treatment [36]. Gentey and Aufry stated that using a sol primer and degreasing/HNO3 increases the failure load [37]. A suitable surface preparation (i.e., a good surface treatment combined with a proper primer application) not only increases the load at the break but it also increases the reliability of the results [38] [39] [40]. Sensitivity to rust is a crucial factor to consider while preparing a surface of the specimen. Yoa and Zu polished the steel plates on both sides to remove any rust within the bond area and then applied acetone to the steel plate to further clean the surfaces [38]. From graph 1.13, it is evident that using a sol-gel as primer increase the surface adhesion reaches its highest value. In the case of surface treatments without primer, degreasing + $HNO_3$ and abrasion almost showed similar maximum load values [37]. Figure 1.13 shows the effect of pretreatments methods on the polymer composites [41]. Table 1.3 shows the effects of various surface pretreatments methods on the surface tension, surface roughness, surface chemistry, bond strength and durability of the polymer composites.

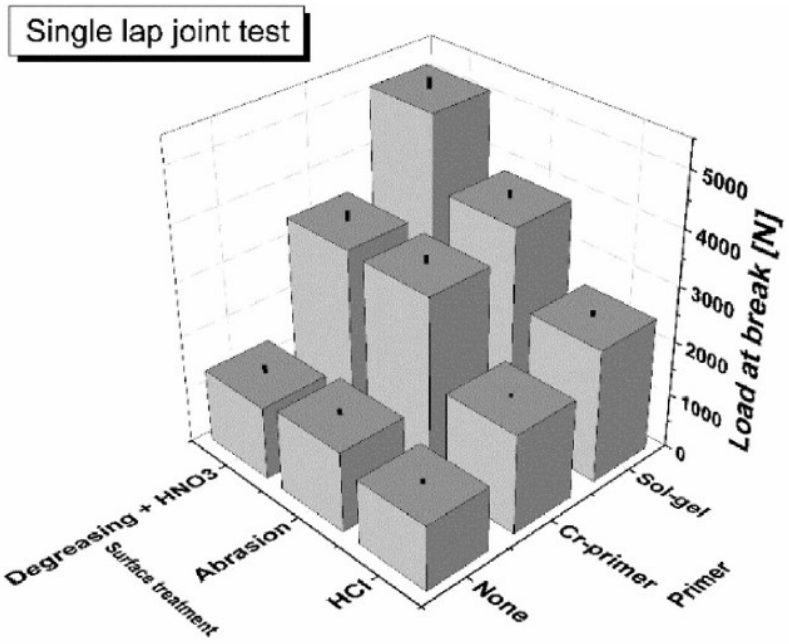


Figure 1.13 Average loads at break measured by the SLJ tests.

Table 1.3 Effects of various surface pretreatments methods on the surface tension, surface roughness, surface chemistry, bond strength and durability of the polymer composites.

| Treatment type | Material | Nature of treatment | Surface tension | Surface roughness | Surface chemistry | Bond strength | Durability |
|---|---|---|---|---|---|---|---|
| (1) Abrasion and solvent wipe | Thermoset and thermoplastic | Remove mold release | | Y | | Increased found for thermosets | Good for thermosets |
| (2) Grit blasting | Thermoset and thermoplastic | Remove mold release | | Y | | Increased found for thermosets | Good for thermosets |
| (3) Acid etch | Thermoset and thermoplastic | Etch[a] | Y | | Y | Slight increase | Poor |
| (4) Peel-ply | Thermoset | Remove mold release | | Y | | Increase | Good |
| (5) Tear-ply | Thermoset | Remove mold release | | | | Increase | Good |
| (6) Corona discharge | Thermoplastic | Oxidising | Y | | Y | Double | Good (90 days) |
| (7) Plasma treatment | Thermoplastic | Ablation and/or oxidation[a] | Y | Y | Y | Increase | Good (90 days) |
| (8) Flame treatment | Thermoplastic | Oxidasing[a] | Y | | | Increase | |
| (9) Laser treatment | Thermoset and thermoplastic | Ablation and or oxidation | | Y | Y | Increase | More research is necessary |

[a]Depends on polymer matrix material.

### 1.6.2 Selection of Adhesive

Adhesives can be categorized using a wide range of parameters. Among the most common are the source, function, chemical composition, reaction method, and physical form. When considering the functionality of adhesives, these materials can also be classified as structural and non-structural. The difference between structural adhesives and non-structural adhesives is that structural adhesives are high strength materials which can support high loads. Epoxies, phenolic, and polyurethanes are examples of structural adhesives, and synthetic rubbers and polyesters are examples of non-structural adhesives.

The most commonly used adhesive for structural application and SLJ, DLJ and scarf lap joints are epoxy and polyurethane [42]. However, for hybrids joints, there are other types of adhesives used. Epoxy is one of the common types of adhesives for dissimilar metals as they exhibit low creep, high toughness, corrosion and chemical resistance, good gap filling capabilities, excellent heat resistance, low cost, and joint design. An assessment of single lap joints with polyurethane adhesive proved to be 100% efficient for CFRP Joints and becoming less for dissimilar adherends, particularly for the case of different adherend thickness. This is due to flexural rigidities of the adherends which give an uneven stress distribution in the bondline [43]. Esmaeil and Onur studied

the load carrying capacity of single-lap joints bonded with different adhesives based on epoxy resin, and the experiments were carried out at two strain rates which are 1 mm/min and 100 mm/min and he presented the cohesive failure in adhesive increased with an increase in strain rate, and the peak loads are lower for the two-part adhesive compared to film-based epoxy adhesive [44].

Halliday used Scotch-Weld AF-1632U Adhesive for bonding. It is a modified structural epoxy film adhesive which is cured at 125 ˚C [41]. Ribeiro used Nagase Chemtex – XNR6823 and XNR6852 to test his adhesive lap between aluminum and carbon–epoxy composites [36] whereas Yoa used Epoxy resin structural adhesive Sikadur 330 [38]. Challita used an epoxy adhesive film SA 80 by GURIT to test steel substrates under dynamic shear loading from quasi-static (10^-4) up to high (10^4) strain rates [45]. Six adhesives of several families were considered in the experimental program: two epoxy adhesives, one acrylic adhesives, one methacrylate adhesive, and two polyurethane adhesives and behavior is shown in figure 1.14 [46].

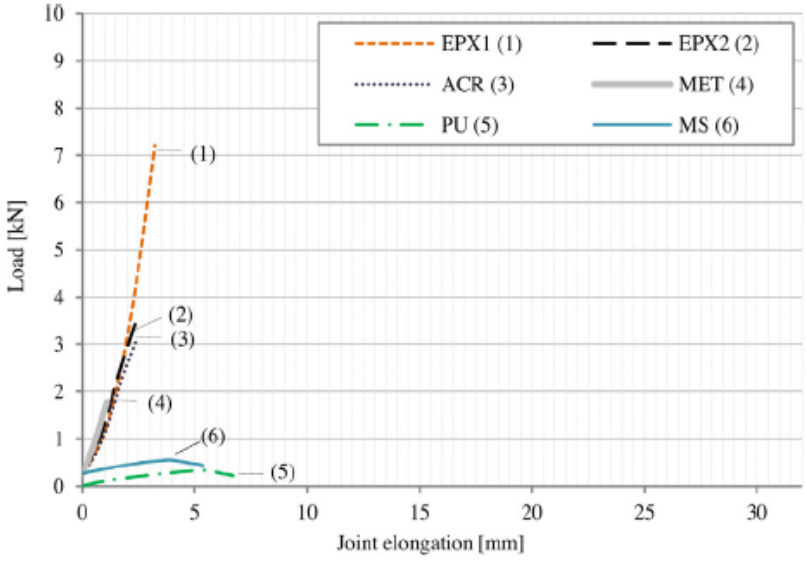


Figure 1.14 Load and Joint Elongation for the six adhesives chosen.

### 1.6.3 Preparation of Joint

Joints should be designed in such a way to minimize stress concentration. The research work mostly focuses on uniform shear stress distribution in the adhesive to attain higher failure loads at the break. Joints made with high strength adhesives are more likely to fail prematurely in the composite before failure in the adhesive occurs [47]. The effect of adhesive dimensions on the strength of adhesively bonded aluminum joints was studied experimentally, and the results for the aluminum joints of the thickness of 1 mm and an overlap length of 15 mm showed highest interfacial shear strength when compared with two other adhesive thickness of 0.5 mm and 1.5mm [48]. When the joint is very large, then the adhesive selected should have a cure time that is sufficiently long to allow for the application time [27]. Curing time for the adhesives is different for different applications. Rapid cure time was found to decrease the failure load by 50%, and hence the effect of curing time has a significant effect on bond strength than the presence of impurities in the bond [49]. Halliday studied about the shear strength and fracture toughness for different curing times and temperatures ranging from 20 days to 423 days and found out that when the joint is aged in water at 70°C for 423 days the shear strength was reduced by 25 % and the fracture toughness was reduced by 15% [41]. The adhesive thickness also plays a major role in determining the strength of the joint. Researchers have studied the effect of adhesive thickness on the strength of SLJs [50] [42]. An increasing fracture toughness with increasing adhesive thickness was found for Single Lap Joints. The lap-shear strength decreases as the adhesive layer gets thicker for flexible adhesives. Joint geometry can be selected from ASTM though ASTM does not standardize tests for dissimilar metals as stated by Anyfantis [47]. The use of bonding fixture is recommended to ensure correct bond length and accurate alignment and uniform bond line thickness. Broughton even introduced end tabs to single lap joints to reduce the eccentricity of the load path and to discard the out of plane distortions and ensure that the test is taking place in a single 2D Plane. These end tabs help in reducing peel stresses and uniform shear stress in maintained throughout the bond line area [51]. The effects of adherend yield strength, adherend thickness, adhesive thickness, overlap, adhesive toughness, surface treatment, durability and test speed on the lap shear strength were investigated using the Taguchi method. These results were used to give a failure prediction equation. His results presented that the effect of surface treatment and strain rate are negligible when compared to the adhesive and adherend thickness [52]. Figure

1.15 shows the different tapers used for single lap joints and he stated that the taper for adhesive shows the maximum lap shear strength when tested under tensile loading conditions [53].

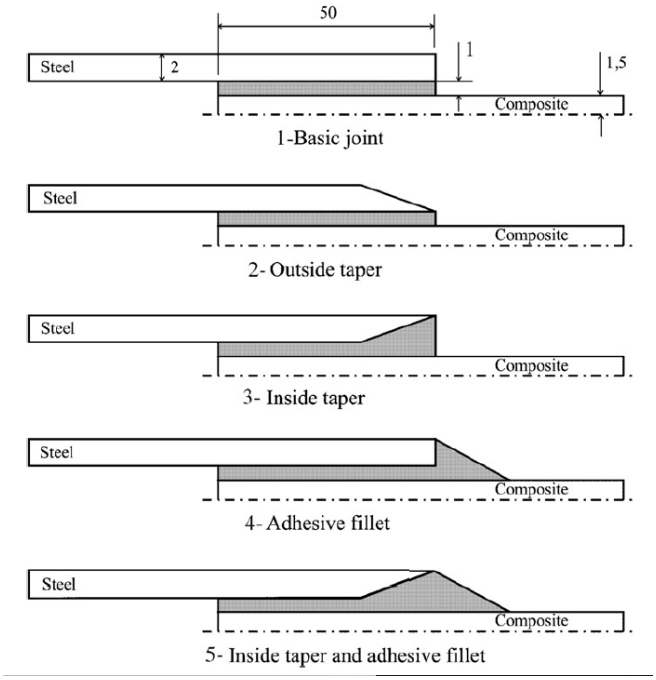


Figure 1.15 Different Tapers for Single Lap Joints.

The bonding procedure was explained in detail by Challita [45]. He mainly presented that the substrates need to be sanded with appropriate sanding paper and then wiped of any dry paper and cleaned with ethanol for three times by changing the paper every time. Furthermore, he checked for the thickness of the substrate at five places using a micrometer to understand the surface roughness after treatment of adherend. Then, after cleaning the surface with ethanol for three times, he applied the adhesive to the bond and end tab area and placed it in a curing oven and maintained the temperature required for the adhesive. After the end of the cure cycle, the specimen was removed from the mounting, the total thickness of the specimen is measured with the micrometer at the same five points marked initially on the substrates, and an average value is calculated. The adhesive joint thickness is the half difference between the total average thickness of the bonded assembly and the sum of the average thicknesses of the substrates.

### 1.6.4 Stresses and Failure Modes in adhesively bonded lap joints

There are several types of stresses occurring in an adhesive bond as shown in figure 1.16 which cause failure in the joint which are:

1 Peel Stress: Stress developed when the material resists breaking under a peeling force at a predetermined angle. An adhesive can be chosen with respect to their peel strength by measuring using the ASTM D1876 test [54].

2 Cleavage Stress: Cleavage strength measures the ability of the adhesive to resist breaking when it is being pulled from one point. The cleavage strength of epoxy is measured using the ASTM D1062 test method [54] [55].

3 Normal stresses: Stresses which occur on a perpendicular plane where they act and can be compressive tensile.

4 Shear stresses: Stresses parallel to the plane where they act [55].

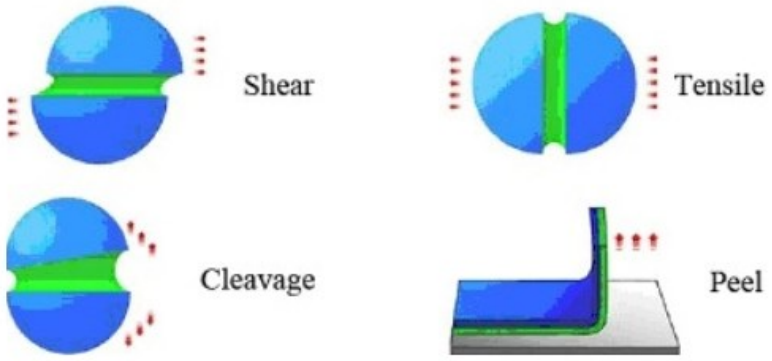


Figure 1.16 Stresses induced in a joint.

Failures occurring in an adhesive area can be cohesive or adhesive failure. Adhesive failure occurs due to the intermolecular forces acting between adherend and adhesive while the cohesive failure is due to the intermolecular forces inside the adhesive or adherend. To achieve a good interfacial strength, surface preparation on substrates, joint configuration, and adhesive properties need to be considered [27]. Figure 1.17 shows failure modes in composite single lap joints which are determined by the quality of specimen after break at each interface, specimen geometry, and loading [56]. In FRP composite adhesive joints, according to the standard ASTM D5573 [57]. It stated that there are six different failure modes and mixed mode failure wherever applicable.

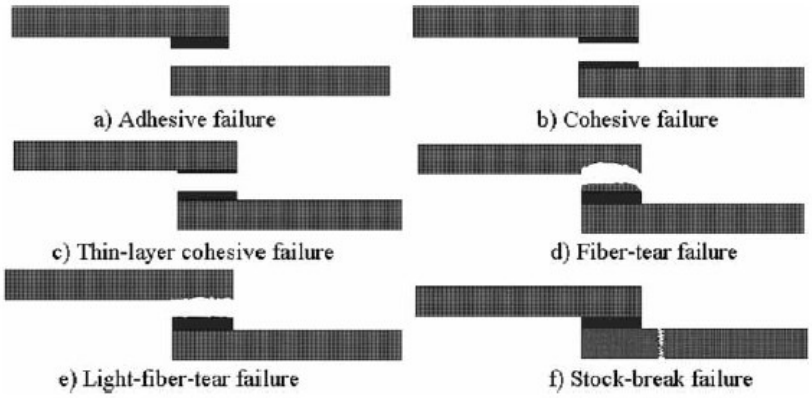


Figure 1.17 Failure modes in composite single lap joints.

Kim's study focused on the detailed investigation of differences in the failure modes occurring with a change in substrate and bonding length, and his results showed that the composite to composite joints fails due to delamination rather than the adhesive failure while the composite – aluminum joints fall in between aluminum-aluminum joints and composite – composite joints. He concluded that the maximum strength of adhesive could be used when the joint is designed to have strong resistance to delamination [58]. The use of internal adherend taper and adhesive fillet improves the shear strength of the bond. Figure 1.18 shows the comparison of failure loads for different double lap joints [53].

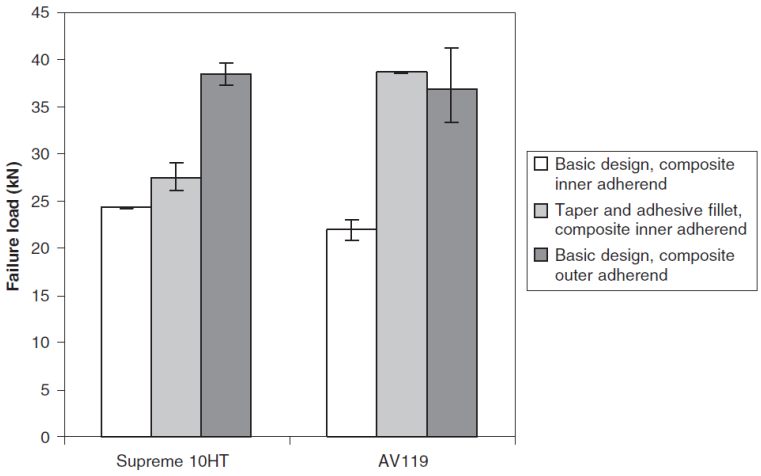


Figure 1.18 Comparison of failure loads for different double lap joints.

### 1.6.5 Strength determination for adhesive bonds

Mechanical properties of adhesive bonds can be determined by numerical or experimental methods. To perform an experimental study, the following test methods can be used: ASTM D1002: Standard test method for apparent shear strength of single lap-joint adhesively bonded metal specimens by tension loading (metal-to-metal) [59] and ASTM D5868: Standard test method for lap shear adhesion for fiber reinforced plastic (FRP) bonding [60]. In the numerical method, FEM is one of the most effective methods. This method has been recently combined with fracture mechanics to create cohesive damage models, which are able to accurately model the failure of an adhesive joint [61]. Many damage models have been developed to predict the behavior of adhesive joints. One of such methods is the Cohesive Zone Model (CZM) [61] [36]. Ribirea calculated interfacial shear stress at different phases using CZM Model, and the stress analysis showed that normal stress through thickness and sear stress peak at the overlap edges and these are highest at the interfaces [36].

Recent investigations on the effect of adhesive geometry, overlap length, adhesive thickness and concluded that as the overlap length increased, the ultimate failure load increased as well, as did the equivalent stiffness of the joint. Moya-Sanz studied different geometrical configurations of single-lap joints, such as adherend recessing and chamfering of the adherends and the effect on the mechanical strength of the joint in terms of failure load, eccentricity of the load, and the peak peel stress and concluded that the depth recess was found to be responsible for reducing peak peel stress because of the decrease in the cross-section at the end of the overlap [28]. Strain gage sensors have been used to study damage initiation occurring in the adhesive bond line [42]. It was concluded by Anyfantis that for single lap joints, the effect of the adhesive thickness and stiffness ratio is negligible compared to the effect of the overlap length to the stiffness and strength of the joints [48]. Ying Yan investigated the tensile performance of adhesively bonded single CFRP lap joints and predicted the failure modes and damage initiation to be adherend delamination failure, sometimes accompanied by some fiber pull-out. Figure 1.19 shows the failure load and lap shear strength with varying lap length and adherend thickness [62].

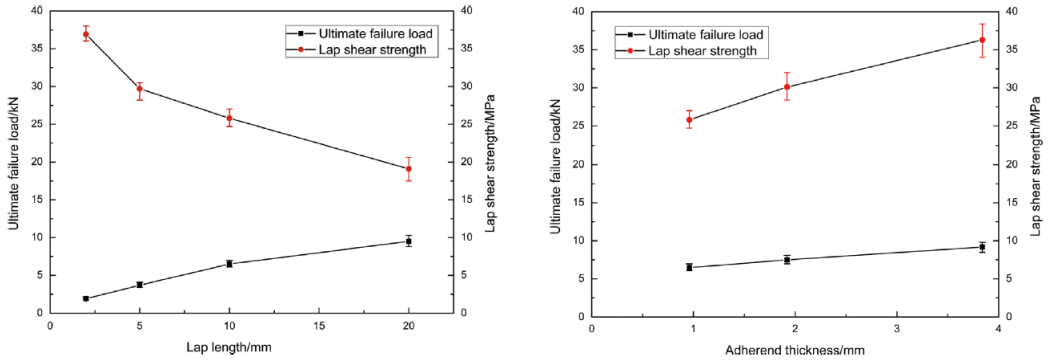


Figure 1.19 Typical failure loads and lap shear strength of single lap specimens at different overlap lengths.

Genty investigated the mechanical adherence measurement with three test methods i.e., SLJ, the Pull-off and the Three-Point bending tests [37]. The fracture surface in his experiment is determined by optical study and Scanning Electron Microscopy (SEM). All the results related to the adherence tests were then combined and statistically compared with two studies: The Weibull analysis and the Principal Component Analysis (PCA).

Marine and automotive applications use polymers and aluminum grade materials which may be subjected to high strain rates [63]. In order to develop, integrate, and implement predictive computational models for CFRP composites that link the materials design, molding process, and final performance requirements, the dynamic mechanical response of unidirectional composites was characterized under various deformation rates. These were tested on an intermediate-to-high speed dynamic testing frame, equipped with high-speed cameras for 3D digital image correlation (DIC) [64]. Hence, Digital Image correlation is a very effective way for measurement of displacement and strain deformations. There is growing knowledge on using the non-contact strain measurement for measuring strain deformation in adhesively bonded single lap joints. Moreira used DIC to monitor the vertical and horizontal displacement fields of adherends and adhesive in the overlap region. Here, a large shear strain of order 48 % with an adhesive characterized by high flexibility was observed [65]. Digital image correlation method helped to develop damage zone models for Single Lap Joints by determining the critical damage zone and strain distributions. Here, the maximum principal strain was calculated from the shear and normal strains in the x and y-directions [66]. Yao and Zhu tested a FRP/steel hybrid lap joint under different temperatures and

different strain rates ranging from (0.625,1.25,2.5,5 m/s). The dynamic behavior at different loading speeds is captured by Phantom v7.3 high-speed digital camera at a sampling rate of 20,000 fps, and analyzed using a digital image correlation (DIC) method. Here, average bond strength, toughness, bond strength displacements, and FRP Strain distributions. It was concluded that the bond strength increases with the loading speed and the same trend is followed regarding shear stiffness and it was also observed that the high strain is near the joint edge where the load is applied as compared to the center of the overlapping area [38]. Cho conducted experiments to study the non- linear plastic behavior of DCB and TDCB specimens until a loading speed of 18.5 m/s and observed the strain energy ranged from 1-10 J/s [39]. A.J Comer has used high magnification 2D DIC to determine maximum principal strain in the adhesive bond and fillet area, and 3D DIC is used to measure the out of plane distortions and axial surface strain of the composite single lap joints. He concluded with a good correlation between the 3D DIC Measurement technique and strain gauges which measured the axial strain of the bonded surface [67]. A typical region of analysis used for determining the local and global strain distributions using digital image correlation method in single lap joints. The fracture process and adherend deformation were monitored by CCD Cameras in real life. The strain evolution is measured in adherend ends and along the bond-line. Figure 1.20 shows the region of analysis can be considered for DIC analysis. Aluminum – CFRP joints were analysed with various adherend thicknesses and adherend material and stated that as the adherend yield strength increases the joint strength increases and the strain deformations revelaed that the crack initiations of the joints with dismilar adherends are located in the lower end side of the adherend with less yield strength [68].

Figure 1.20 Region of Analysis for DIC.

Figure 1.21 shows the maximum principal strain at the adhesive fillet as a function of load level. Here the specific location of the strain deformation was determined using 2D DIC Analysis. 2D DIC results revealed that the high magnification has the potential to indicate the location of strain concentration in the bond-line and the magnitude of strain at this location as a function of applied

load. Consequently, this technique complemented the global full-field characterization provided by the 3D DIC technique [67].

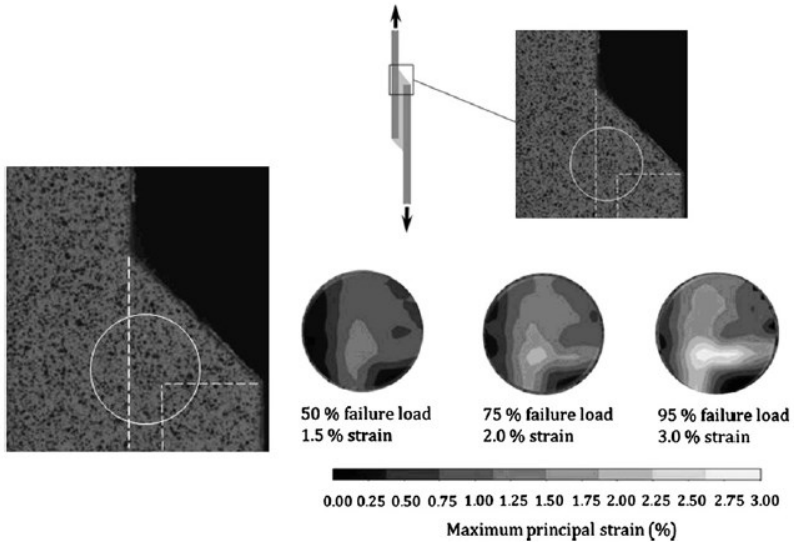


Figure 1.21 The maximum principal strain at the adhesive fillet as a function of load level.

## 1.6 Summary

An introduction to composite materials, adhesives, and aluminum alloys were discussed in this literature survey. The two types of joining in any industrial field which is mechanical fastening and adhesive bonding with their applications, advantages, and disadvantages were also discussed to understand the need for this research. From the review, it can be seen that mechanical fasteners have stress concentration at a point around the attachment location. Hence, an alternative method was adopted for the joining method which is adhesive bonding as this has advantages in decreasing the overall weight of the assembly and minimized galvanic corrosion compared to mechanical fasteners. Furthermore, adhesive bonding has great fatigue and mechanical shock resistance and the ability to bond dissimilar substrate materials as well as materials with different thermal coefficients. However, it is essential to be mindful of the joint configuration, surface treatment and curing requirements of the joint. Many papers have presented extensive research to understand the effect of these parameters on the joint strength. The crucial factor for the adhesion of aluminum substrates is its sensitivity to rust hence degreasing with acetone or $HNO_3$ was found out to be the best way to increase the adhesion of aluminum adherend to the adhesive. The effects of various

surface pretreatments on the surface roughness in case of polymer composites. Selection of adhesives concerning the application is also a crucial factor as considering the functionality of adhesive the adhesives can be divided into structural and non-structural adhesives. The choice of adhesive should be based on the application and adherends as well. Finally, the preparation of the joint to decrease the stress concentration has been discussed. Joint strength mainly depends on the adhesive thickness, overlap length, cure time & temperature and the pressure applied during the curing process. Furthermore, the stresses induced and failure modes in the adhesive joints when subjected to tensile loads have been discussed. In order to understand the behavior of the adhesive joints, experimental standards, numerical models and FEA analysis were developed for quasi-static conditions. Therefore, it is clear that in order to successfully join similar and dissimilar materials, it is necessary to have a better understanding of effect of using number of adhesives for structural applications. Moreover, the mechanical behavior of such joints needs to be investigated at various strain rates in order to be able to predict their performance when subjected to dynamic loading conditions.

## 1.7 Objectives

In this thesis, the effect of strain rate on adhesively bonded single lap joints of similar and dissimilar adherends (Aluminum and Carbon fiber composites) with a number of adhesives will be investigated. The experiments will be conducted based on three different sets of substrate combinations that included 1) Al6061 – Al6061, 2) Al6061–CFRP and, 3) CFRP-CFRP using three different adhesives that included a high strength epoxy, a quick set epoxy, and a urethane-based adhesive. The samples will be tested at different strain rates of 0.0015 $s^{-1}$, 0.15 $s^{-1}$,15 $s^{-1}$,150 $s^{-1}$. The slow strain rate/quasi static testing will be performed using Instron 5767 Universal Testing Machine. The high strain rate testing will be carried out on a hydraulic MTS test machine. Here, the bond strength and peak loads will be determined. In addition, global and local deformations, strain distributions within the materials will be examined using a high resolution non-contact strain measurement system. Finally, low magnification and optical microscopy analyses will be conducted to identify the resulting failure modes. In order to quantify the influence of adherend combination, adhesive type and strain rate on lap shear strength and peak strains, an experimental matrix will be designed and assessed using a statistical software MINITAB 18.0.

# Chapter 2. Experimental Procedure

## 2.1 Manufacturing Procedure

In this research project, a single lap joint configuration was adopted to understand the shear strength and peak load properties of the adhesive. The joint configuration is slightly modified from the ASTM standard D1002 and D5868 and extended the same application to composite-composite joints. A total of nine combinations were chosen which vary in their substrate combination and adhesive material. These lap joints were manufactured similarly to perform a comparative analysis concerning the similar and dissimilar adherends and change in the adhesive. Table 2.1 shows SLJ cases investigated under tensile loading conditions.

High-performance adhesive bonding requires precise bonding technique which can only be accomplished by proper fixturing. Special focus was placed to avoid typical defects associated while manufacturing lap joints such as void formation due to high viscosity and less work time, defects due to leaking of release agent between adhesive and adherend and defects arising while removing the lap joint from the fixture.

Table 2.1 SLJ cases investigated under tensile loading conditions.

| Case | Substrate 1 | Substrate 2 | Adhesive Thickness | Overlap Length | Adhesive Type |
|---|---|---|---|---|---|
| SLJ 1 | Al 6061 | Al 6061 | 1.00 mm | 15.5 mm | Quick set epoxy |
| SLJ 2 | Al 6061 | CFRP | 1.00 mm | 15.5 mm | Quick set epoxy |
| SLJ 3 | CFRP | CFRP | 1.00 mm | 15.5 mm | Quick set epoxy |
| SLJ 4 | Al 6061 | Al 6061 | 1.00 mm | 15.5 mm | High strength epoxy |
| SLJ 5 | Al 6061 | CFRP | 1.00 mm | 15.5 mm | High strength epoxy |
| SLJ 6 | CFRP | CFRP | 1.00 mm | 15.5 mm | High strength epoxy |
| SLJ 7 | Al 6061 | Al 6061 | 1.00 mm | 15.5 mm | Urethane-based system |
| SLJ 8 | Al 6061 | CFRP | 1.00 mm | 15.5 mm | Urethane-based system |
| SLJ 9 | CFRP | CFRP | 1.00 mm | 15.5 mm | Urethane-based system |

## 2.2 Materials

The materials considered as adherends in the current study are Aluminum 6061 – T6 and Carbon fiber reinforced polymer (CFRP). The single lap joints were obtained using three different adhesives which are a high strength epoxy, a quick setting epoxy, and a urethane-based adhesive. The adherend and the adhesives were used to bond similar and dissimilar adherend combinations were characterized in terms of their mechanical properties.

### 2.2.1 Adherends used

#### 2.2.1.1 Al 6061-T6

Al6061-T6 is a wrought alloy belongs in the 6000 series family with silicon and magnesium being alloyed by aluminum. The aging heat treatment applied is presented by the symbol T6. This alloy features good formability, workability, weldability, and machinability. It is important to understand the material properties to evaluate the behavior of the single lap joint under tensile loading conditions. Table 2.2 shows the mechanical properties of Al6061-T6. Al 6061 is typically used for heavy duty structures in rail coaches, truck frames, shipbuilding, bridges and military bridges, helicopter skins. The chemical composition of Al6061-T6 reported in Table 2.3 [69].

Table 2.2 Mechanical properties of Al6061-T6.

| Alloy & Temper | Ultimate tensile strength (MPa) | Yield Strength (MPa) | Elongation (%) in 50mm | Shear ultimate Strength (MPa) | Modulus of Elasticity (GPa) | Density (g/cm3) | Thickness (mm) |
|---|---|---|---|---|---|---|---|
| Al606-T6 | 310 | 275 | 12 | 205 | 69 | 2.7 | 2 |

Table 2.3 Chemical Composition for Aluminum alloy 6061-T6 adherend.

| | |
|---|---|
| Aluminum | 95.1-98.2% |
| Chromium | 0.04-0.35% |
| Copper | 0.15-0.4% |
| Iron | 0-0.7% |
| Magnesium | 0.8-1.2% |
| Manganese | 0.15% |
| Nickel | 0-0.05% |
| Silicon | 0.4-0.8% |
| Titanium | 0.15% |
| Zinc | 0.25% |
| Zirconium | 0.25% |
| Other | 0.15% |

#### 2.2.1.2 Carbon fiber reinforced polymer (CFRP)

CFRP is a black woven fabric comingled with epoxy resin to form a reinforced polymer. The primary element of this carbon fiber is a carbon filament which is from a precursor polymer known as polyacrylonitrile (PAN) and is spun into yarns. After undergoing the spinning and drawing operations, the carbon fiber is produced. The high strength and stiffness of this CFRP stand out from other polymers. The strength to weight ratio is very high when compared to Al6061 – T6. Table 2.4 shows the material properties of carbon fiber reinforced polymer [70].

Table 2.4 Material properties of Carbon fiber reinforced polymer.

| Material | Tensile Strength (MPa) | Compressive Strength (MPa) | Flexural Strength (MPa) | Density (g/cm3) | Thickness (mm) |
|---|---|---|---|---|---|
| Carbon fiber sheet | 827 | 517 | 613 | 1.66 | 1.58 |

### 2.2.2 Adhesives selected

#### 2.2.2.1 High strength epoxy

Epoxy-based adhesive by Fiber Glast can be used to bond a variety of materials and is very versatile. It is a two-component adhesive with a mix ratio of 1:1 by weight or volume. It has a 6-8 hr cure time at 77 $^{\circ}$F and 45 – 60 min cure time at 140 $^{\circ}$F. The cured material has excellent strength and good resistance to water, moisture, and weak acids. Table 2.5 shows the mechanical properties of high strength epoxy adhesive.

Table 2.5 Mechanical properties of high strength epoxy adhesive.

| Mixed viscocity | Tensile Strength (MPa) | Elongation at break (%) | Compressive Strength (MPa) |
|---|---|---|---|
| Smooth Paste | 49.65 | 6% | 98.59 |

#### 2.2.2.2 Quick set epoxy

Quick setting epoxy by JB Weld is a multipurpose adhesive which can bond to a number of parts including, brick, ceramic, concrete, epoxy & adhesives, fiberglass, glass, plastic/composite/PVC. It is a two-component adhesive. It has a high viscosity compared to high strength epoxy and a tensile strength of 30.33 MPa as per the manufacturer's website. The cure time is 6-8 hrs at room temperature and a set time of 5 min. Special attention was placed to avoid void formation during the manufacture of lap joints is more as the viscous nature of the adhesive takes more fixturing time than the set time.

#### 2.2.2.3 Urethane-based adhesive

The plastic bonder by JB Weld was chosen as it was a urethane-based adhesive which offers flexibility and can be used to bond plastics, composites and prepared metals. Urethane adhesives offer a good combination of tensile strength and ductility. They are sensitive to moisture as the isocyanate reacts with the system. Hence, care should be taken to avoid humidity conditions and on the substrates. The cure cycle of this adhesive was less than an hour at room temperature and

with a set time of 15 min. The tensile strength is a little low at 25.5 MPa, but the elongation at break is 300 % [42].

### 2.3 Bonding Procedure

The bonding procedure of the lap joints was divided into three parts: adherend surface preparation, adhesive placement, and adhesive curing.

#### 2.3.1 Joint Configuration

A total of nine combinations were fabricated and tested shown previously in table 2.1. A fixture is developed to achieve a similar joint configuration for all the single lap joints produced. This fixture helped was used to maintain the same adhesive thickness, width and an overlap length of the bond area, and constant pressure was applied throughout the specimen. The ASTM D1002 [15] and D5868 [16] standard test methods were used to evaluate the apparent shear strength of single-lap-joint adhesively bonded metal specimens by tension loading for similar and dissimilar adherends. Figure 2.1 shows a schematic representation of the SLJ geometry used in this research project. Here, the recommended overlap length was 12.7 ± 0.25 mm, and the computation for maximum permissible length was provided which showed that an overlap length of 15.5 mm would be permissible for the adherends chosen [15].

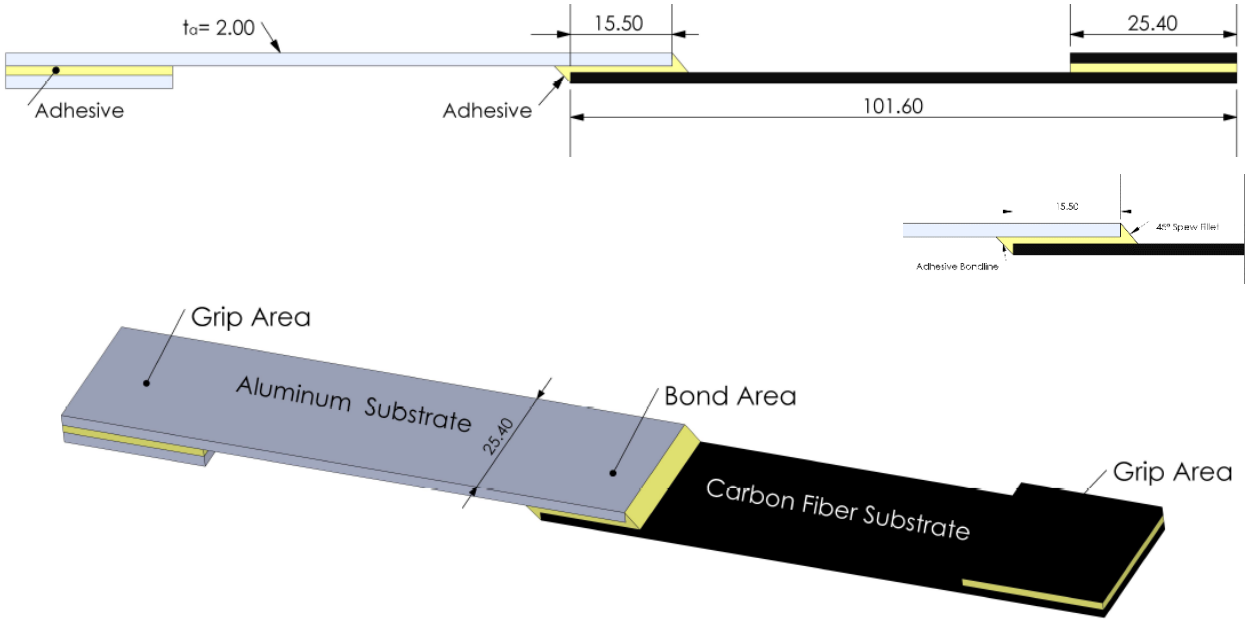


Figure 2.1 Schematic of single lap joint geometry (not to scale, dimensions in mm)

### 2.3.2 Adherend surface preparation

The aluminum 6061-T6 sheets were cut into 100 mm × 25 mm strips using an automatic variable speed pulley horizontal bandsaw, and the carbon fiber epoxy panels were cut in a similar manner using a tile saw cutter using a diamond coated wheel in an even manner and a specific surface preparation was chosen before the application of adhesive. Figure 2.2 (a) Horizontal wet cutting bandsaw (b) Wet tile saw with a diamond coated cutter.

Adherend preparation plays a critical role in the development of the strength of bonded joints. The bond strength increases by selecting the appropriate surface treatment and increased surface roughness as well. Hence, degreasing technique and surface roughening method were adopted for better adhesion of substrate and adhesive. The panels were cleaned and treated before bonding to eliminate surface contamination and promote adhesion. Here, to maximize the strength of the bond the surface was mechanical randomly abraded with a 180 Grit silicon carbide paper and cleaned with acetone for three times. The sanding operation was performed in order to remove any oxide layer formed and to increase the substrate roughness.

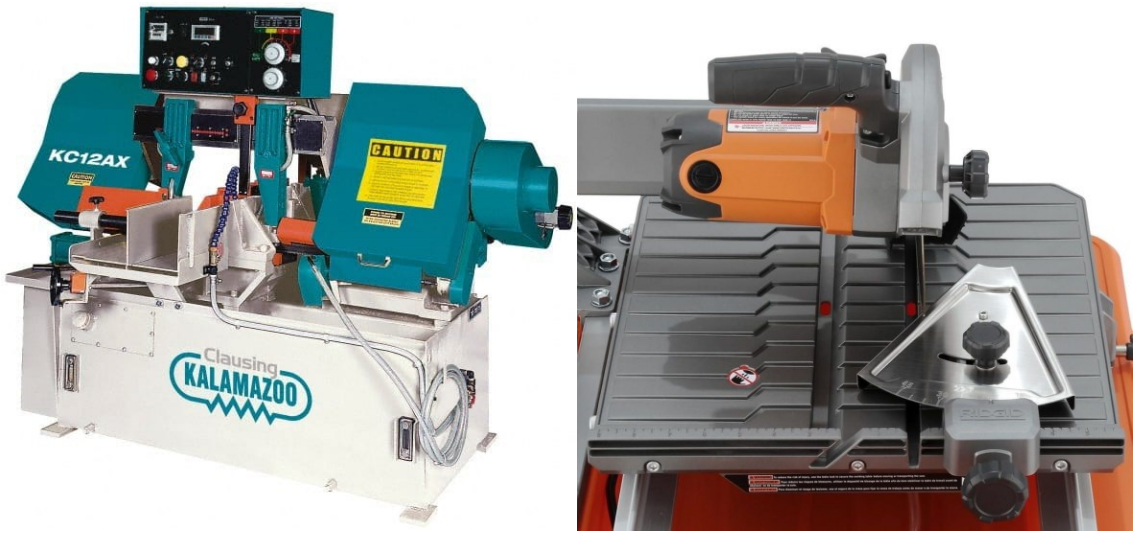


Figure 2.2 (a) Horizontal wet cutting bandsaw (b) Wet tile saw with a diamond coated cutter

### 2.3.3 Adhesive placement

A lap joint fixture was designed to manufacture all the specimens similarly as shown in figure 2.3 (a). The adhesive bond line thickness was controlled by using chamfered spacers in order to keep the thickness uniform. The use of chamfered spacers is one of the most effective ways to control the bond-line thickness and reduce the peel stress. The angle of the fillet was chosen to be 45° [17]. All the chamfered spacers were of the exact thickness required to produce a bond-line thickness of 1 mm for each joint. Positioning holes and fasteners were used to ensure minimum movement of the joint during the cure cycle. Then, the two-part adhesive is mixed as per the manufacturer's instructions and applied to the bond and grip area of the bottom panel. The top panels are placed in the position and pressure is applied, the excessive adhesive is removed, and the lap joint is allowed to cure for the required time and temperature. The high strength epoxy is cured for 45 min at a temperature of 140 F, quick set epoxy is cured for one hour at room temperature with applied pressure and fully cured in one day, and the urethane adhesive takes up to 45 min at room temperature to fully cure. Before positioning the joint on the bond fixture, Teflon sticker of different thickness was embedded on the surface of the fixture to ensure that the joint does not bond to the fixture. After the cure time was achieved and the adhesive was well set, the spacers were removed, and the lap joint was sanded using a polishing machine to remove any excess adhesive oozed out during the curing cycle. The specimens were then cleaned with water to remove dust accumulated during polishing. Figure 2.3 (b) shows a manufactured lap joint of Al-Al bonded with polyurethane adhesive.

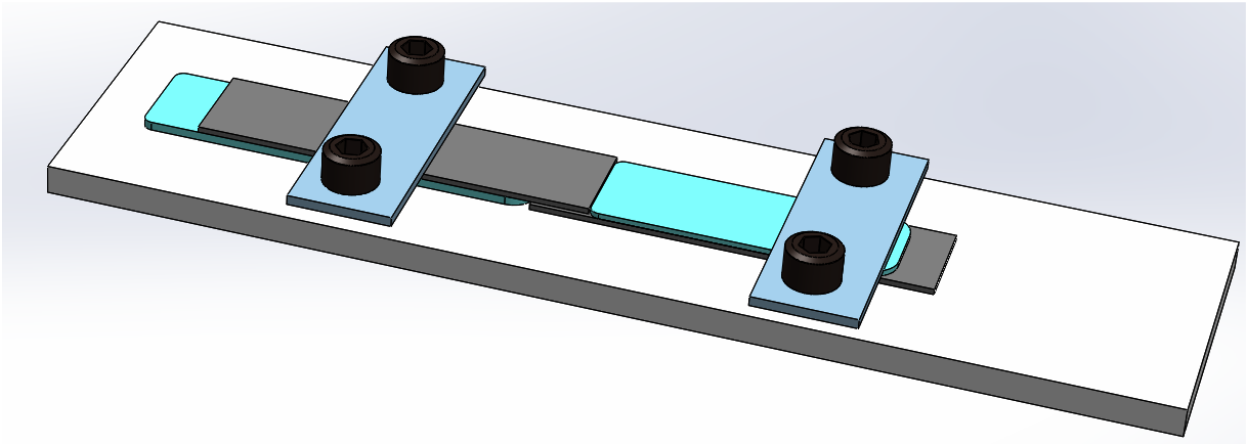

(a)

(b)

Figure 2.3 (a) Lap joint fixture overview (not to scale) (b) Manufactured lap joint

A nominal adhesive thickness was chosen as 1 mm after performing a round of quasi static testing of SLJ 1 with three different adhesive thickness (0.5 mm, 1.00 mm, 1.5 mm). Initial experimental results shown in the figure 2.4, for the single lap joints clearly highlight that thickness of 1.00 mm showed the maximum values of lap shear strength indicated by peak failure load and hence was chosen as a parameter to perform the experimental study.

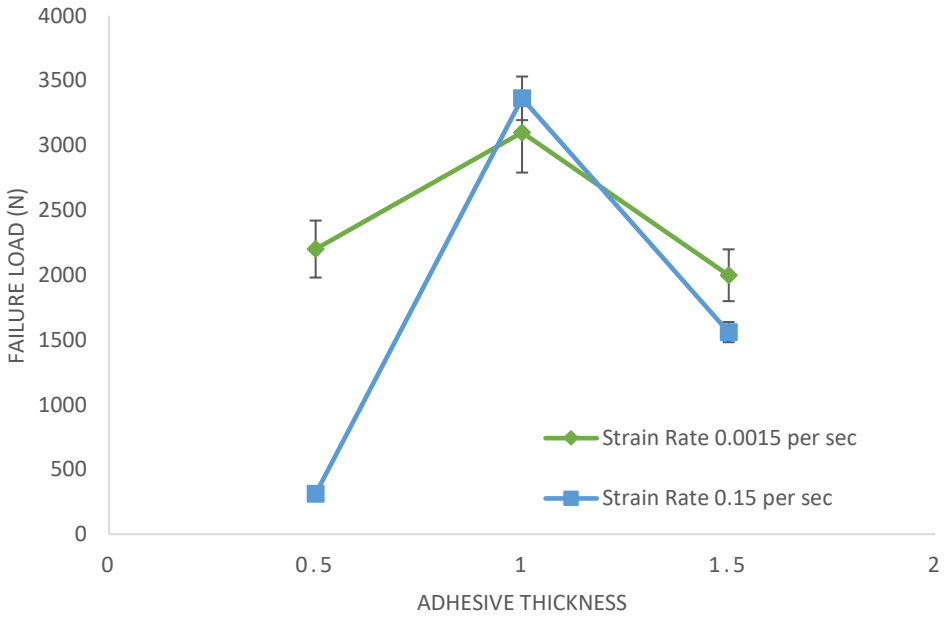


Figure 2.4: Effect of adhesive thickness for Aluminum - Aluminum SLJs.

## 2.4 Quasi-Static tensile testing

Initially, the single lap joints were tested on a universal testing machine with a load cell 30 KN under tensile loading conditions at a loading rate of 0.0015 $s^{-1}$ (1.4 mm/min) and 0.15 $s^{-1}$ (140 mm/min). While testing, the specimens were gripped with mechanical jaws and additional gripping was provided by placing #80 grit abrasive sheet between the end tab and mechanical wedges. Figure 2.5 shows the universal testing machine INSTRON 5967 to test under quasi-static tensile loading conditions.

During the testing the load and time data points were recorded. Additionally, local and global strain distributions were monitored using a non-contact strain measurement technique known as DIC.


Figure 2.5 INSTRON 5967 Universal testing machine

### 2.4.1 Introduction to DIC

In this research, DIC was mainly used to analyze and reveal deformations in order to understand the behavior of the lap joint during tensile loading conditions. The initial experimentation was performed using a 3D DIC Technique which required the calibration of two cameras. This technique was mainly used to understand the out-of-plane distortions components of the adhesive layer. It provided more extensive data; the system is more robust. Later in the research, a newly proposed technique was adopted by using a single-camera DIC technique for characterizing the deformation behavior of SLJ specimens subjected to tensile loads. Due to its compact and easy implementation, the 2D DIC technique was successfully to understand the strain distributions in the SLJ specimens. The only limitation is the sensitivity of the deformation with the movement of the tripod, tilting of specimen and bulging of the specimens. Figure 2.6 Difference in the principle of 2D (left) and 3D ( right) digital image correlation [71].

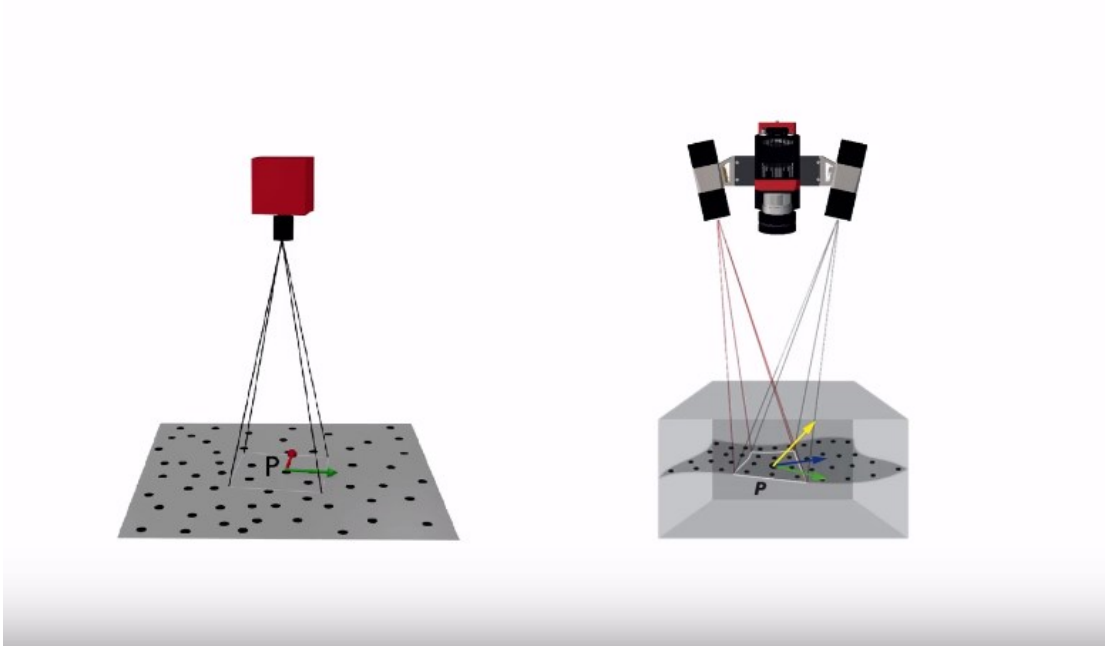


Figure 2.6 Difference in the principle of 2D (left) and 3D ( right) digital image correlation.

DIC primarily analyses, calculates and reports the material deformation. A graphical representation is shown in the results section to understand the behavior of the dissimilar and similar adherends with the change in the adhesive. The basic principle of DIC is to recognize the surface structure of the specimen and allocate pixels. During the deformation of the SLJ specimen,

pictures were the captured at a rate of one frame per sec for lower strain rate. Then the digital correlation process (ARAMIS System) determines the shift and rotation of the facet elements concerning the reference image (which is usually the first image). This procedure is used to determine the deformation of the adhesive layer in the specimen when the image plane of the camera is parallel to the sample. The primary operation of DIC is by tracking the pattern in the sequence of images. Hence, a pattern must be obtained on the sample for tracking. Figure 2.7 shows the basic principle of DIC measurement [72].

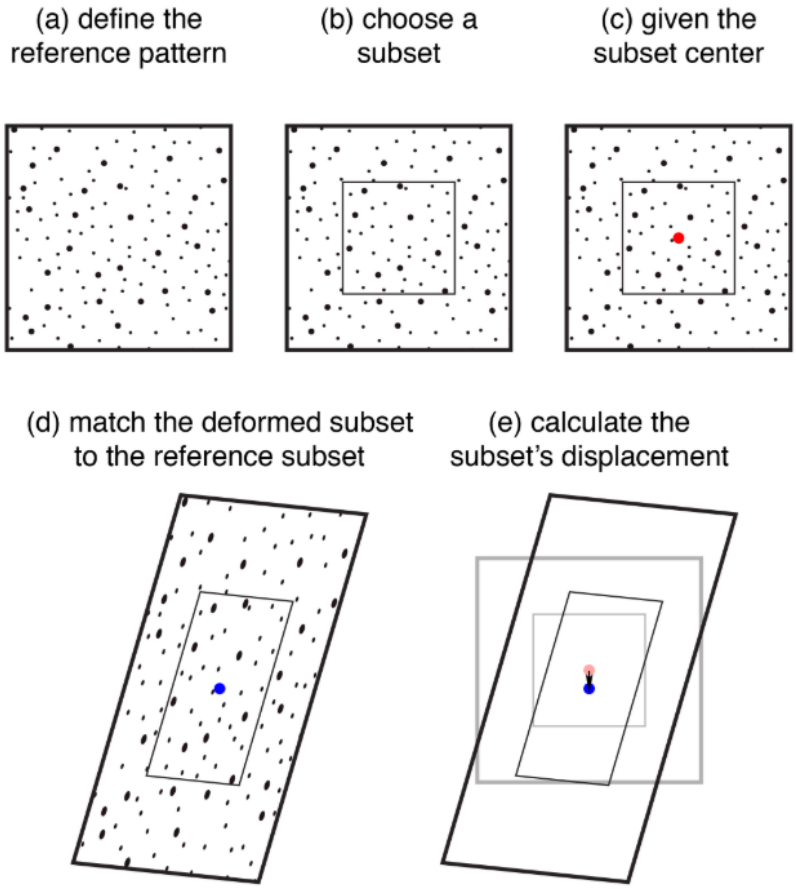


Figure 2.7 Basic operation of DIC analysis.

### 2.4.2 3D DIC

For the 3D DIC Deformation, two cameras are set up and calibrated before testing. The cameras used in this setup are Schneider 2.8/50 mm lens with a 43 mm lens filter. To calibrate the cameras the measuring volume was decided which determines the distance between sensor and specimens and the cameras. The measuring volume is chosen as 35 X 28 X 28 $mm^3$ for a 43mm lens with aperture 2.8. The measuring volume is selected concerning the specimen dimensions such that the specimen stays in the measurement volume until the break. Once the measuring volume has been decided, the system was calibrated by placing the sensors in the appropriate position concerning the field of view of the specimen. Figure 2.8 shows the calibration object used to calibrate the measuring volume using DIC.

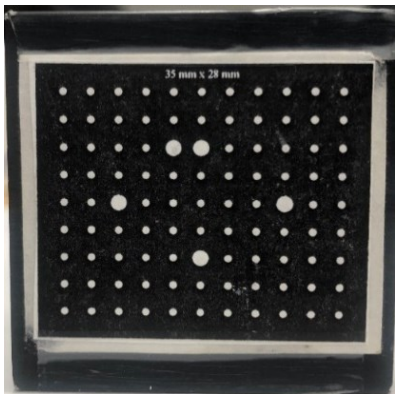


Figure 2.8 Calibration object for DIC

The sensor configuration is analyzed after determining the measuring volume to calibrate the sensors using the cube calibration panel. As per Aramis sensor configuration for a focal length of 50 mm and aperture 2.8, the base should be maintained 110 mm, the min length of camera support is 500 mm and measuring distance is 305 m with a camera angle maintained at 25 degrees, and the ellipse quality should be maintained between 0.6-0.8 after calibration. Figure 2.9 shows the 3D sensor setup unit for calibration process [72]. Figure 2.10 Setup for calibrating the cameras using the cubic panel.

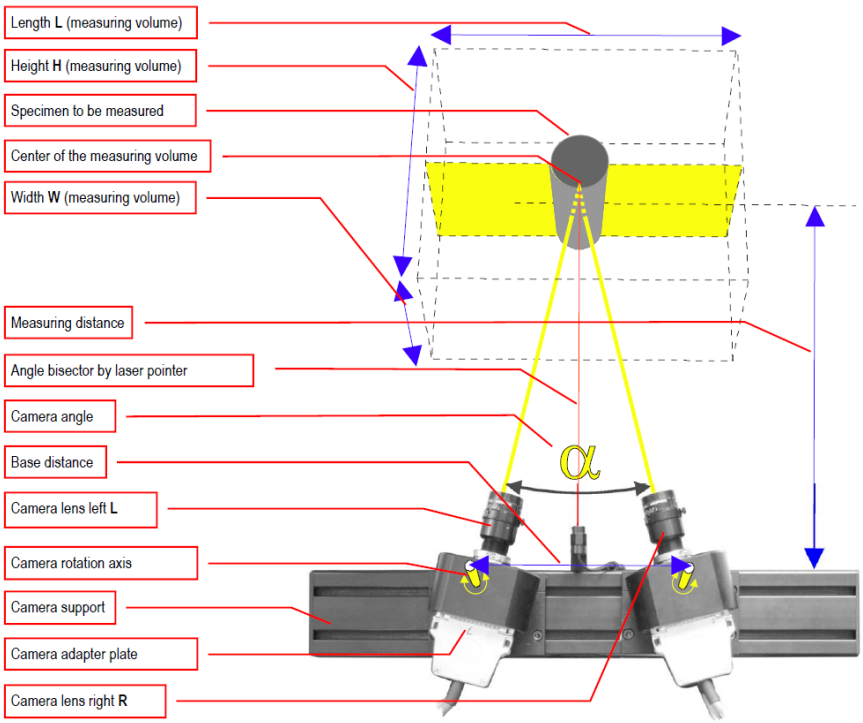


Figure 2.9 3D sensor unit in top view

To complete the calibration process as shown in figure 2.10:

1. The calibration object was placed in the center of measuring of measuring volume. A fixture was designed to fix the calibration panel in a position.
2. Calibration panel was defined, and the ellipse quality was set to 0.8.
3. The shutter time was set as 42 ms to avoid overexposing of the calibration object
4. The calibration images were recorded in 13 positions as shown in the instruction window of DIC.
5. Once the recording was done, the calibration deviation was below 0.04 after computation.

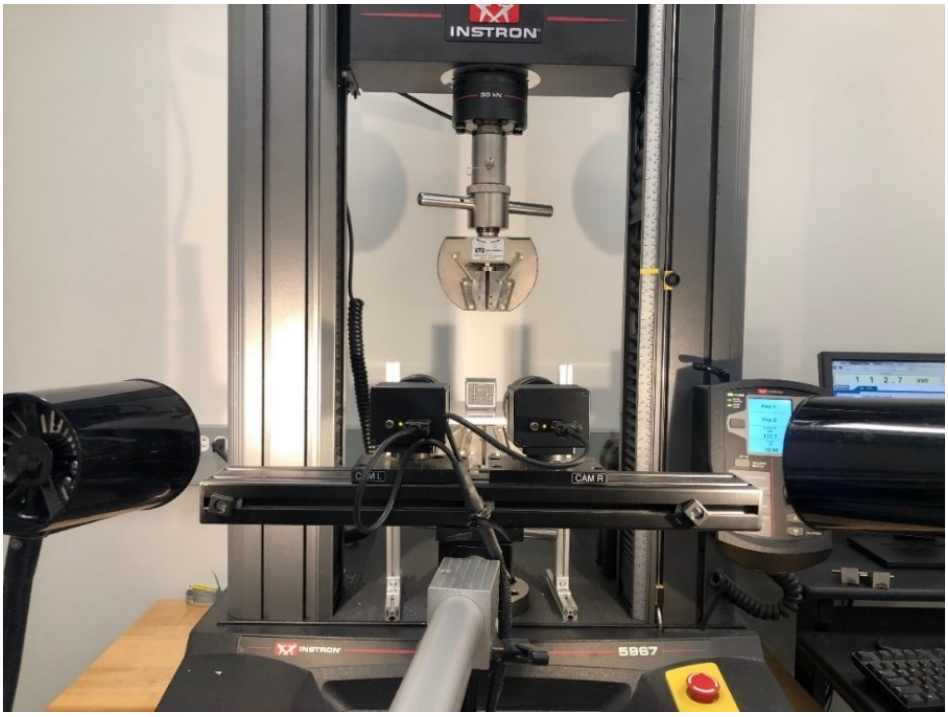


Figure 2.10 Setup for calibrating the cameras using the cubic panel.

Since the field of view was very small, special attention was placed to avoid any mechanical obstacles, like vibrations, even thermal fluctuations (from lights) that could influence the measurements. Following this, the sensors are ready to record the deformation of the specimen. However, to analyze the image in the DIC Software, the specimen needs to be prepared with a high contrast stochastic pattern with conventional spray paint to allocate the pixels in the picture as shown in figure 2.11. The quality of the speckle pattern was determined by comparing it with the one provided by ARAMIS for the chosen measuring volume. The reliability of DIC depends on this high-contrast random pattern applied to the specimen. The design was not made too sparse, too dense, or the speckles too large as the spatial resolution of the measurement will suffer. Once the speckle pattern was established, the recording mode was switched on to capture the deformation pictures at one frame per sec. The pictures were further analyzed to understand the strain distribution and further post-processing techniques in DIC were used to extract the results required. Figure 2.12 shows experimental setup for quasi-static tensile testing using two cameras for a 3D DIC setup.

Figure 2.11 Typical speckle pattern required for DIC measurement.

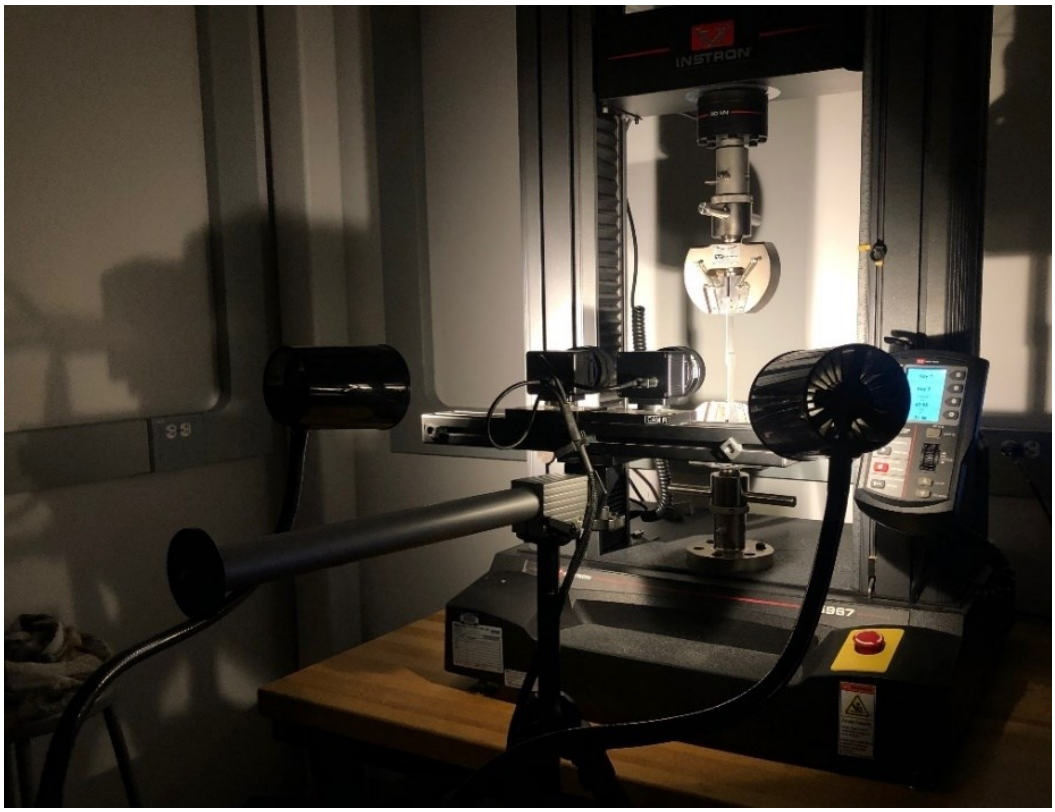


Figure 2.12 Experimental setup for quasi-static tensile testing using two cameras.

From the testing machine, the load and time data were extracted, and similarly, from DIC software, the linear technical strain (%) was obtained by creating a point-point analysis on the reference image. This analysis allows exporting of the engineering strain data concerning time. Then, the time can be correlated with nominal shear stress and engineering strain to obtain stress vs. strain curve. From here, the elastic modulus, shear stiffness, and Poisson's ratio can be determined.

### 2.4.3 2D DIC measurement

The implementation of the 2D DIC technique required only three consecutive steps: (a) preparation of specimen and experimental setup (b) recording images in a single plane during the test (c) processing the images in software. The cumbersome process of calibrating the cameras in 3D technique can be avoided in the 2D technique. Here, the camera needs to be mounted perpendicular to the specimen surface, and most crucial part is to make sure they remain in the same plane perpendicular to the camera during the test [73]. The fixture designed for calibrating the image sensor was used to fix the camera to the plate with the help of a mounting screw. With this process, the camera remained fixed to the position throughout the test. The 2D measurement can only measure in-plane displacement, and any out-of-plane deformation was neglected. The images were captured using the Flea3 USB3 Vision camera in combination with a 20 mm focal length lens which offered a maximum frame rate of 60 fps. In this project, the experimental tests for strain rate 0.0015 s-1 were recorded with one fps and 60 fps for 0.15 $s^{-1}$. The camera remained in a fixed position concerning specimen throughout the test. Figure 2.13 shows the DIC setup required for in-plane displacement measurements.

The specimen was prepared with the random speckle pattern just as shown in 3D DIC measurement technique and analyzed in DIC software. In the DIC software, a new project was created with a 2D dimension, and project parameters were established before importing the images acquired from the test. The facet size was set as 11 and facet step as 4, these account to a validity quote of 55 % with the linear computation of strain. Once these were established, the image series were imported from the stage. The images need to be numbered in series and should be in a .tif format. Then, these images should be computed by choosing start points in the reference image. After the processing of images, the post-processing was performed in the evaluation mode, and 2D parameter was given to the project. This 2D parameter is generally the gage length of the specimen which was the overlap length of the bond in this case. Many post-processing techniques can be used to understand the behavior of the test coupon. Figure 2.14 shows the experimental setup to carry out quasi-static testing using a single camera.

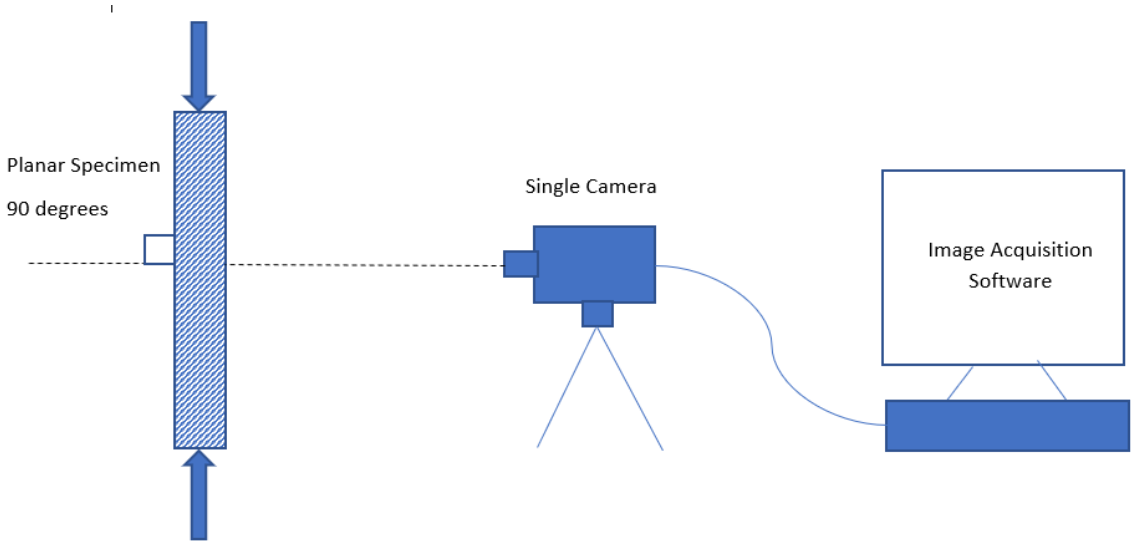


Figure 2.13 DIC Setup for in-plane displacement measurement.

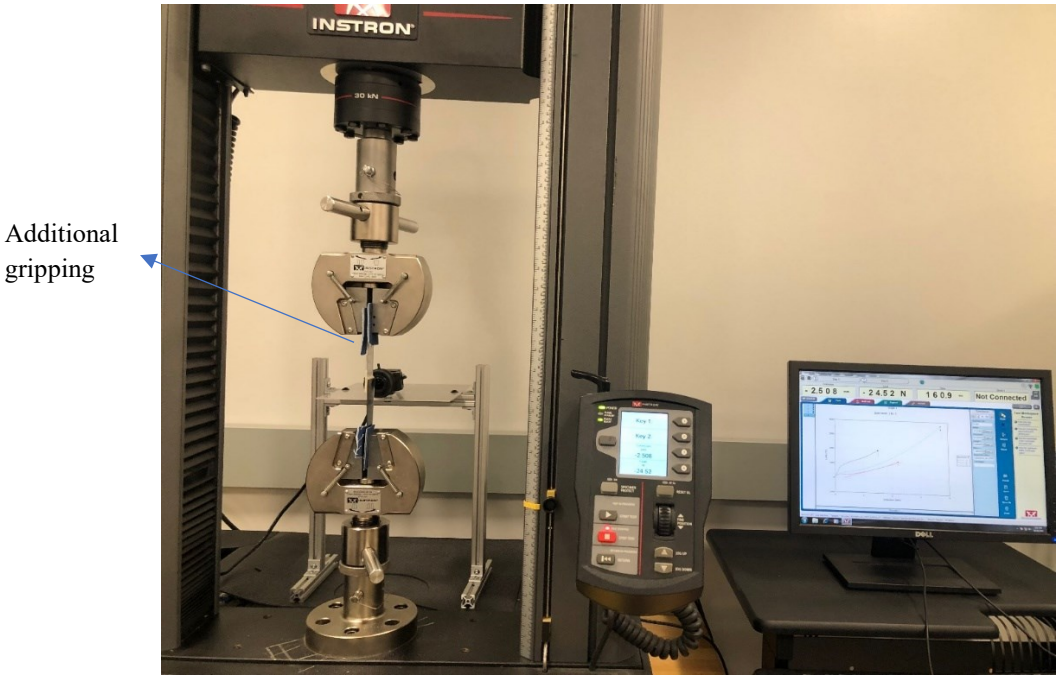


Figure 2.14 Experimental setup for quasi-static tensile testing using a single camera

## 2.5 Dynamic tensile testing

Dynamic testing was performed on the manufactured SLJ specimens at loading rates of 15 $s^{-1}$ (14000 mm/min) and 150 $s^{-1}$ (140000 mm/min). The digital images to compute for strain distribution are obtained from Photron APX-RS High-speed cameras. These images are analyzed in DIC using 2D deformation technique similar to quasi-static testing. An integrated imaging software (Photron FASTCAM analysis) was used to save the digital images, perform image enhancement and create simple motion analysis. A servohydraulic machine was used with a load capacity of 50 KN and self-tightening grips. A hydraulic power unit (HPU) is used to activate the actuators which in turn move the crosshead at the desired velocity. It was assumed that the actuator velocity was equal to the specimen deformation rate and the required actuator velocity can be estimated based on the needed strain rate and gage length. Figure 2.15 shows procedure followed for high strain rate testing [75]. Figure 2.16 Schematic of high strain rate testing system [76].

The high strain testing works on the kinetic energy concept where the energy supplied to break the specimen should be significantly higher than the energy to break the specimen. This process can be achieved by storing the energy in an accumulator and then providing it to the actuators while testing as the HPU reacts very slowly. As the test is initiated, the stroke is opened, and the stroke accelerates until it reaches the predetermined velocity and this constant velocity is transferred to the specimen using the slack adapter. The slack adapter mainly reduces the inertia effect of the upper grip. The adapter connects with the specimen, and the actuator was raised so that the distance is slightly higher than the actual distance required for the specimen to break. To reduce inertia, lightweight grips were used for dynamic tensile testing this clamping system is critical to ensure minimum ringing os the system which is the cause of load oscillation [74]. Figure 2.15 shows the procedure followed for high strain rate testing [75].

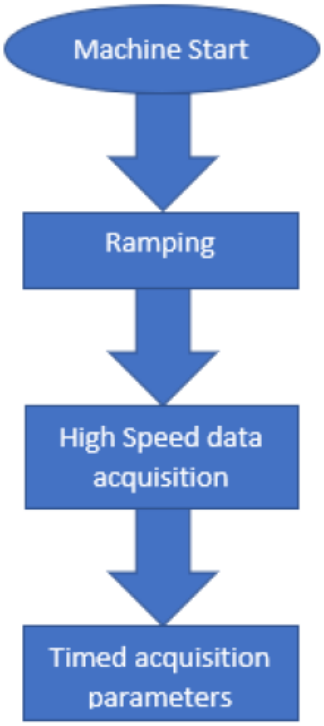


Figure 2.15 Procedure followed for high strain rate testing.

The grips used for holding the specimen were designed to clamp it firmly without any slip. The potential issue of the MTS was found out to be load ringing in the stress-strain curve as the slack adapter components were slamming together and reaching its resonance frequency which in turn vibrates the load frame. Hence, this noise was eliminated from stress-strain curves presented in the result section. MTS had different channels to render data acquisition varying from load transducer data, actuator displacement, time step, and test setup. Data were collected at a frequency at a sampling rate of 6544 Hz. Figure 2.16 shows the schematic of high strain rate testing system [76].

Actuator velocity = original specimen gage length * strain rate.

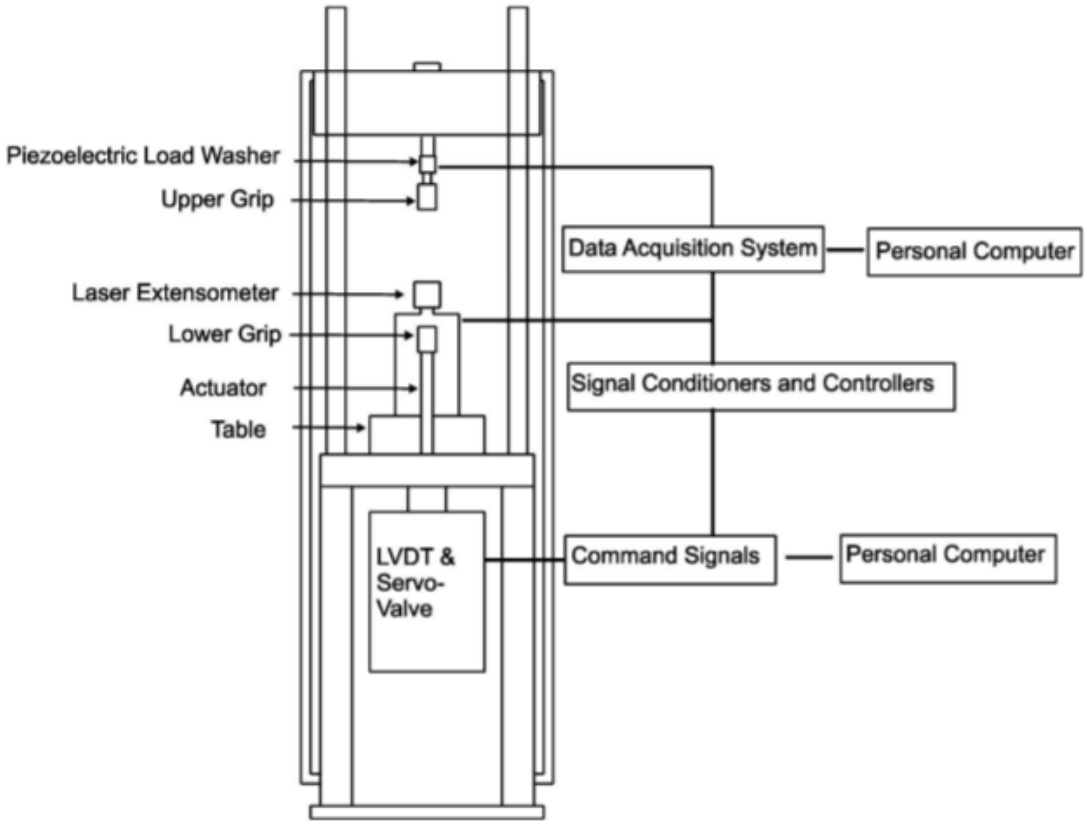


Figure 2.16 Schematic of high strain rate testing system.

### 2.5.1 Photron FASTCAM Viewer

In order to analyze the deformation of the specimens using the 2D DIC technique, a single camera of Photron APX-RS camera with a 75 mm focal length lens was used to capture the digital images during deformation. PFV was used for controlling the cameras and perform operations like setting camera options, shooting and saving images to the PC. Various camera settings need to be controlled to capture images. These varied from frame rate, shutter speed, resolution.

In this research project, the SLJs were tested under dynamic conditions at two strain rates, i.e., 15 $s^{-1}$ and 150 $s^{-1}$. To perform analysis on DIC for strain deformation at least 50 pictures were recommended. Hence, the frame rate to capture the test was estimated by understanding the duration of the test under the quasi-static loading conditions. The duration of the test was estimated to be around 0.015-0.02 secs for strain rate 15 $s^{-1}$ and 0.0015-0.002 secs for strain rate 150 $s^{-1}$.

Following this, the sampling rates of 5000 fps and 21000 fps were chosen with a resolution of 256 × 512 pixels and 256 × 384 pixels so that the failure modes could be examined in detail.

Once the specimen was clamped in the grips and mounted on the test machine, high-intensity fiber optical lights were used to illuminate the surface of interest so the cameras could capture the images. Now, the camera was calibrated after establishing the frame rate and resolution, and the trigger mode was set to 'start.' Simultaneously the MTS test system was set up by turning on the actuators, and the manual control was turned on to move the specimen to the zero position. The images in the PFV were captured using trigger mode 'start.' The MTS test and the PFV were started at the same time with the help of external trigger attached to the camera. Once the recording was complete, the images were filtered from the beginning to end of the test and saved. These images were analyzed in the DIC software using the 2D DIC technique discussed before. Vibrations were observed during the processing which were attributed to noise in the DIC strain deformations. This noise was removed by using rigid body motion and interpolation of 2D points techniques in the post-processing stage of DIC. Figure 2.17 shows experimental setup used for performing high strain rate testing on single lap joint specimens.

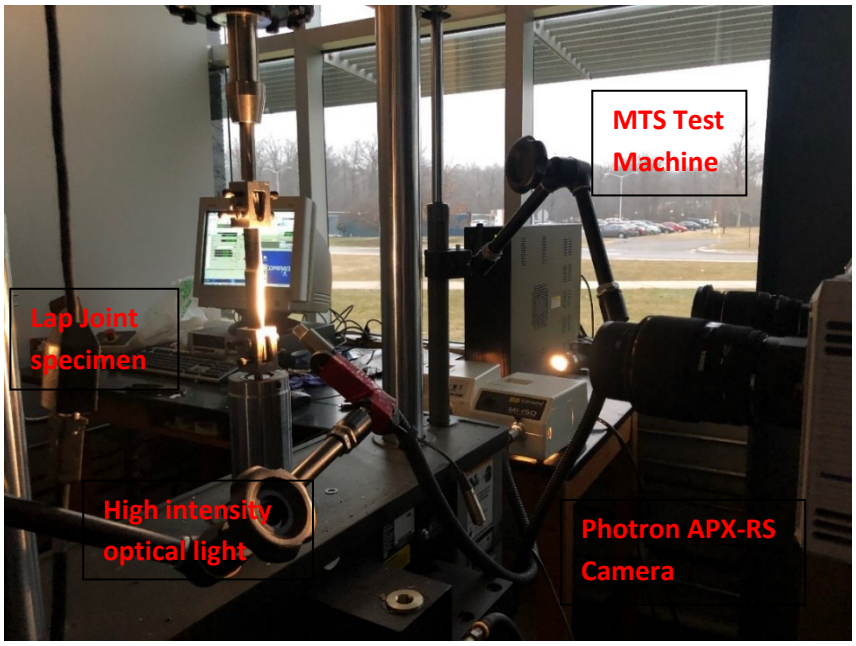


Figure 2.17 Experimental Setup for high strain rate testing.

## 2.6 Optical Microscopy

Tested samples under quasi-static and dynamic loading conditions were examined using an optical microscopy technique in order to understand the failure modes at break. Two types of analysis were performed on the specimen which included low magnification analysis and optical microscopic analysis with 10 x zoom. The low magnification images revealed the failure modes of the specimen using an HP Scanjet 3970. This procedure produced high-quality images of the fracture surface. The optical microscopy analysis was performed to deeply understand the modes of failure in composites and aluminum substrates and the behavior of adhesive with the change in strain rate. This was performed using an advanced metallurgical microscope with 5 MP digital camera at 10 x magnification. The light is illuminated on the specimen from the top which allowed to see the fracture surface. It has a built-in reduction lens which gives the same field of view on the PC which is seen through eyepieces. These images were captured and post-processed in the software. Figure 2.18 shows the optical microscope used to understand the fracture surface of the SLJ specimens after the break.

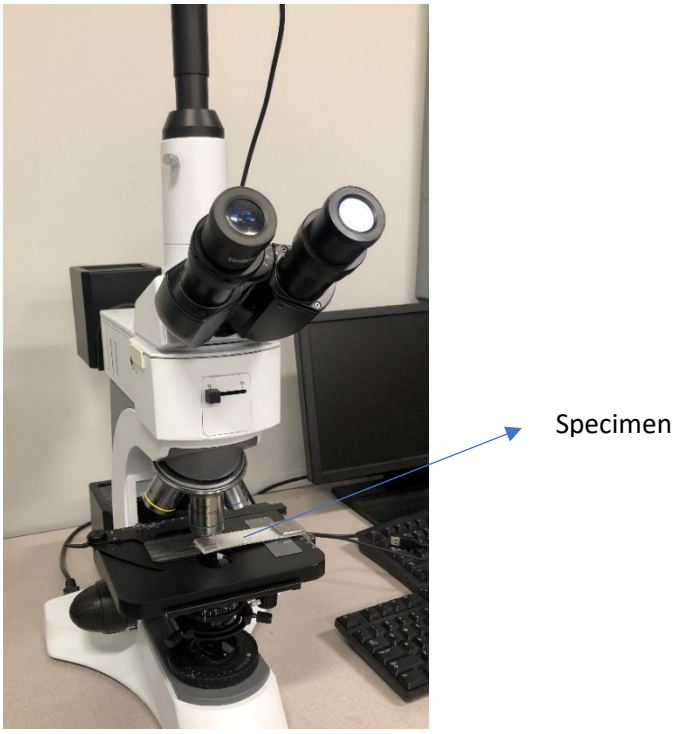


Figure 2.18 Optical Microscope used to examine the fracture surfaces.

# Chapter 3. Results and Discussion

## 3.1 Quasi-Static Tensile properties

In this research project, single lap joints were experimentally tested under Quasi-static and quasi-dynamic loading conditions. Tensile testing was performed in order to investigate their mechanical behavior. Furthermore, the local and global strain were obtained using a non-contact strain measurement technique. Under quasi-static testing, the manufactured lap joints were subjected to tensile loading conditions on the universal tensile machine. Analysis of results and fracture surfaces will be presented in this section. Based on the analysis and observations, some conclusions will be drawn, and further studies can be performed based on these results. Figure 3.1 (a) Typical failure modes associated with adhesively bonded single lap joints under tensile loading conditions (26) (b) Specialized failure modes [78].

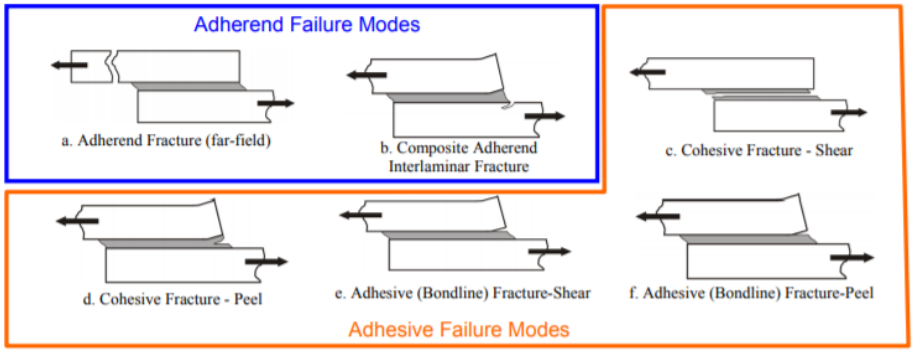


(a)

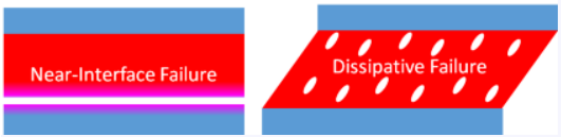


(b)

Figure 3.1 (a) Typical failure modes associated with adhesively bonded single lap joints under tensile loading conditions [26] (b) Specialized failure modes [78].

### 3.1.1 Aluminum – Aluminum joints

In these joints, an aluminum alloy 6061 – T6 was bonded to aluminum 6061 – T6 with three different adhesives. Three combinations were tested after manufacturing into a single lap joint configuration. These lap joints were tested on an INSTRON 5967 under tensile loading conditions at strain rates of 0.0015 $s^{-1}$ and 0.15 $s^{-1}$ and the resulting data was analyzed.

#### 3.1.1.1 Al 6061-Al 6061 with high strength epoxy

Figure 3.2 shows typical stress-strain curves for Al-Al SLJ bonded with high strength epoxy subjected to a strain rate of 0.0015 $s^{-1}$. Here, the average lap shear strength of the graph was observed to be 5.25 MPa and an average peak strain of 0.135 %.

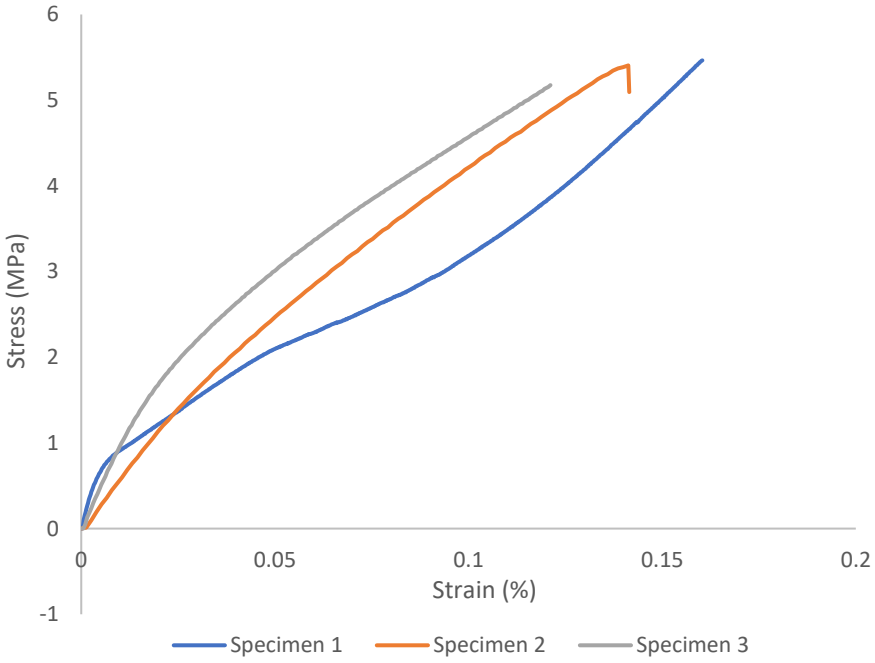


Figure 3.2 Typical stress-strain curve of al-al joint bonded with high strength epoxy subjected to a strain rate of 0.0015 $s^{-1}$

Figure 3.3 depicts a low magnification image after fracture for Al-AL SLJ bonded with high strength epoxy subjected to a strain rate of 0.0015 $s^{-1}$. From the figure, it can be seen that failure

is an interfacial fracture between adhesive and adherend. Moreover, there is no residue from the adhesive on the adherend which can be observed from the optical micrograph image captured at 10x zoom. It can even be understood that the brittle nature of this adhesive could be the reason for the interfacial failure when bonded to the aluminum adherend. Figure 3.4 shows the optical microscopy image after fracture at ×10 magnification of Al-Al bonded with high strength epoxy subjected to a strain rate of 0.0015 s-1.


Figure 3.3 Low magnification image after fracture of Al-Al bonded with high strength epoxy under tensile loading conditions at a strain rate of 0.0015 $s^{-1}$

Figure 3.4 shows an optical microscopy image after fracture at ×10 magnification of Al-Al bonded with high strength epoxy subjected to a strain rate of 0.0015 s-1. From figure 3.4, it is evident the aluminum adherend was abraded with a 180 Grit silicon carbide sheet to increase the adhesion between the epoxy and substrate. Hence, the micrograph mainly depicts the rough surface of the aluminum substrate after surface treatment and the fact that no residue was left on the substrates.

Figure 3.5 shows a DIC strain distribution map near to failure for Al-Al SLJ bonded with high strength epoxy subjected to a strain rate of 0.0015 $s^{-1}$. It can be noted that the peak strain is propagating from the Peel region in the top and bottom towards the middle. This behavior further confirms that the interfacial failure between adherend and adhesive is due to peeling.

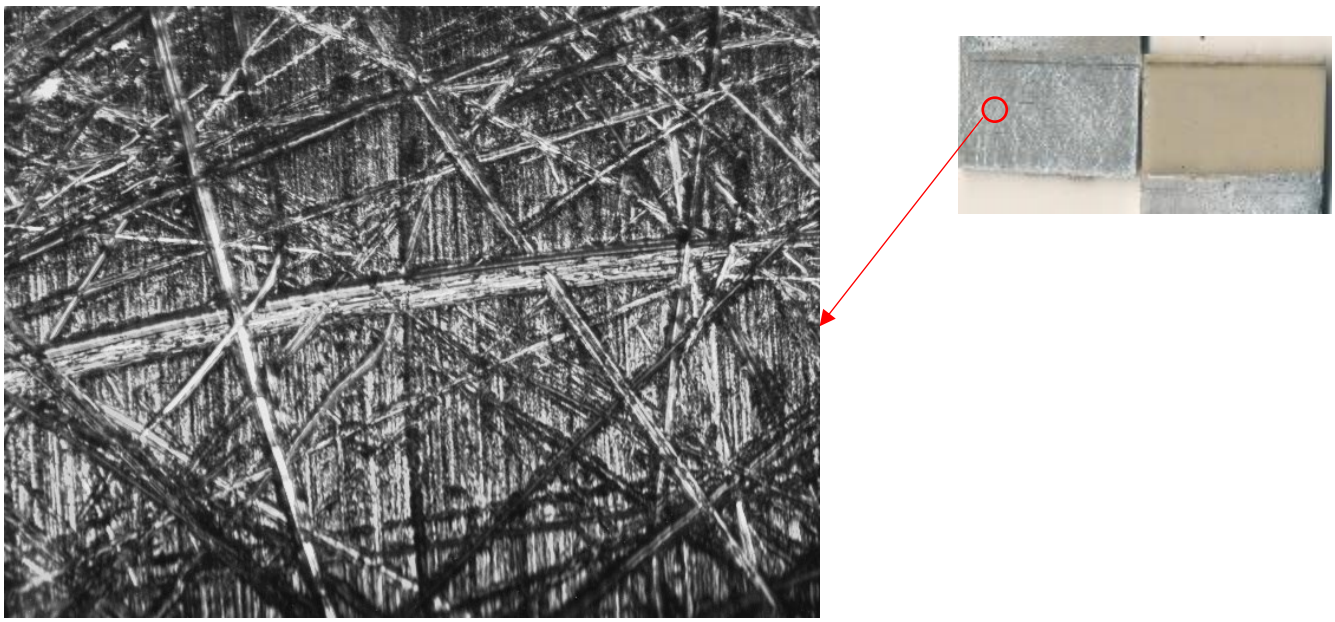

Figure 3.4 Optical Microscopy image after fracture at ×10 magnification of Al-Al bonded with high strength epoxy subjected to a strain rate of 0.0015 $s^{-1}$.

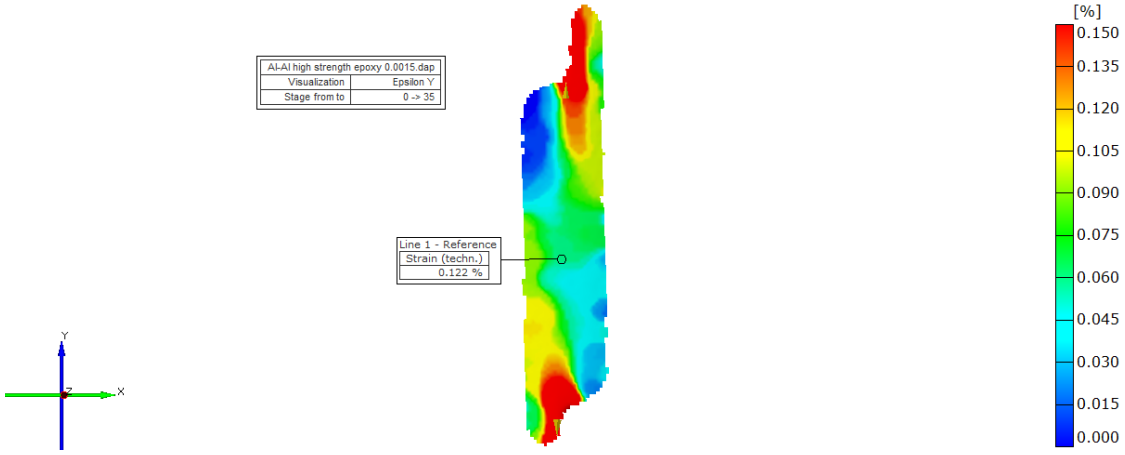


Figure 3.5 DIC distribution of Al-Al SLJ bonded with high strength epoxy subjected to a strain rate of 0.0015 $s^{-1}$.

Figure 3.6 shows typical stress-strain curves for Al-Al SLJ bonded with high strength epoxy subjected to a strain rate of 0.15 $s^{-1}$. Here, the average lap shear strength of the graph was observed to be 7.55 MPa and an average peak strain of 0.111 %.

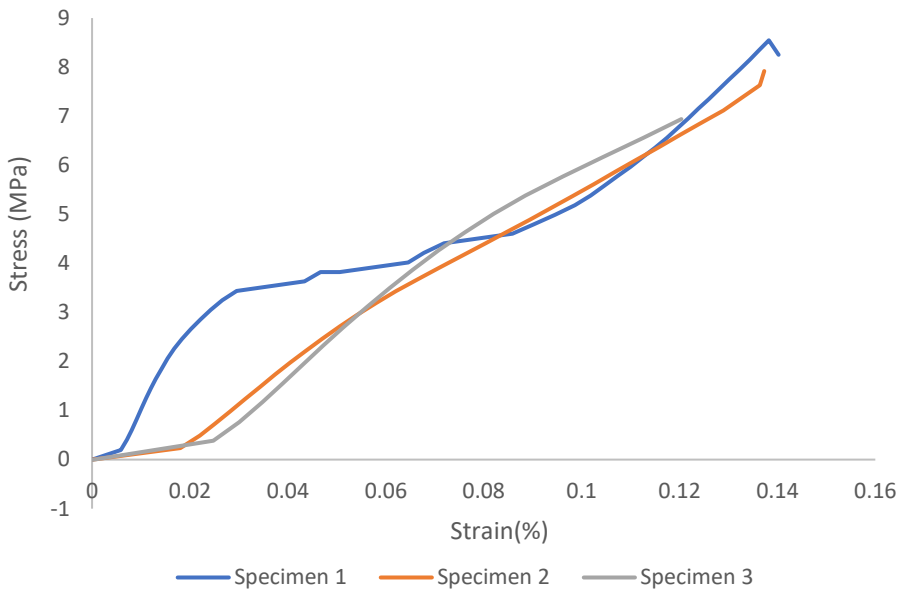


Figure 3.6 Typical stress-strain curve of al-al joint bonded with high strength epoxy subjected to a strain rate of 0.15 $s^{-1}$

Figure 3.7 depicts a low magnification image after fracture for Al-AL SLJ bonded with high strength epoxy subjected to a strain rate of 0.0015 $s^{-1}$. From the figure, it can be seen that it is a mixed mode failure with interfacial fracture between adhesive and adherend and some amount of cohesive failure in adherend due to the uncured adhesive during manufacturing.


Figure 3.7 Low magnification image after fracture of Al-Al bonded with high strength epoxy under tensile loading conditions at a strain rate of 0.15 $s^{-1}$

Figure 3.8 depicts the DIC distribution in the adhesive bondline region for Al-Al SLJ bonded with high strength epoxy subjected to a strain rate of 0.15 $s^{-1}$. It can be seen that the peak strain for the particular specimen was 0.141 % with the strain accumulated in the bottom adhesive region which could have started the crack initiation in the adhesive and in turn caused an interfacial failure.

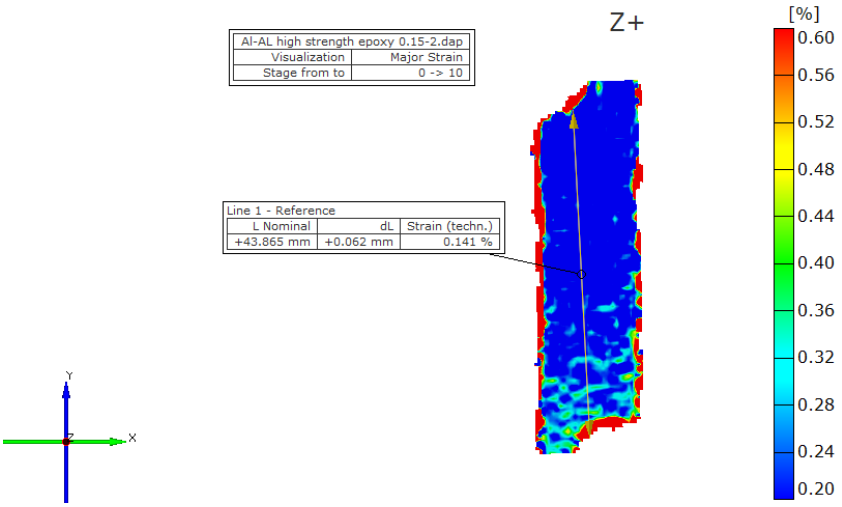


Figure 3.8 DIC distribution of Al-Al SLJ bonded with high strength epoxy under tensile loading conditions at a strain rate of 0.15 $s^{-1}$.

### 3.1.1.2 Al 6061-Al 6061 with quick set epoxy

Figure 3.9 shows typical stress-strain curves of Al-Al joint bonded with quick set epoxy under tensile loading conditions at a strain rate of 0.0015 s-1. The lap joint was analyzed based on the lap shear strength and peak strain, and it can be seen from the graph that the lap joint exhibited an average shear strength of 2.48 MPa and a peak strain of 0.92 %.

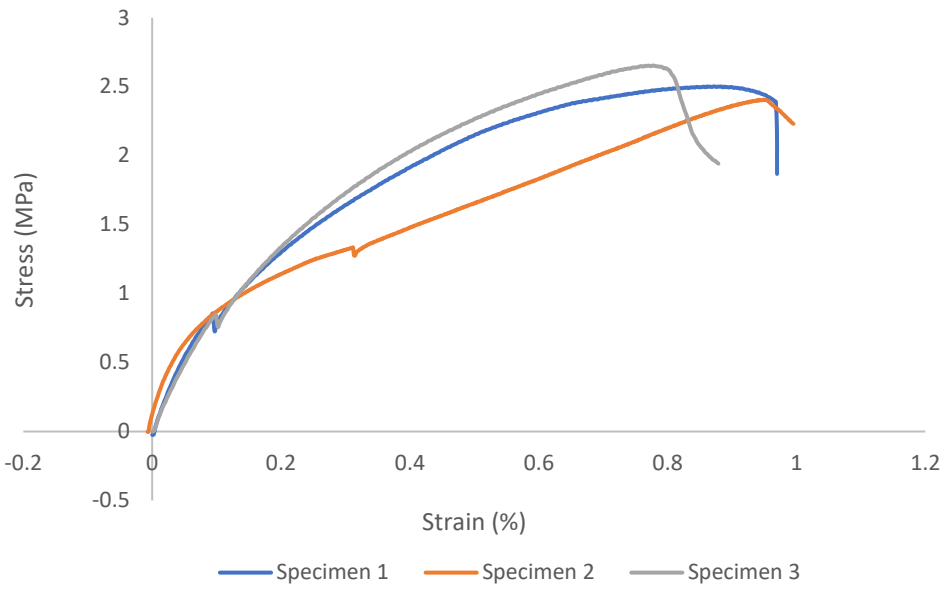


Figure 3.9 Typical stress-strain curves of Al-Al joint bonded with quick set epoxy under tensile loading conditions at a strain rate of 0.0015 $s^{-1}$

Figure 3.10 shows a low magnification optical microscopy image after the break for Al-Al SLJ bonded with quick set epoxy when tested under tensile loading conditions at a strain rate of 0.0015 $s^{-1}$. From the Figure 3.10, the failure mode can be observed as the interfacial failure between the adhesive and adherend due to shear and due to large absorption of energy with the adhesive system, there is some dissipative failure.


Figure 3.10 Low magnification image after fracture of Al-Al bonded with quick set epoxy at a strain rate of 0.0015 $s^{-1}$

Figure 3.11 shows an optical microscopy image captured at 10 × magnification of Al-Al SLJ bonded with quick set epoxy tested under tensile loading conditions at a strain rate of 0.0015 $s^{-1}$.

The figure depicts the bond area of the aluminum adhered with the adhesive to understand the behavior of quick set epoxy adhesion to aluminum adherend. It was observed that the adhesion between epoxy and adherend is good. Moreover, the dissipative forces in the adhesion when subjected to loading can be observed due to the formation of pores on the surface.

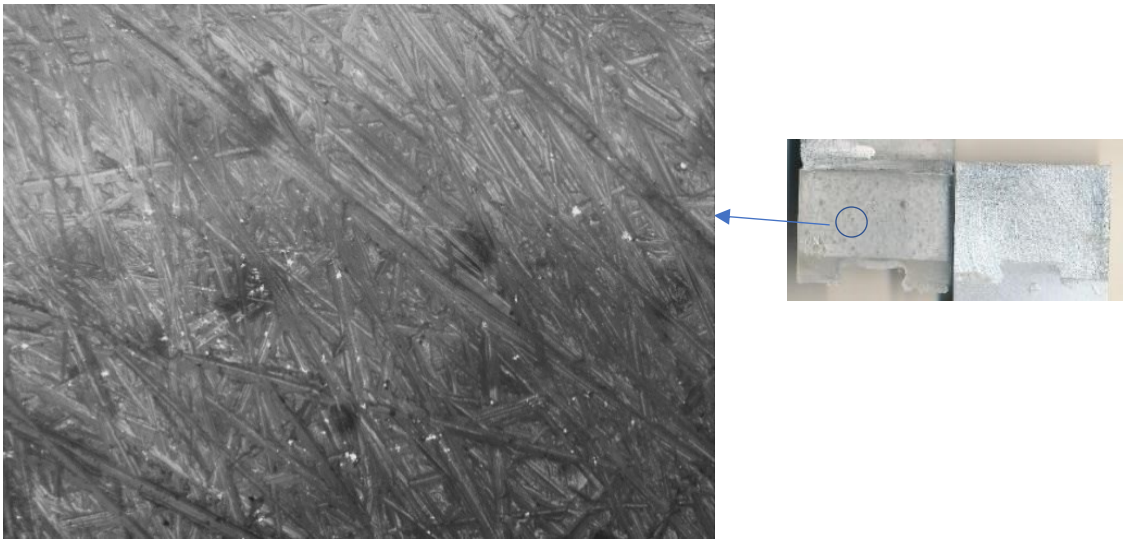

Figure 3.11 Optical Microscopy image at 10× magnification Al-Al bonded with quick set epoxy at a strain rate of 0.0015 $s^{-1}$

Figure 3.12 shows a DIC strain distribution map near to failure for Al-Al SLJ bonded with quick set epoxy subjected to a strain rate of 0.0015 $s^{-1}$. It can be seen that the peak strain is localized in the top region of adhesive and adherend due to peeling and propagated to the bottom until failure. The peak strain obtained from the point-point analysis for the particular specimen is 0.828 %.

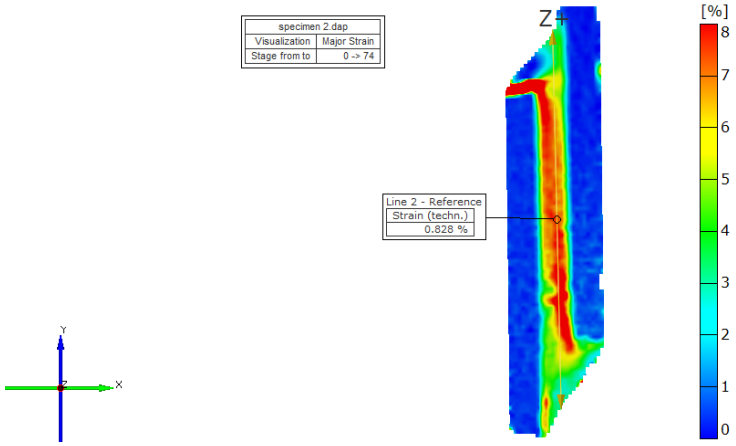


Figure 3.12 DIC Strain distribution at failure for Al-Al SLJ bonded with quick set epoxy at a strain rate of 0.0015 $s^{-1}$.

Figure 3.13 shows typical stress-strain curves of the lap joint specimen when tested at a strain rate of 0.15 $s^{-1}$. The lap joint was analyzed based on the shear strength, and it can be seen from the graph that the lap joint exhibited an average shear strength of 5.99 MPa and a peak strain of 0.66 %.

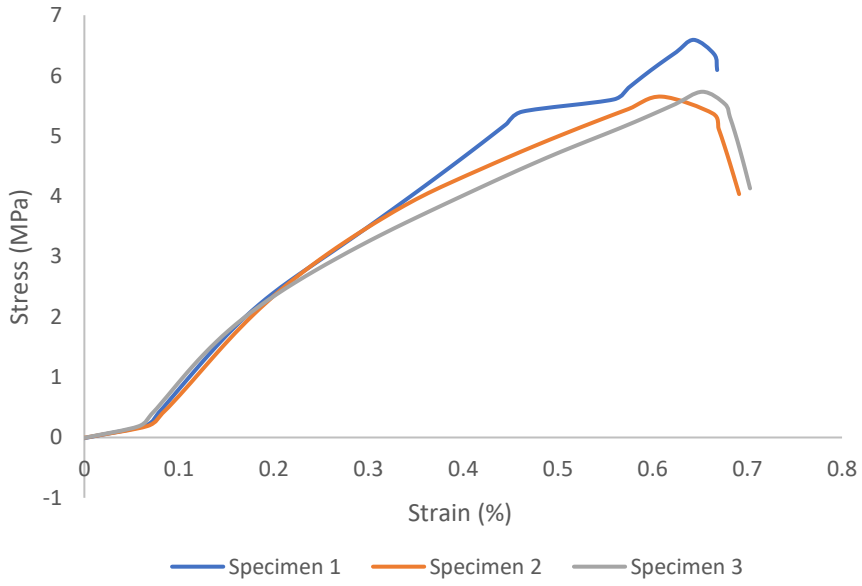


Figure 3.13 Typical stress-strain curve of Al-Al joint bonded with quick set epoxy tested under tensile loading conditions at a strain rate of 0.15 $s^{-1}$.

Figure 3.14 shows low magnification optical microscopy image after break for Al-Al SLJ bonded with quick set epoxy when tested under tensile loading conditions at a strain rate of 0.15 $s^{-1}$. From the image, it can be clearly observed that the failure mode is interface failure between adhesive and adherend due to peeling (AF-P) on both of the adherends.

Figure 3.14 Low magnification image after fracture of Al-Al bonded with quick set epoxy under tensile loading conditions at a strain rate of 0.15 $s^{-1}$

Figure 3.15 shows the DIC strain distribution map near to failure for Al-Al SLJ bonded with quick set epoxy subjected to a strain rate of 0.15 $s^{-1}$. It can be seen that the peak strain is localized in the top and bottom region of adhesive and adherend due to peeling and propagated to the middle section until failure. This can be verified with the low magnification were adhesive failure mode can be observed on both the adherends.

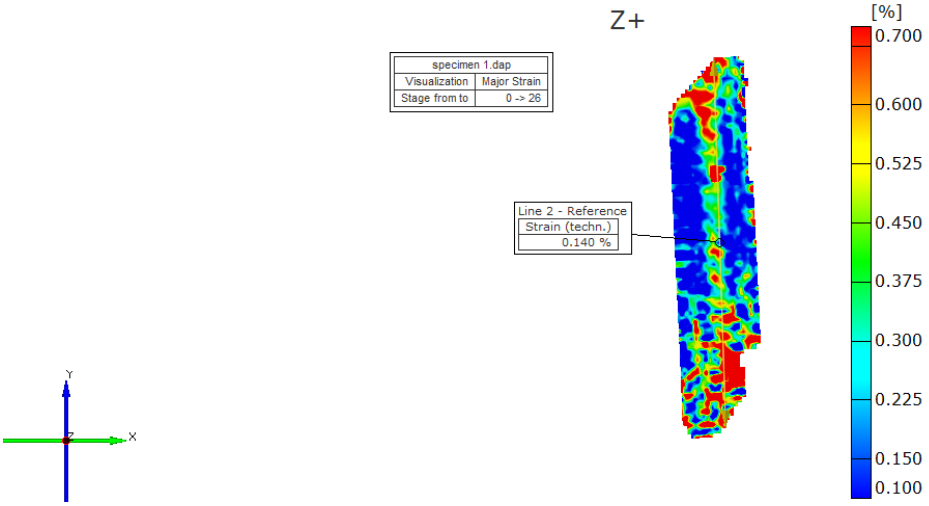


Figure 3.15 DIC Strain distribution at failure for Al-Al SLJ bonded with quick set epoxy tested under tensile loading conditions at a strain rate of 0.15 $s^{-1}$.

### 3.1.1.3 Al 6061-Al 6061 with urethane-based adhesive

Figure 3.16 shows a typical stress-strain curves of al-al SLJ bonded with urethane-based tested under tensile loading conditions at a strain rate of 0.0015 s-1. The lap joint was analyzed based on the lap shear strength and it can be seen from the graph that the lap joint exhibited an average shear strength of 3.01 MPa and a peak strain of 2.8 %.

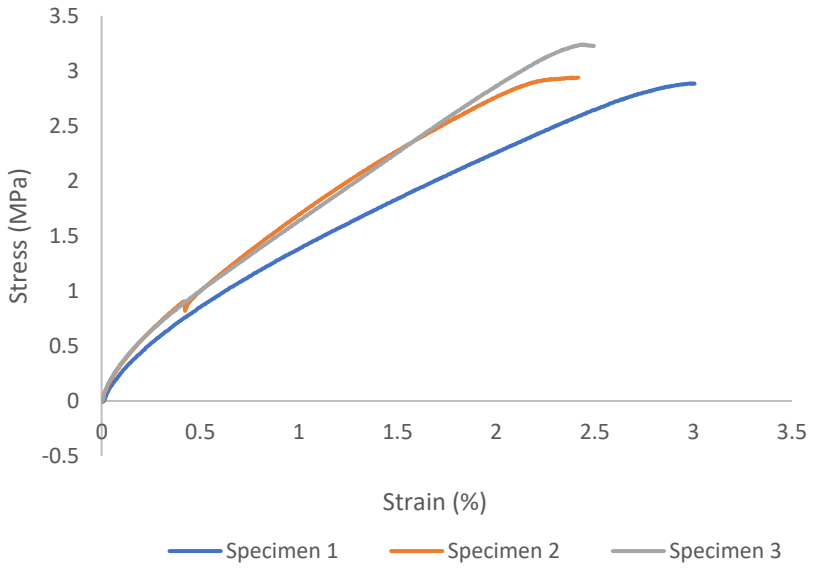


Figure 3.16 Typical stress-strain curve of al-al SLJ bonded with urethane-based tested under tensile loading conditions at a strain rate of 0.0015 $s^{-1}$

Figure 3.17 shows a low magnification optical microscopy image after break for Al-Al SLJ bonded with urethane-based adhesive when tested under tensile loading conditions at a strain rate of 0.0015 $s^{-1}$. Here, it can be seen that there is a mixed mode failure with some amount of cohesive failure in adhesive due to shear while the rest is interface failure between adhesive and adherend due to shear.

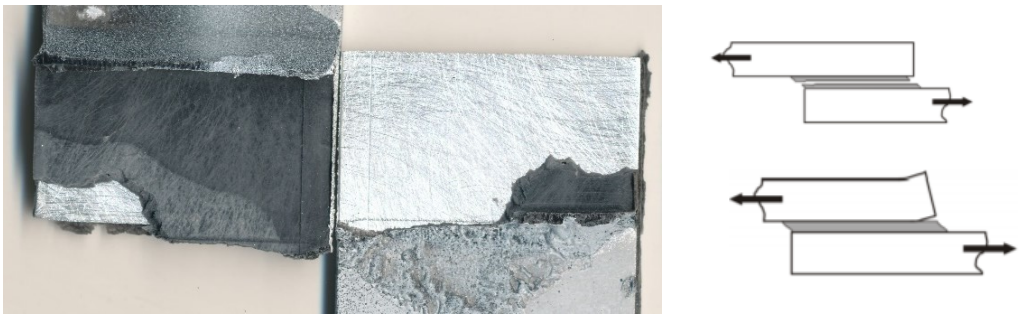

Figure 3.17 Low magnification image after fracture of Al-Al SLJ bonded with urethane-based adhesive tested under tensile loading conditions at a strain rate of 0.0015 $s^{-1}$.

Figure 3.18 shows an optical microscopy image captured at 10 × magnification of Al-Al SLJ bonded with urethane-based adhesive tested under tensile loading conditions at a strain rate of 0.0015 $s^{-1}$. The figure depicts the bond area of the aluminum adhered with the adhesive to understand the behavior of urethane-based adhesion. In this case, we can clearly observe the shearing between the adhesive and the impressions of rough surface from the aluminum adherend on the adhesive tells us that the surface treatment used is working well on this adhesive as well.

Figure 3.18 Optical microscopy image 10 × magnification of Al-Al SLJ bonded with urethane-based adhesive tested at a strain rate of 0.0015 $s^{-1}$.

Figure 3.19 shows a DIC strain distribution map near to failure for Al-Al SLJ bonded with urethane-based adhesive subjected to a strain rate of 0.0015 $s^{-1}$. It can be seen that the peak strain

was first localized in the bottom region of adhesive and adherend but simultaneously a shear strain is also observed to propagate from middle section to the top section until failure.

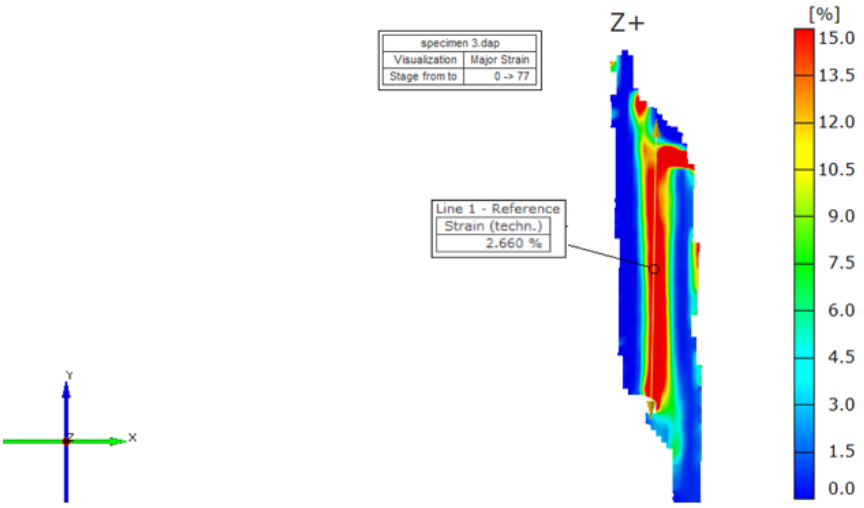


Figure 3.19 DIC Strain distribution at failure for Al-Al SLJ bonded with urethane-based adhesive at a strain rate of 0.0015 $s^{-1}$.

Figure 3.20 shows a typical stress-strain curves of the single lap joint specimen when tested at a strain rate of 0.15 $s^{-1}$. The lap joint was analyzed based on the lap shear strength and it can be seen from the graph that the lap joint exhibited an average shear strength of 11.34 MPa and a peak strain of 3.32 %.

Figure 3.21 shows a low magnification optical microscopy image after break for Al-Al SLJ bonded with urethane-based adhesive tested under tensile loading conditions at a strain rate of 0.15 $s^{-1}$. Here, it can be seen that there is a mixed mode failure with huge amount of cohesive failure in adhesive due to shear some amount of interface failure between adhesive and adherend due to shear.

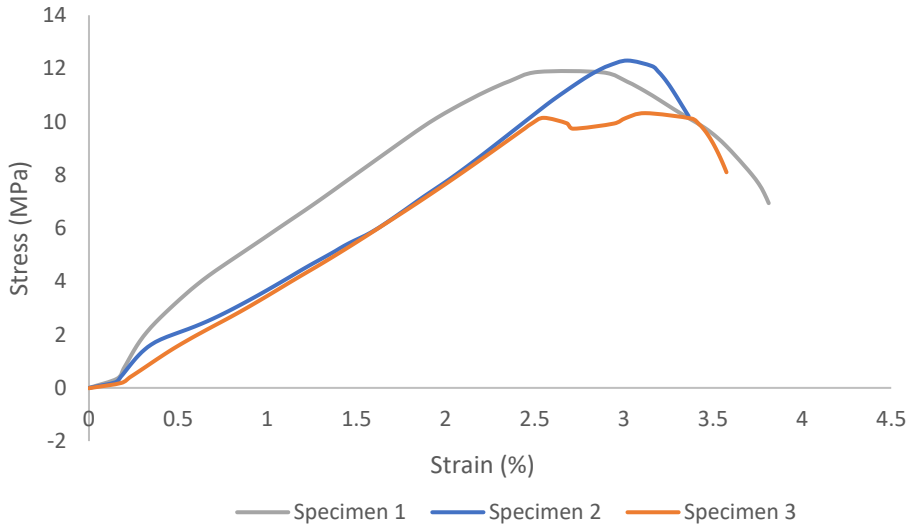


Figure 3.20 Typical stress-strain curve of Al-Al SLJ bonded with urethane-based adhesive tested under tensile loading conditions at a strain rate of 0.15 $s^{-1}$

Figure 3.21 Low magnification image after fracture of Al-Al bonded with urethane-based adhesive under tensile loading conditions at a strain rate of 0.15 $s^{-1}$

Figure 3.22 shows a DIC strain distribution map near to failure for Al-Al SLJ bonded with urethane-based adhesive subjected to a strain rate of 0.15 $s^{-1}$. It can be seen that the peak strain is throughout the adhesive bondline propagating resulting in a cohesive failure in adhesive due to shear.

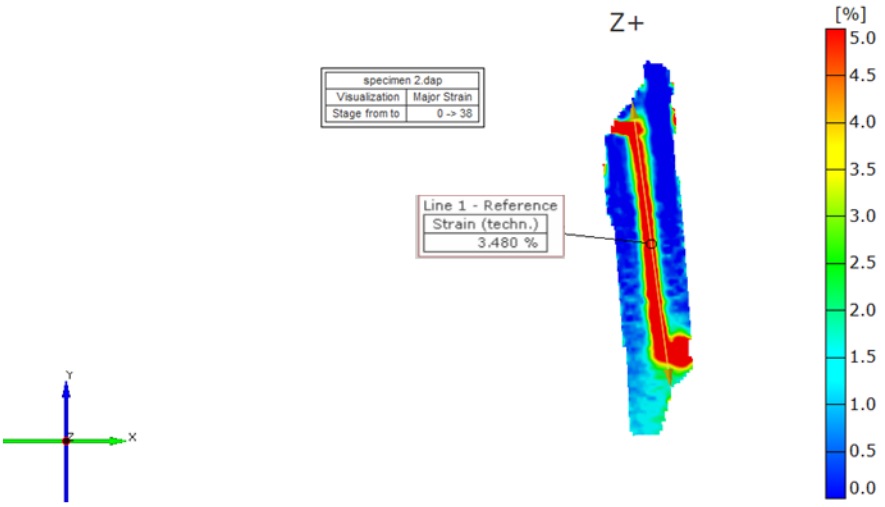


Figure 3.22 DIC Strain distribution at failure for Al-Al SLJ bonded with urethane-based adhesive at a strain rate of 0.15 $s^{-1}$.

### 3.1.2 Aluminum – CFRP joints

In these joints, the Aluminum alloy was bonded with carbon fiber reinforced polymer with the three adhesives chosen. Different adherends were used for understanding the behavior of similar and dissimilar single-lap joints.

#### 3.1.2.1 Al6061-CFRP with high strength epoxy

Figure 3.23 shows a typical stress-strain curves of the lap joint specimen when tested at a strain rate of 0.0015 $s^{-1}$. The lap joint was analyzed based on the lap shear strength, and it can be seen from the graph that the lap joint exhibited an average shear strength of 4.94 MPa and a peak strain of 0.264 %.

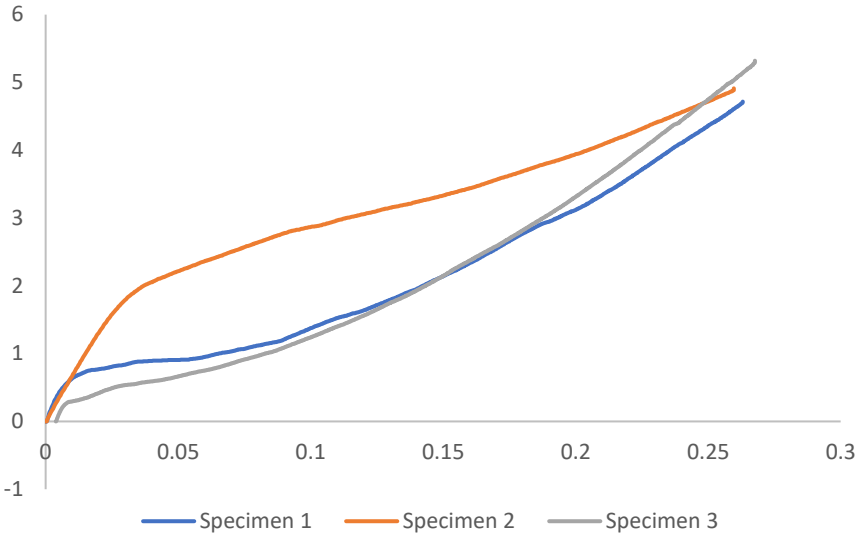


Figure 3.23 Typical stress-strain curve of Al-CFRP SLJ bonded with high strength epoxy tested under tensile loading conditions at a strain rate of 0.0015 $s^{-1}$.

Figure 3.24 shows a low magnification optical microscopy image after the break for Al-CFRP SLJ bonded with high strength epoxy adhesive when tested under tensile loading conditions at a strain rate of 0.0015 $s^{-1}$. Here, it appears to be a mixed mode failure with a large amount of interface failure between adhesive and adherend due to peel and a small amount of cohesive failure in adhesive due to shear. This could have due to the uncured epoxy in the near-end of the bond. If the adhesion between aluminum adherend and epoxy was better a large amount of cohesive failure in the adhesive could have been observed.

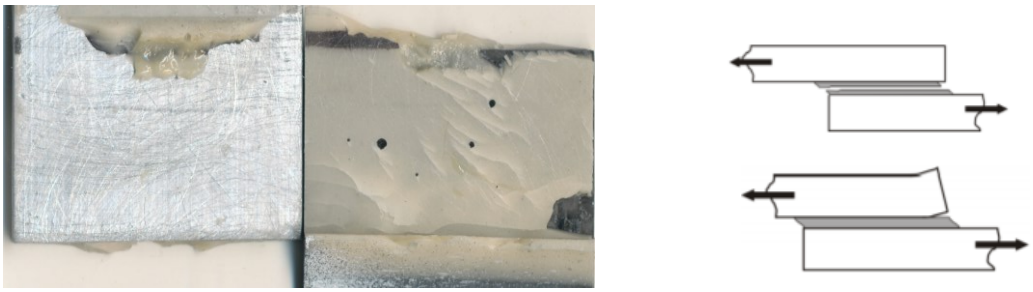

Figure 3.24 Low magnification image after fracture of Al-CFRP SLJ bonded with high strength epoxy at a strain rate of 0.0015 $s^{-1}$

Figure 3.25 shows an optical microscopy image captured at 10 × magnification of Al-CFRP SLJ bonded with high strength epoxy tested under tensile loading conditions at a strain rate of 0.0015 $s^{-1}$. The figure depicts the bond area of the composite adherend with the adhesive to understand the behavior of high strength epoxy adhesion. In this case, we can observe the brittle fracture of adhesive and the impressions of rough surface from the aluminum adherend on the adhesive are not as evidently visible like in other adhesives.

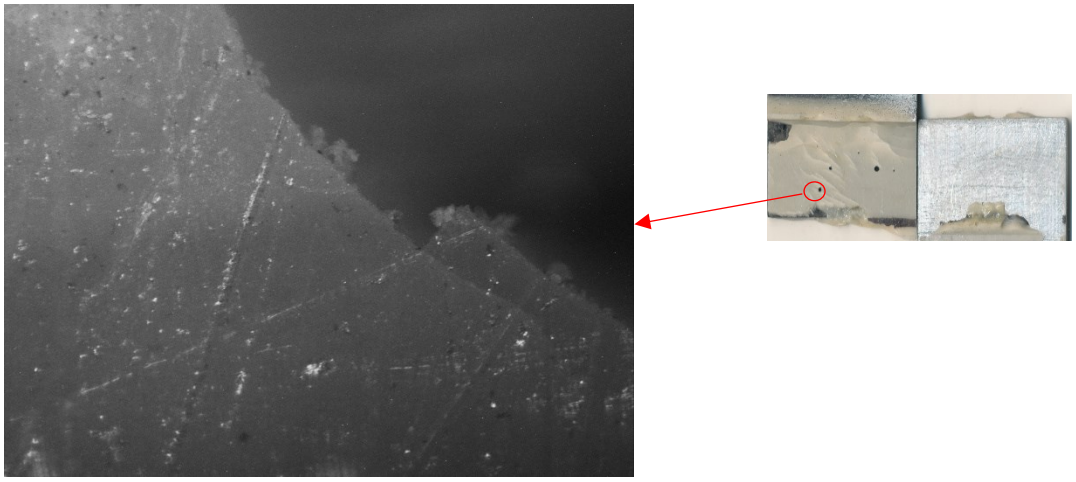

Figure 3.25 Optical microscopy image captured at 10 × magnification of Al-CFRP SLJ bonded with high strength epoxy tested under tensile loading at a strain rate of 0.0015 $s^{-1}$.

Figure 3.26 shows a DIC strain distribution map near to failure for Al-CFRP SLJ bonded with high strength epoxy subjected to a strain rate of 0.0015 $s^{-1}$. From the figure, we can see that the peak strain is in the bottom region due to peeling which resulted in the cohesive failure in the adhesive as seen in low magnification image. Moreover, there is strain accumulated in the CFRP adherend.

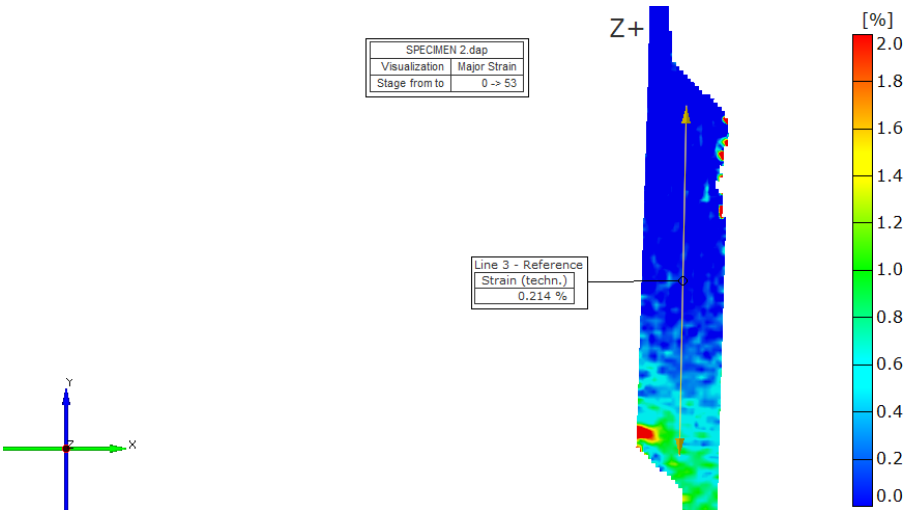


Figure 3.26 DIC Strain distribution at failure for Al-CFRP SLJ bonded with high strength epoxy at a strain rate of 0.0015 $s^{-1}$.

Figure 3.27 shows a typical stress-strain curves of the lap joint specimen when tested at a strain rate of 0.15 $s^{-1}$. The lap joint was analyzed based on the lap shear strength and peak strain, and it can be observed that the lap joint exhibited an average shear strength of 5.79 MPa and a peak strain of 0.154 %.

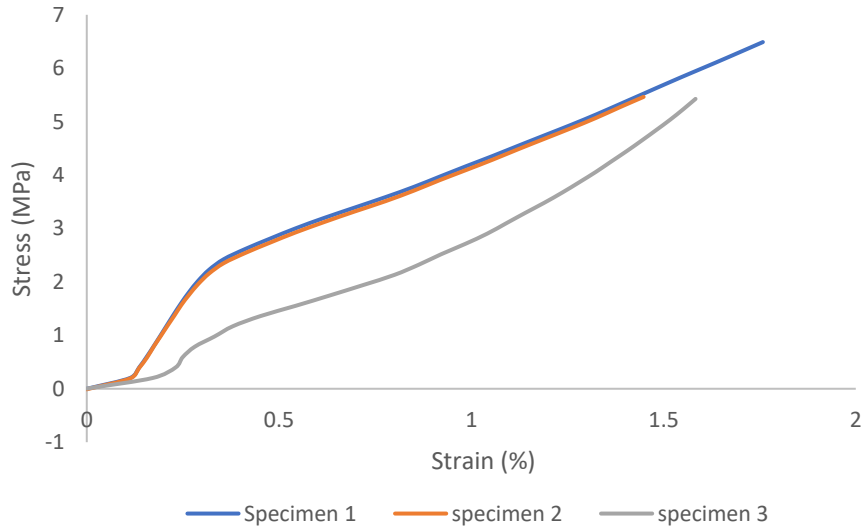


Figure 3.27 Typical stress-strain curve of Al-CFRP SLJ bonded with high strength epoxy tested under tensile loading conditions at a strain rate of 0.15 $s^{-1}$

Figure 3.28 shows a low magnification optical microscopy image after the break for Al-CFRP SLJ bonded with high strength epoxy when tested under tensile loading conditions at a strain rate of 0.15 $s^{-1}$. Here, it appears to be a mixed mode failure with an equal amount of interface failure between adhesive and CFRP adherend and composite adherend interlaminar failure.

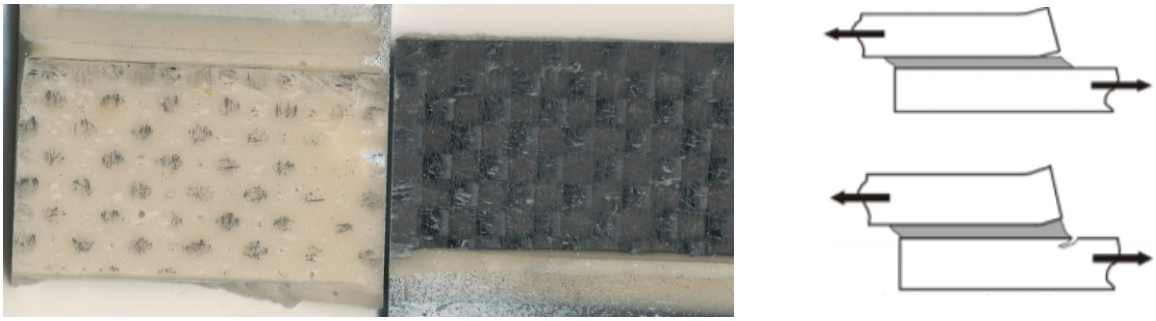

Figure 3.28 Low magnification image after fracture of Al-CFRP SLJ bonded with high strength epoxy at a strain rate of 0.15 $s^{-1}$

Figure 3.29 shows a DIC strain distribution map near to failure for Al-CFRP SLJ bonded with high strength epoxy subjected to a strain rate of 0.15 $s^{-1}$. From the figure, the peak strain before failure is 0.175 % for this specimen, and the shear strain is spread throughout the adhesive bondline and CFRP adherend.

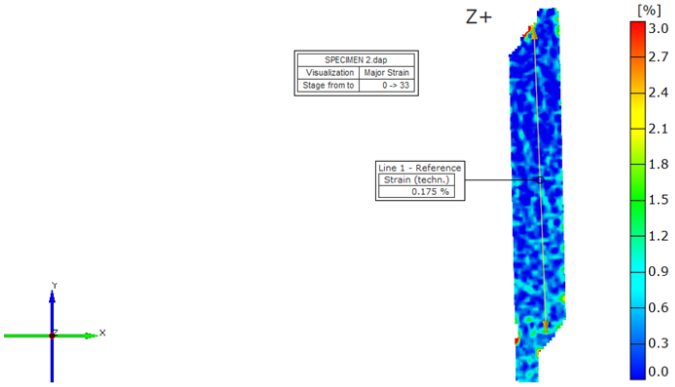


Figure 3.29 DIC Strain distribution at failure for Al-CFRP SLJ bonded with high strength epoxy tested under tensile loading conditions at a strain rate of 0.15 $s^{-1}$.

### 3.1.2.2 Al6061-CFRP with quick set epoxy

Figure 3.30 shows typical stress-strain curves of Al-CFRP SLJ bonded with quick set epoxy tested under tensile loading conditions at a strain rate of 0.0015 $s^{-1.}$ The lap joint was analyzed based on the lap shear strength and peak strain, and it can be observed that the lap joint exhibited an average shear strength of 4.28 MPa and a peak strain of 0.508 %. Moreover, when bonded with quick set epoxy exhibits a non-linear behavior in the initial part of the curve. This is believed to be as a result of tensile behavior in the metallic layer.

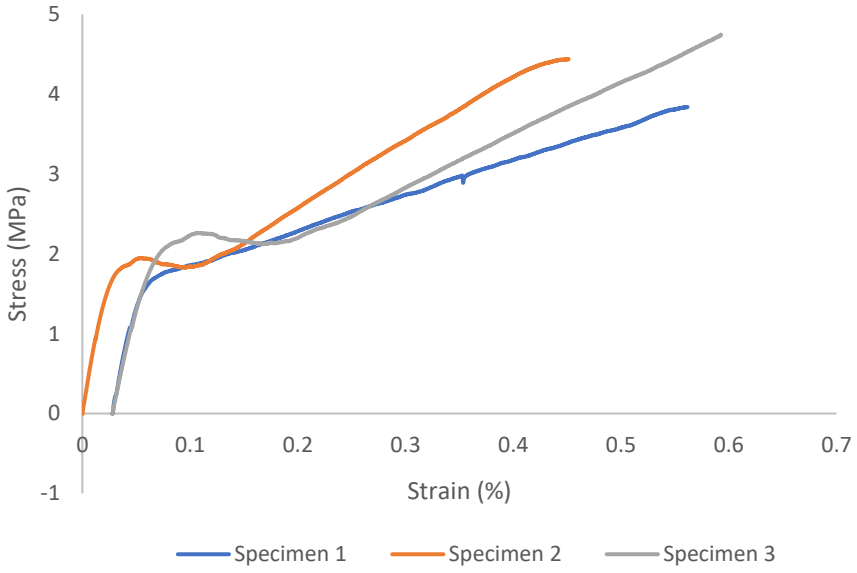


Figure 3.30 Typical stress-strain curve of Al-CFRP SLJ bonded with quick set epoxy tested under tensile loading conditions at a strain rate of 0.0015 $s^{-1}$.

Figure 3.31 shows a low magnification optical microscopy image after the break for Al-CFRP SLJ bonded with quick set epoxy when tested under tensile loading conditions at a strain rate of 0.0015 $s^{-1}$. Here, it appears to be complete interface failure between the aluminum alloy adherend and epoxy with no residue left on the aluminum adherend.

Figure 3.31 Low magnification image after fracture of Al-CFRP bonded with quick set epoxy tested under tensile loading conditions at a strain rate of 0.0015 $s^{-1}$.

Figure 3.32 shows an optical microscopy image captured at 10 × magnification of Al-CFRP SLJ bonded with quick set epoxy tested under tensile loading conditions at a strain rate of 0.0015 $s^{-1}$. The figure depicts the bond area of the aluminum adhered without adhesive to understand the behavior of substrate after break. In this case, there is some amount of adhesive residue left on the aluminum adherend after an interfacial failure between aluminum substrate and adhesive.

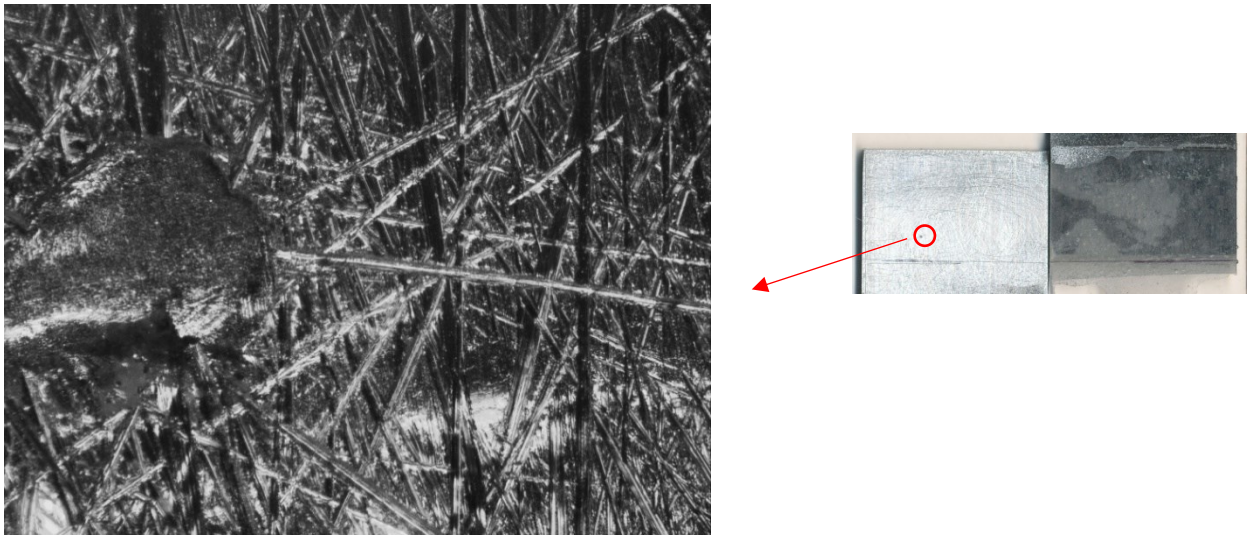

Figure 3.32 Optical microscopy image at 10 × magnification of Al-CFRP SLJ bonded with quick set epoxy tested at a strain rate of 0.0015 $s^{-1}$.

Figure 3.33 shows a DIC strain distribution map near to failure for Al-CFRP SLJ bonded with quick set epoxy subjected to a strain rate of 0.0015 $s^{-1}$. From the figure, the peak strain before failure is 0.598 % for this specimen, and higher values of longitudinal and shear strain to failure is

observed. The maximum strain values are more pronounced near to the top adherend which resulted in the cohesive failure in the CFRP adherend as discussed in theprevious section.

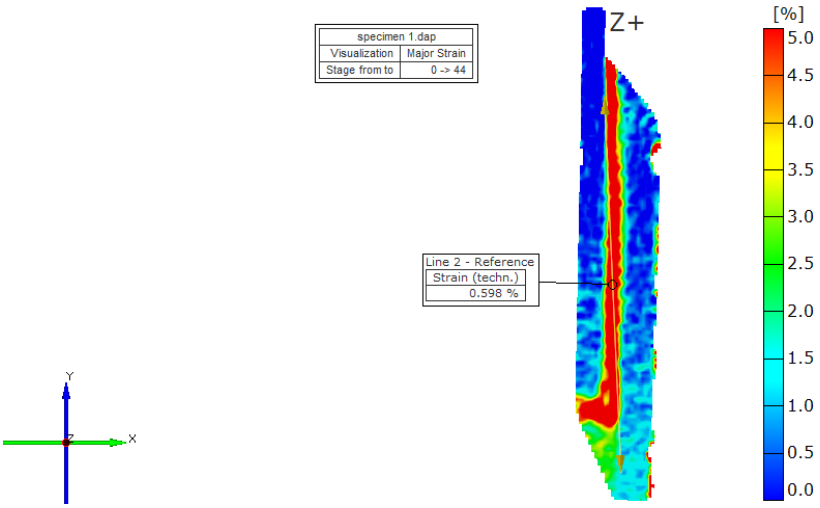


Figure 3.33 DIC Strain distribution at failure for Al-CFRP SLJ bonded with quick set epoxy at a strain rate of 0.0015 $s^{-1}$.

Figure 3.34 shows a typical stress-strain curves of Al-CFRP SLJ bonded with quick set epoxy tested under tensile loading conditions at a strain rate of 0.15 s-1. The lap joint was analyzed based on the lap shear strength and peak strain, and it can be observed that the lap joint exhibited an average shear strength of 7.67 MPa and a peak strain of 0.493 %.

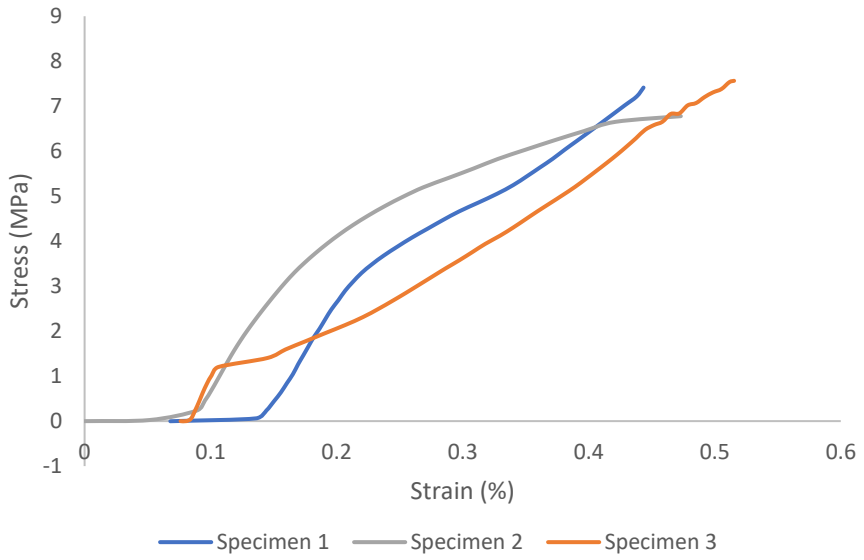


Figure 3.34 Typical stress-strain curve of Al-CFRP SLJ bonded with quick set epoxy tested under tensile loading conditions at a strain rate of 0.15 $s^{-1}$.

Figure 3.35 shows a low magnification optical microscopy image after the break for Al-CFRP SLJ bonded with quick set epoxy when tested under tensile loading conditions at a strain rate of 0.15 $s^{-1}$. Here, it appears to be mixed mode failure with interface failure between the both the adherends and adhesive, and cohesive failure in the CFRP adherend.

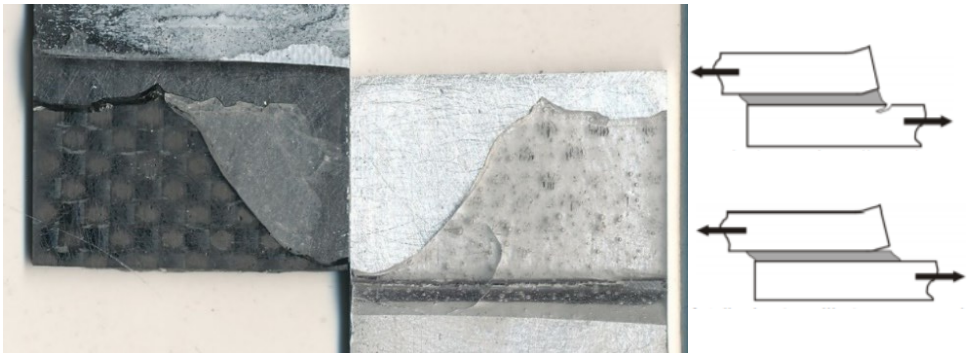

Figure 3.35 Low magnification image after fracture of Al-CFRP bonded with quick set epoxy at a strain rate of 0.15 $s^{-1}$.

Figure 3.36 shows a DIC strain distribution map near to failure for Al-CFRP SLJ bonded with quick set epoxy subjected to a strain rate of 0.0015 $s^{-1}$. From the figure, the peak strain before failure is 0.493 % for this specimen. The peak strain is creeping towards the middle section from

the top section until failure. Moreover, it is also evident that such strain distribution is less pronounced across the bond region as the strain rate was increased, highlighting the effect of strain rate on the mechanical behavior of the SLJ system.

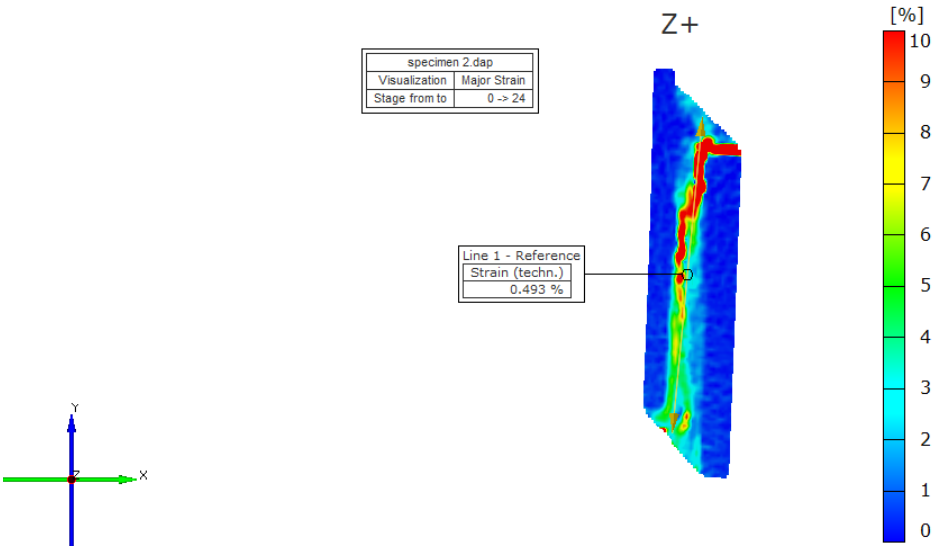


Figure 3.36 DIC Strain distribution at failure for Al-CFRP SLJ bonded with quick set epoxy tested under tensile loading conditions at a strain rate of 0.15 $s^{-1}$.

### 3.1.2.3 Al6061-CFRP with urethane-based adhesive

Figure 3.37 shows typical stress-strain curves of Al-CFRP SLJ bonded with urethane-based adhesive tested under tensile loading conditions at a strain rate of 0.0015 $s^{-1}$. The lap joint was analyzed based on the lap shear strength and peak strain, and it can be observed that the lap joint exhibited an average shear strength of 6.77 MPa and an average peak strain of 1.3 %.

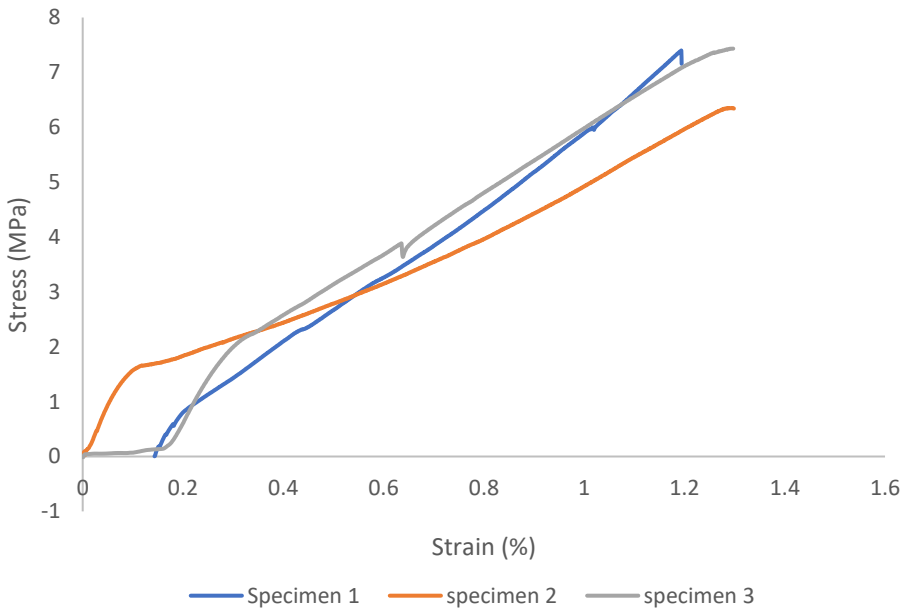


Figure 3.37 Typical stress-strain curve of Al-CFRP SLJ bonded with urethane-based adhesive tested under tensile loading conditions at a strain rate of 0.0015 $s^{-1}$.

Figure 3.38 shows a low magnification optical microscopy image after the break for Al-CFRP SLJ bonded with urethane-based adhesive when tested under tensile loading conditions at a strain rate of 0.0015 $s^{-1}$. Here, it is evident that the failure mode is interface failure between aluminum alloy and adhesive due to shear.

Figure 3.38 Low magnification image after fracture of Al-CFRP bonded with urethane-based adhesive at a strain rate of 0.0015 $s^{-1}$

Figure 3.39 shows an optical microscopy image captured at 10 × magnification of Al-CFRP SLJ bonded with urethane-based adhesive tested under tensile loading conditions at a strain rate of 0.0015 $s^{-1}$. The figure depicts the bond area of the CFRP adherend with adhesive to understand the behavior of adhesive after break. Here, few shine spots on the bond are visible which might be from the oxide layer formed on aluminum during adhesion.

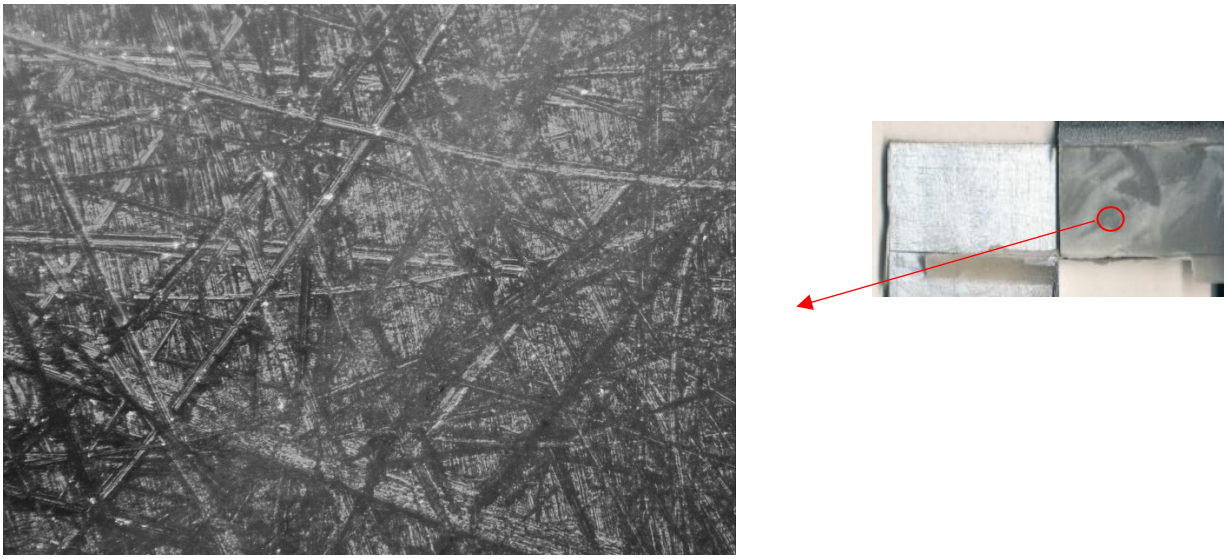

Figure 3.39 Optical microscopy image captured at 10 × magnification of Al-CFRP SLJ bonded with urethane-based adhesive tested conditions at a strain rate of 0.0015 $s^{-1}$.

Figure 3.40 shows a DIC strain distribution map near to failure for Al-CFRP SLJ bonded with urethane-based adhesive subjected to a strain rate of 0.0015 $s^{-1}$. From the figure, the peak strain before failure is 1.314 % for this specimen. It can be observed that a shear strain is present in the adhesive bondline region.

Figure 3.41 shows typical stress-strain curves of Al-CFRP SLJ bonded with urethane-based adhesive tested under tensile loading conditions at a strain rate of 0.15 s-1. The lap joint was analyzed based on the lap shear strength and peak strain, and it can be observed that the lap joint exhibited an average shear strength of 12.99 MPa and a peak strain of 1.20 %.

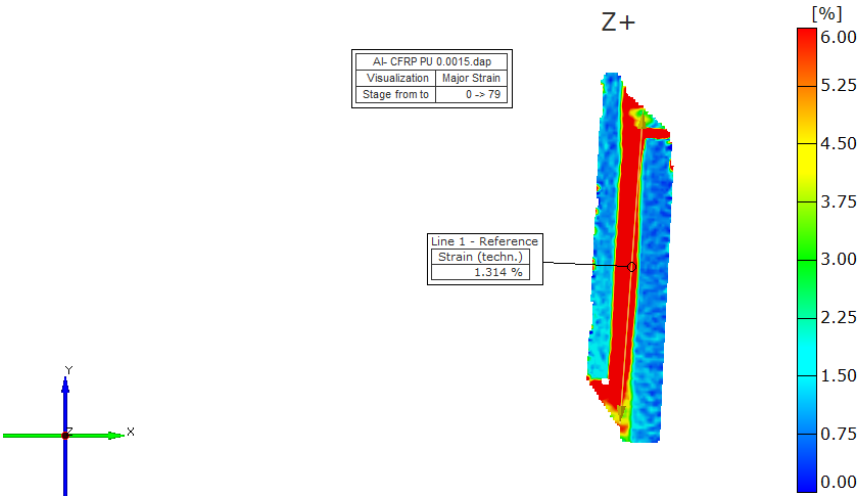


Figure 3.40 DIC Strain distribution at failure for Al-CFRP SLJ bonded with urethane-based adhesive tested under tensile loading conditions at a strain rate of 0.0015 $s^{-1}$.

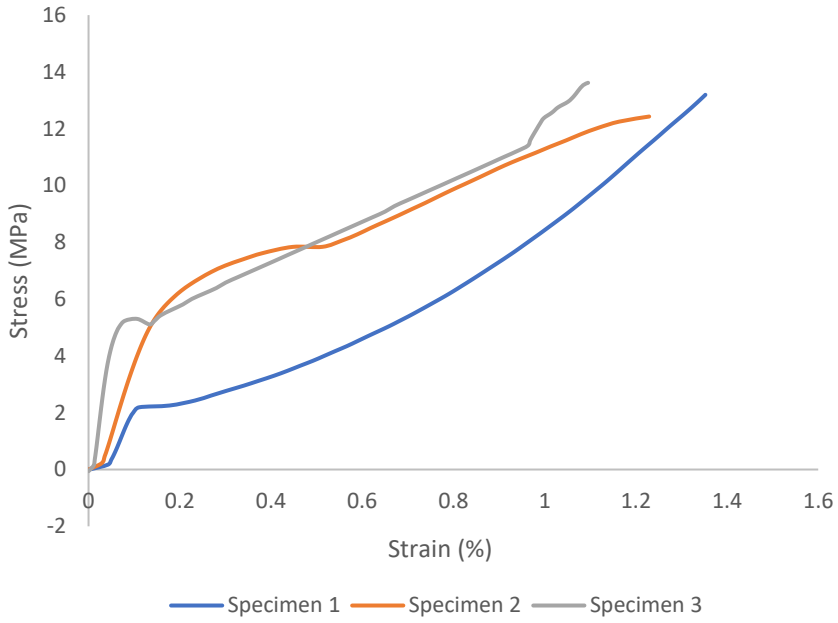


Figure 3.41 Typical stress-strain curve of Al-CFRP SLJ bonded with urethane-based adhesive tested at a strain rate of 0.15 $s^{-1}$

Figure 3.42 shows a low magnification optical microscopy image after the break for Al-CFRP SLJ bonded with urethane-based adhesive when tested under tensile loading conditions at a strain rate

of 0.0015 $s^{-1}$. Here, it is visible that there is cohesive failure in the adhesive due to shear and the ductile behavior of the adhesive can be observed.


Figure 3.42 Low magnification image for Al-CFRP SLJ bonded with urethane-based adhesive under tensile loading conditions subjected to a strain rate of 0.15 $s^{-1}$.

Figure 3.43 shows a DIC strain distribution map near to failure for Al-CFRP SLJ bonded with urethane-based adhesive subjected to a strain rate of 0.0015 $s^{-1}$. From the figure, there is an evident spread of shear strain along the adhesive bondline propagating from the middle section towards the Peel region.

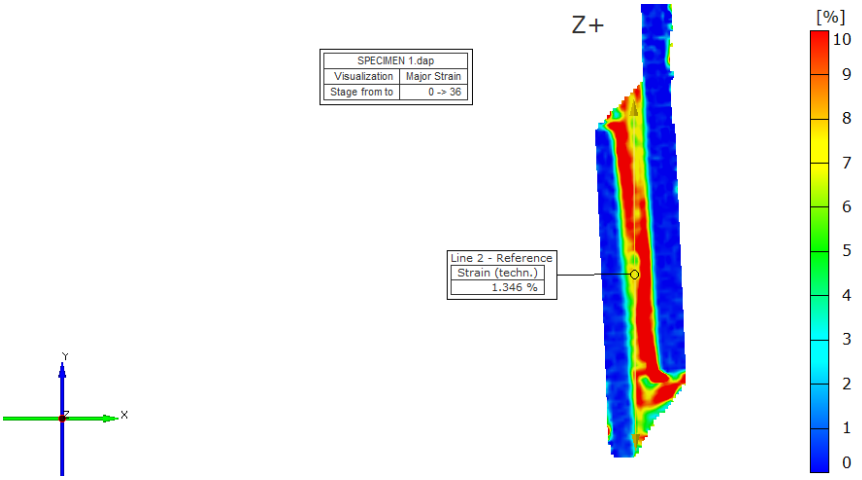


Figure 3.43 DIC strain distribution at failure for Al-CFRP SLJ bonded with urethane-based adhesive subjected to a strain rate of 0.15 $s^{-1}$.

### 3.1.3 Composite Joints

Experimental analysis was performed adhesively bonded single lap joints with carbon fiber reinforced polymer as adherends with three different adhesives. The carbon fiber was obtained with a thickness of 1.58 mm, and the adhesive thickness was maintained at 1 mm. These joints exhibited high load bearing capacity than the other combinations, but lesser shear strain compared to Aluminum joints when tested under tensile loading conditions at strain rates of 0.0015 $s^{-1}$ and 0.15 $s^{-1.}$ Optical microscopy and DIC distributions were used to determine the failure mode occurring in the joints.

#### 3.1.3.1 CFRP-CFRP with high strength epoxy

Figure 3.44 shows typical stress-strain curves of CFRP-CFRP SLJ bonded with high strength epoxy tested under tensile loading conditions at a strain rate of 0.0015 $s^{-1}$. The lap joint was analyzed based on the lap shear strength and peak strain, and it can be observed that the lap joint exhibited an average shear strength of 11.78 MPa and a peak strain of 0.35 %.

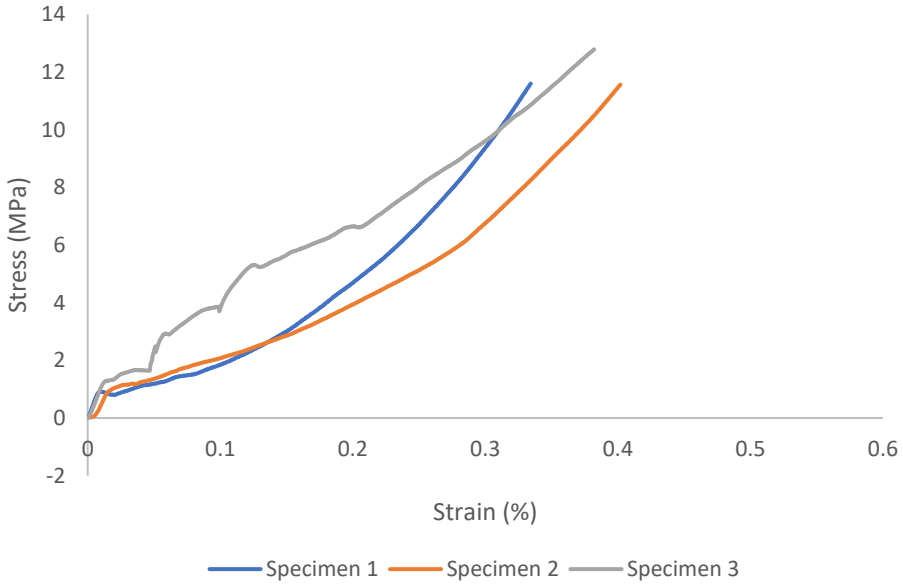


Figure 3.44 Typical stress-strain curve of CFRP-CFRP SLJ bonded with high strength epoxy tested under tensile loading conditions at a strain rate of 0.0015 $s^{-1}$.

Figure 3.45 shows a low magnification optical microscopy image after the break for CFRP-CFRP SLJ bonded with high strength epoxy when tested under tensile loading conditions at a strain rate of 0.0015 $s^{-1}$. From the figure, it can be observed that there is an interlaminar failure in carbon fiber adherend due to shear and some amount of interface failure between adhesive and CFRP adherend.

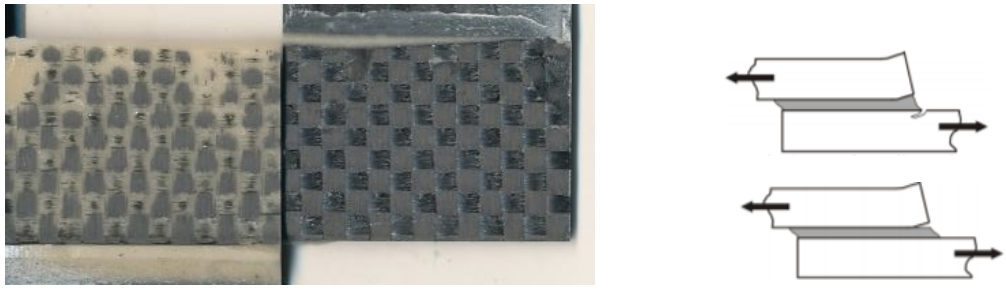

Figure 3.45 Low magnification image after failure for CFRP-CFRP SLJ bonded with high strength epoxy subjected to a strain rate of 0.0015 $s^{-1}$.

Figure 3.46 shows an optical microscopy image captured at 10 × magnification of CFRP-CFRP SLJ bonded with high strength epoxy tested under tensile loading conditions at a strain rate of 0.0015 $s^{-1}$.

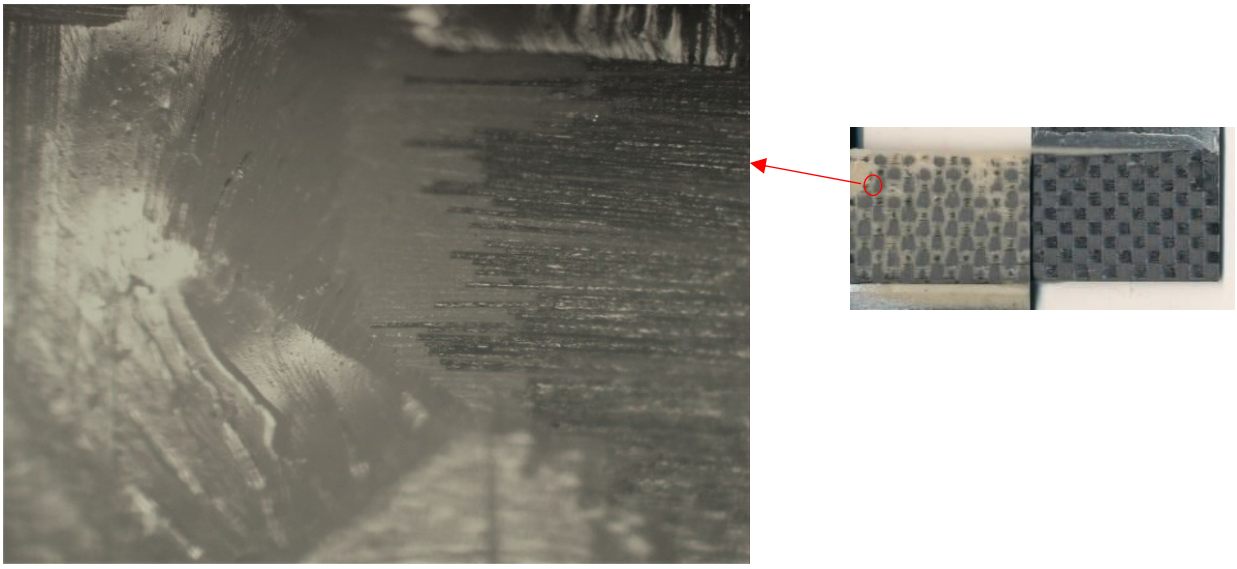

Figure 3.46 Optical microscopy image 10 × magnification of CFRP-CFRP SLJ bonded with high strength epoxy tested at a strain rate of 0.0015 $s^{-1}$.

The figure depicts the bond area of the CFRP adherend with adhesive to understand the behavior of composite adherend fracture pattern. Here, an interlaminar failure in the CFRP layer can be observed which caused the failure. Furthermore, the brittle nature of high strength epoxy can also be noted.

Figure 3.47 shows a DIC strain distribution map near to failure for CFRP-CFRP SLJ bonded with high strength epoxy subjected to a strain rate of 0.0015 $s^{-1}$. From the figure, the peak strain for the particular specimen was 0.354 %, and the strain was propagating from the bottom region in both adherend and adhesive which resulted in the interlaminar failure in between the composite adherend.

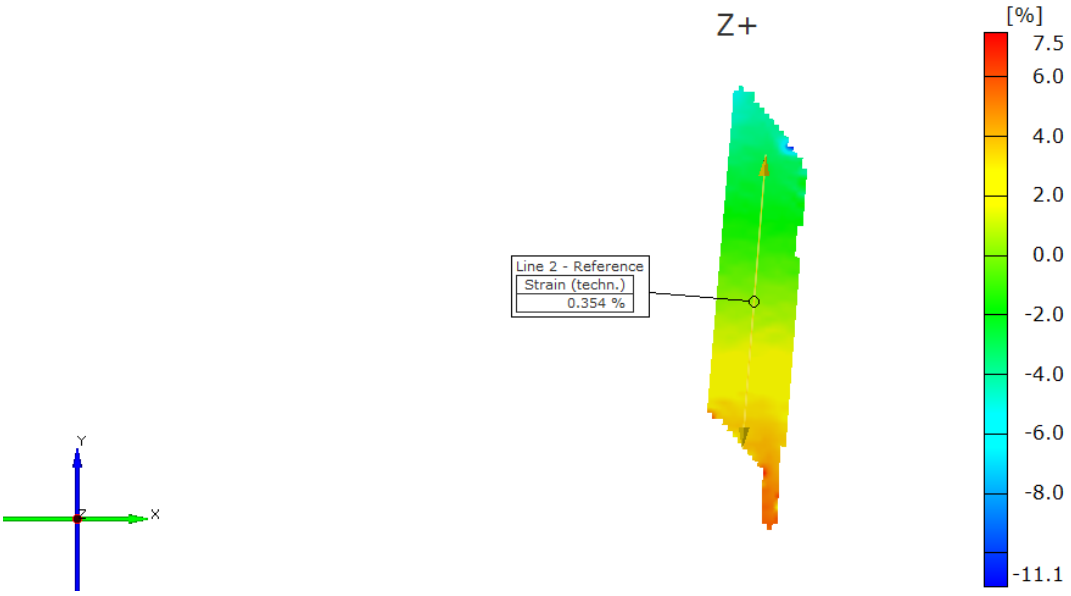


Figure 3.47 DIC strain distribution at failure for CFRP-CFRP SLJ bonded with high strength epoxy subjected to a strain rate of 0.0015 $s^{-1}$.

Figure 3.48 shows typical stress-strain curves of CFRP-CFRP SLJ bonded with high strength epoxy tested under tensile loading conditions at a strain rate of 0.15 $s^{-1}$. The lap joint was analyzed based on the lap shear strength and peak strain, and it can be observed that the lap joint exhibited an average shear strength of 12.92 MPa and a peak strain of 0.23 %.

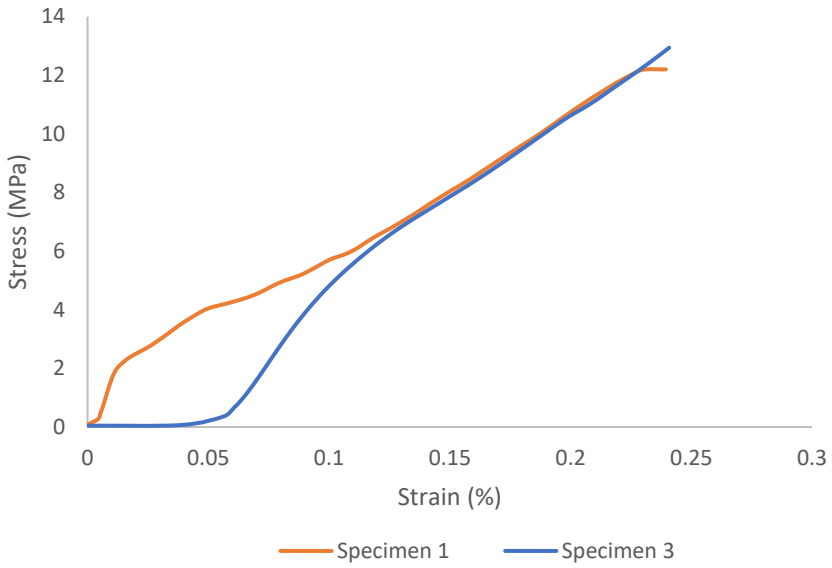


Figure 3.48 Typical stress-strain curve of CFRP-CFRP SLJ bonded with high strength epoxy tested at a strain rate of 0.15 $s^{-1}$.

Figure 3.49 shows a low magnification optical microscopy image after the break for CFRP-CFRP SLJ bonded with high strength epoxy when tested under tensile loading conditions at a strain rate of 0.15 $s^{-1}$. From the figure, it can be observed that there is a mixed mode failure with cohesive failure in CFRP adherend and some amount of cohesive failure in the adhesive.

Figure 3.49 Low magnification image after failure for CFRP-CFRP SLJ bonded with high strength epoxy subjected to a strain rate of 0.15 $s^{-1}$.

Figure 3.50 shows a DIC strain distribution map near to failure for CFRP-CFRP SLJ bonded with high strength epoxy subjected to a strain rate of 0.15 $s^{-1}$. From the figure, the peak strain for the

particular specimen was 0.216 %, the strain propagation is similar to the lower strain rate but more evident in this case.

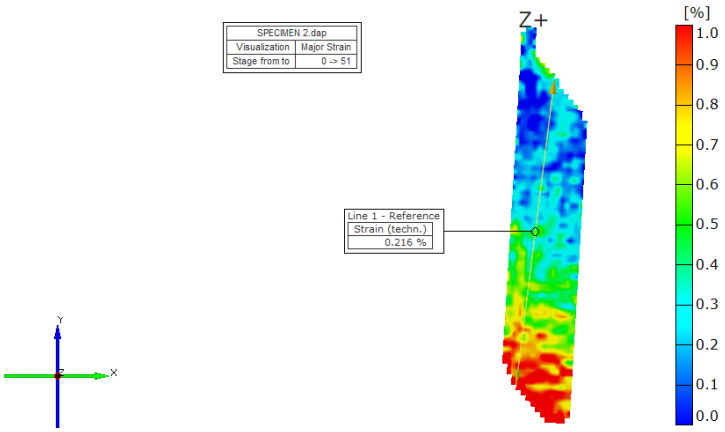


Figure 3.50 DIC strain distribution at failure for CFRP-CFRP SLJ bonded with high strength epoxy subjected to a strain rate of 0.15 $s^{-1}$.

### 3.1.3.2 CFRP-CFRP with quick set epoxy

Figure 3.51 shows typical stress-strain curves of CFRP-CFRP SLJ bonded with quick set epoxy tested under tensile loading conditions at a strain rate of 0.0015 $s^{-1}$. The lap joint was analyzed based on the lap shear strength and peak strain, and it can be observed that the lap joint exhibited an average shear strength of 9.53 MPa and an average peak strain of 1.84 %.

Figure 3.52 shows a low magnification optical microscopy image after the break for CFRP-CFRP SLJ bonded with quick set epoxy when tested under tensile loading conditions at a strain rate of 0.0015 $s^{-1}$. From the figure, it can be observed that there is a mixed mode failure, i.e. cohesive fracture in adhesive and interface fracture between adhesive and composite adherend.

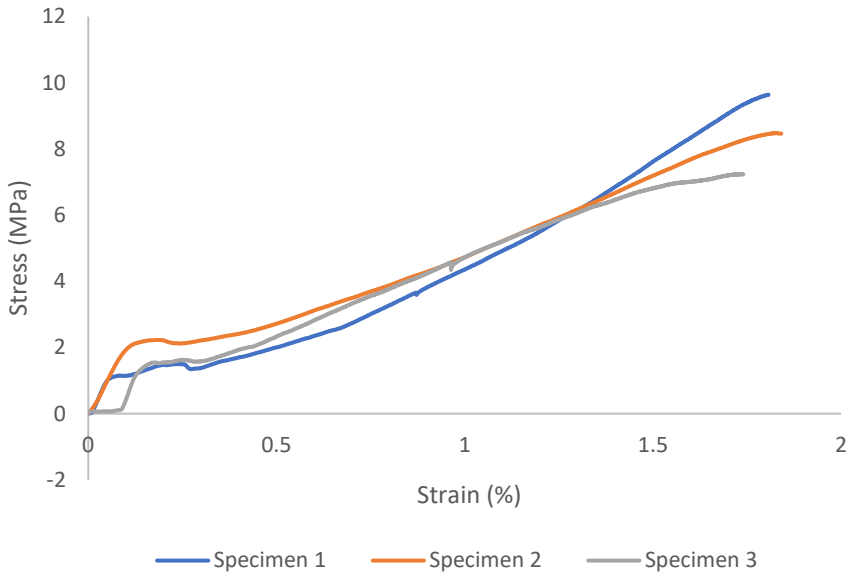


Figure 3.51 Typical stress-strain curve of CFRP-CFRP SLJ bonded with quick set epoxy tested at a strain rate of 0.0015 $s^{-1}$.

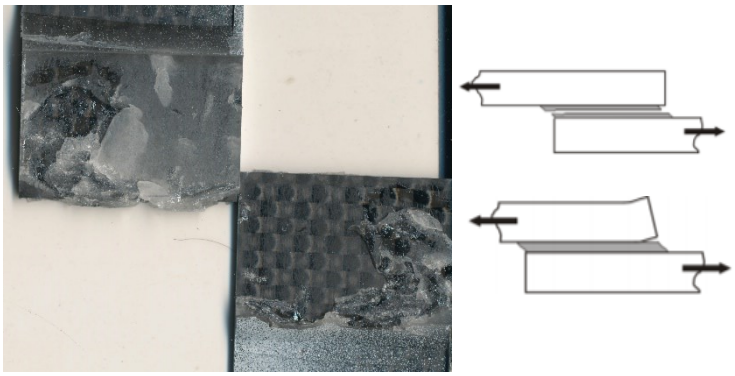

Figure 3.52 Low magnification image after failure for CFRP-CFRP SLJ bonded with quick set epoxy subjected to a strain rate of 0.0015 $s^{-1}$.

Figure 3.53 shows an optical microscopy image captured at 10 × magnification of CFRP-CFRP SLJ bonded with quick set epoxy tested under tensile loading conditions at a strain rate of 0.0015 $s^{-1}$. The behavior could be confirmed as a cohesive failure in adhesive.

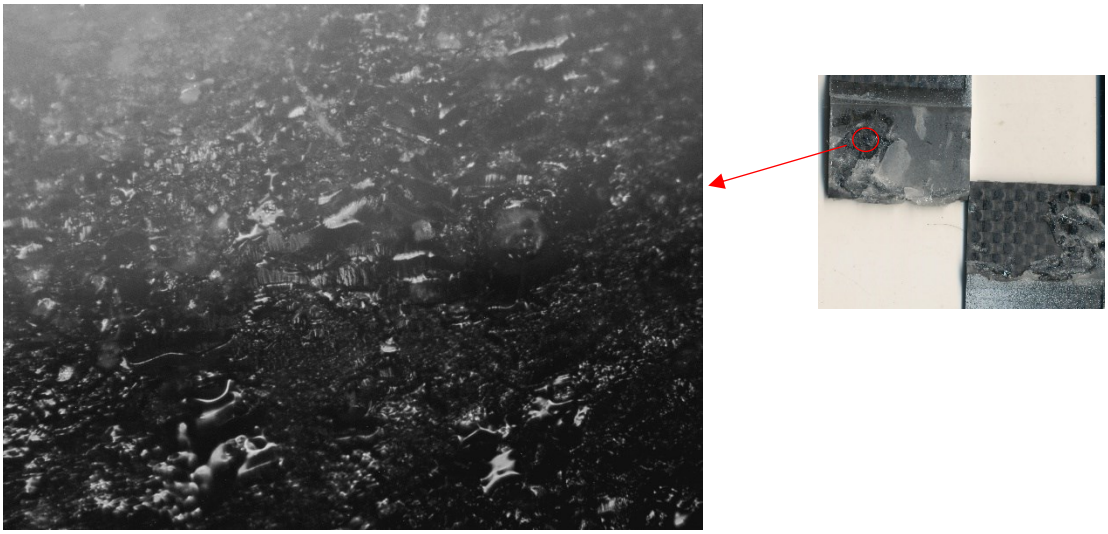

Figure 3.53 Optical microscopy image 10 × magnification of CFRP-CFRP SLJ bonded with quick set epoxy tested at a strain rate of 0.0015 $s^{-1}$.

Figure 3.54 shows a DIC strain distribution map near to failure for CFRP-CFRP SLJ bonded with quick set epoxy subjected to a strain rate of 0.0015 $s^{-1}$. From the figure, the strain near failure for the particular specimen was 1.436 %. Here, a shear strain is observed along the adhesive bondline. Furthermore, the DIC deformation analysis showed that there is a significant amount of strain propagating in the CFRP adherends as well, but it did not lead to failure.

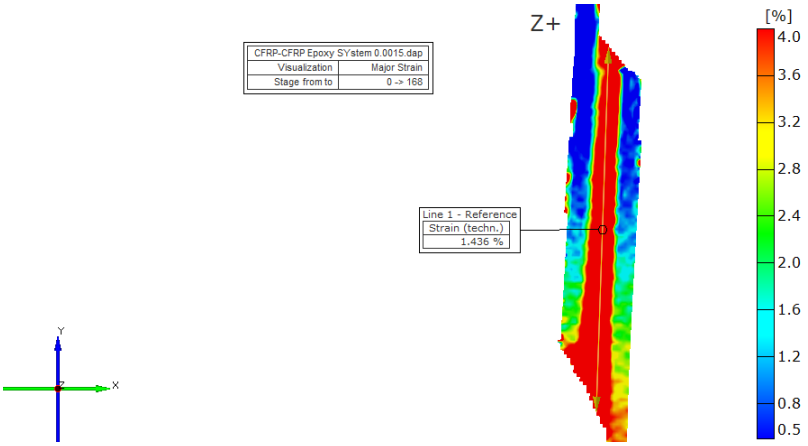


Figure 3.54 DIC strain distribution at failure for CFRP-CFRP SLJ bonded with quick set epoxy subjected to a strain rate of 0.0015 $s^{-1}$.

Figure 3.55 shows typical stress-strain curves of CFRP-CFRP SLJ bonded with quick set epoxy tested under tensile loading conditions at a strain rate of 0.15 $s^{-1}$. The lap joint was analyzed based on the lap shear strength and peak strain, and it can be observed that the lap joint exhibited an average shear strength of 13.57 MPa and a peak strain of 0.84 %.

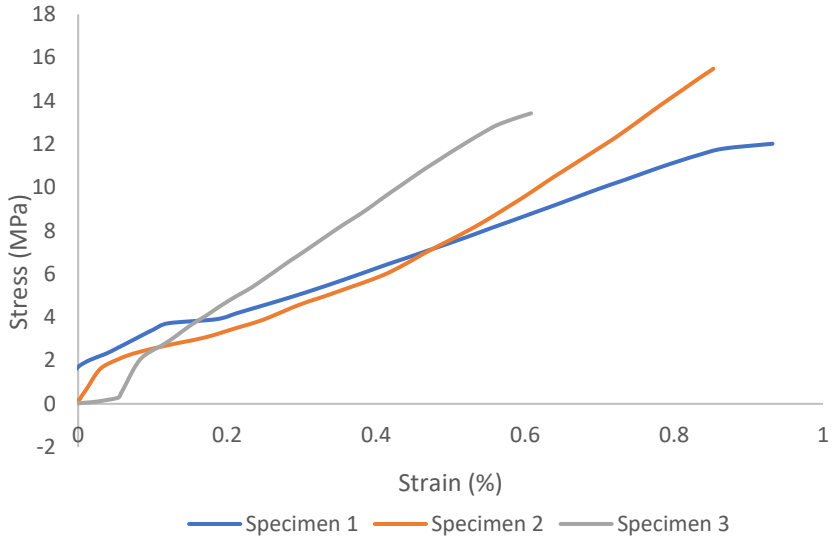


Figure 3.55 Typical stress-strain curve of CFRP-CFRP SLJ bonded with quick set epoxy tested under tensile loading conditions at a strain rate of 0.15 $s^{-1}$.

Figure 3.56 shows a low magnification optical microscopy image after the break for CFRP-CFRP SLJ bonded with quick set epoxy when tested under tensile loading conditions at a strain rate of 0.15 $s^{-1}$. From the figure, it can be observed that there is a mixed mode failure similar to the lower strain rate but with higher percentage of interface fracture between adhesive and composite adherend due to peel and some amount of cohesive fracture in adhesive due to shear.

Figure 3.57 shows a DIC strain distribution map near to failure for CFRP-CFRP SLJ bonded with quick set epoxy subjected to a strain rate of 0.15 $s^{-1}$. From the figure, the peak strain for the particular specimen was 0.822 %. From the figure, the intensity of shear strain along the adhesive bondline has decreased from lower strain rate and there is a maximum principal strain visible in the peel region which might have lead to the interface failure between adheisve and adherend.

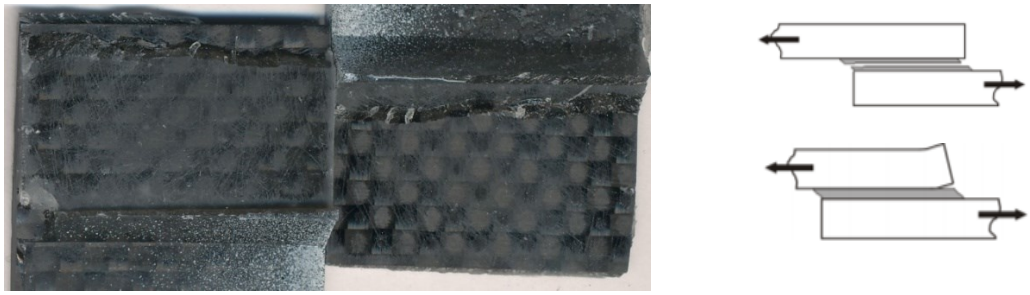

Figure 3.56 Low magnification image after failure for CFRP-CFRP SLJ bonded with quick set epoxy tested at a strain rate of 0.15 $s^{-1}$.

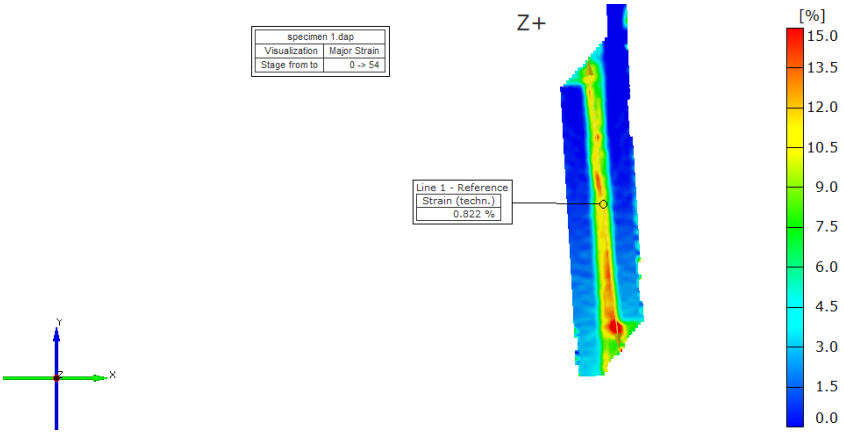


Figure 3.57 DIC strain distribution at failure for CFRP-CFRP SLJ bonded with quick set epoxy tested subjected to a strain rate of 0.15 $s^{-1}$.

### 3.1.3.3 CFRP-CFRP with urethane-based adhesive

Figure 3.58 shows typical stress-strain curves of CFRP-CFRP SLJ bonded with urethane-based adhesive tested under tensile loading conditions at a strain rate of 0.0015 $s^{-1}$. The lap joint was analyzed based on the lap shear strength and peak strain, and it can be observed that the lap joint exhibited an average shear strength of 17.35 MPa and a peak strain of 2.80 %.

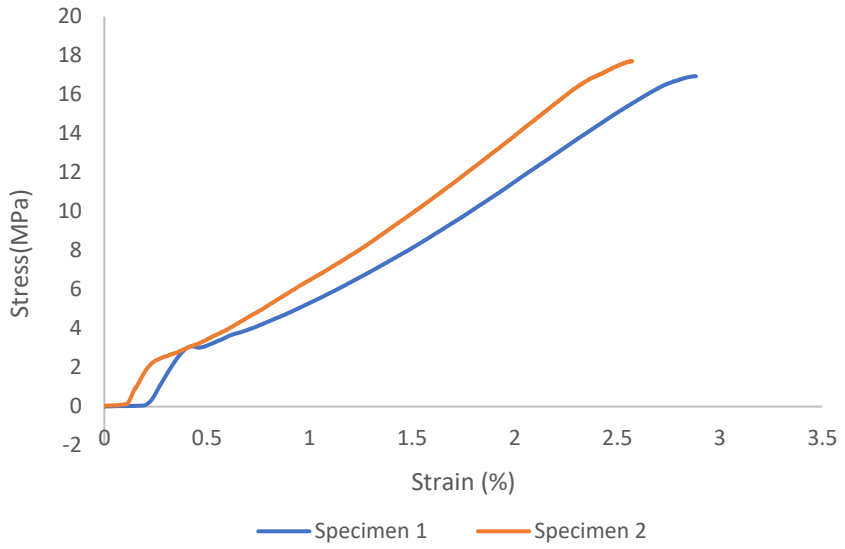


Figure 3.58 Typical stress-strain curve of CFRP-CFRP SLJ bonded with urethane-based adhesive tested at a strain rate of 0.0015 $s^{-1}$.

Figure 3.59 shows a low magnification optical microscopy image after the break for CFRP-CFRP SLJ bonded with urethane-based adhesive when tested under tensile loading conditions at a strain rate of 0.0015 $s^{-1}$. From the figure, it can be observed that there is a cohesive failure in the adhesive due to peel and shear similar to most of the cases where this adhesive was in use.

Figure 3.59 Low magnification image after failure for CFRP-CFRP SLJ bonded with urethane-based adhesive subjected to a strain rate of 0.0015 $s^{-1}$.

Figure 3.60 shows an optical microscopy image captured at 10 × magnification of CFRP-CFRP SLJ bonded with urethane-based adhesive tested under tensile loading conditions at a strain rate of 0.0015 $s^{-1}$. The figure depicts the bond area of the CFRP adherend with adhesive to understand the behavior of composite adherend fracture pattern. It was observed that the urethane adhesive

has undergone shearing and the composite substrate experienced some fiber tear. Moreover, the adhesive's high ductile nature when bonded to composite substrate can be noted.

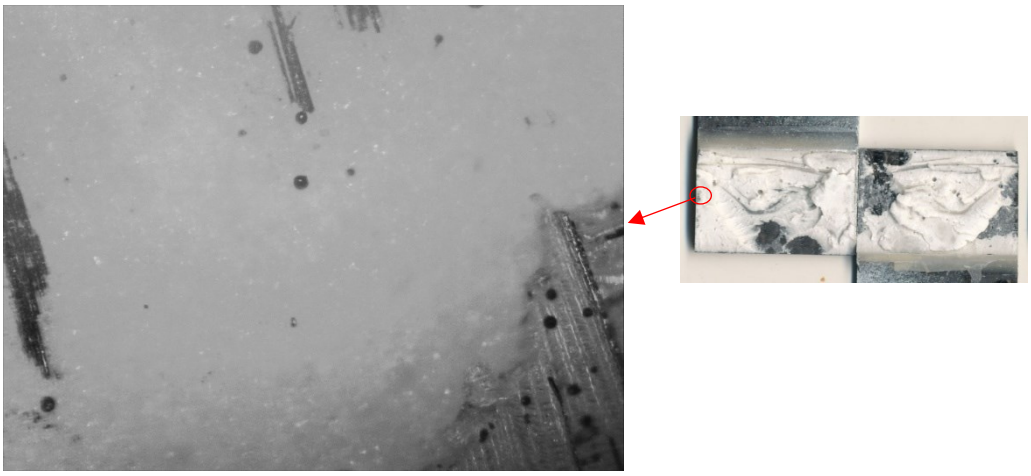

Figure 3.60 Optical microscopy image 10 × magnification of CFRP-CFRP SLJ bonded with urethane-based tested at a strain rate of 0.0015 $s^{-1}$.

Figure 3.61 shows a DIC strain distribution map near to failure for CFRP-CFRP SLJ bonded with urethane-based adhesive subjected to a strain rate of 0.0015 $s^{-1}$. From the figure, the peak strain for the particular specimen was 2.802 %.

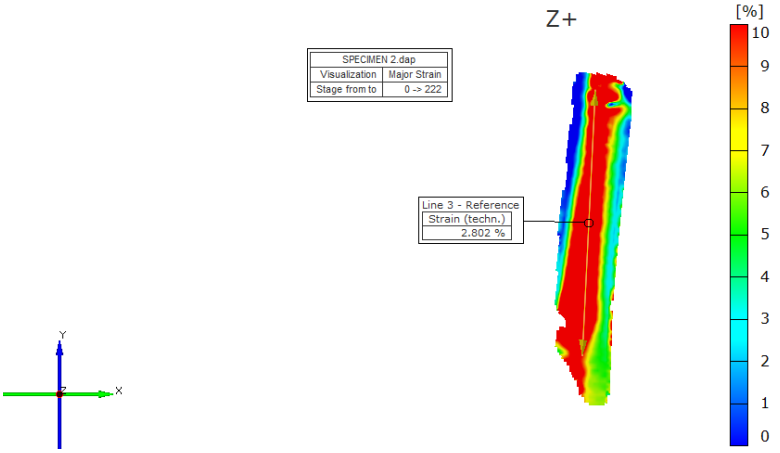


Figure 3.61 DIC strain distribution at failure for CFRP-CFRP SLJ bonded with urethane-based adhesive subjected to a strain rate of 0.0015 $s^{-1}$.

Figure 3.62 shows typical stress-strain curves of CFRP-CFRP SLJ bonded with urethane-based adhesive tested under tensile loading conditions at a strain rate of 0.15 $s^{-1}$. The lap joint was analyzed based on the lap shear strength and peak strain, and it can be observed that the lap joint exhibited an average shear strength of 22.2 MPa and an average peak strain of 2.60 %.

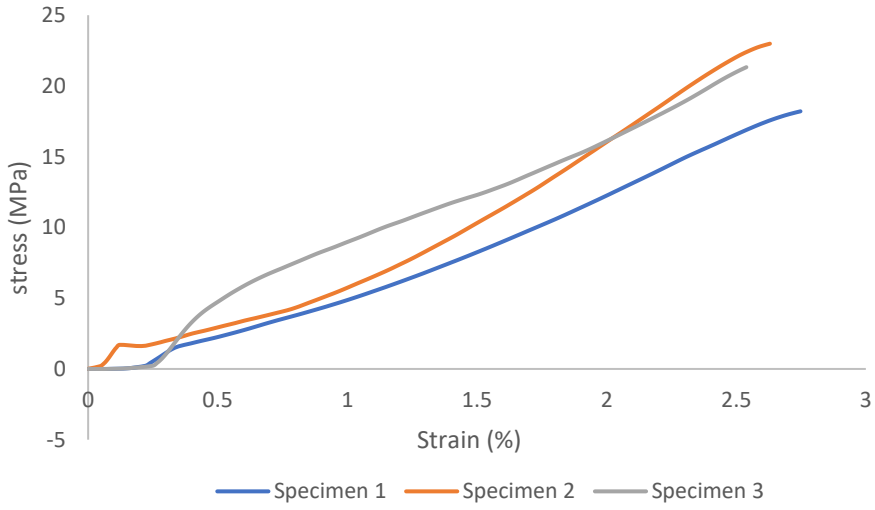


Figure 3.62 Typical stress-strain curve of CFRP-CFRP SLJ bonded with urethane-based adhesive tested under tensile loading conditions at a strain rate of 0.15 $s^{-1}$.

Figure 3.63 shows a low magnification optical microscopy image after the break for CFRP-CFRP SLJ bonded with urethane-based adhesive when tested under tensile loading conditions at a strain rate of 0.15 $s^{-1}$. From the figure, it can be observed that there is a cohesive failure in composite adherend due to interlaminar fracture. It can be concluded that the joint has failed before the maximum adhesive strength reached.

.

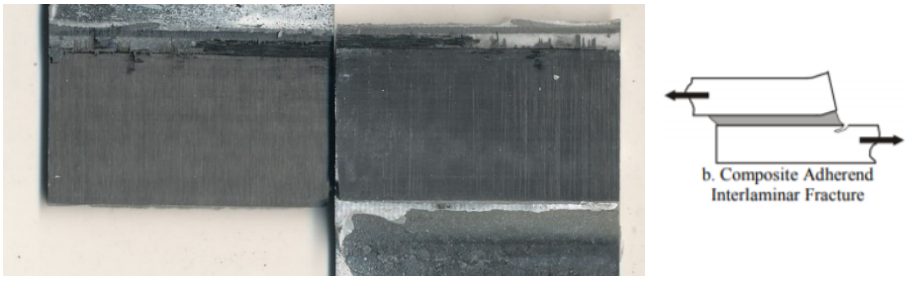


Figure 3.63 Low magnification image after failure for CFRP-CFRP SLJ bonded with urethane-based adhesive subjected to a strain rate of 0.15 $s^{-1}$.

Figure 3.64 shows a DIC strain distribution map near to failure for CFRP-CFRP SLJ bonded with urethane-based adhesive subjected to a strain rate of 0.15 $s^{-1}$. From the figure, the peak strain for the particular specimen was 2.601 %. From the figure,there is large amount of shear and longitudnal strain in the adhesive bondline which is propogating towards the adherends as well.

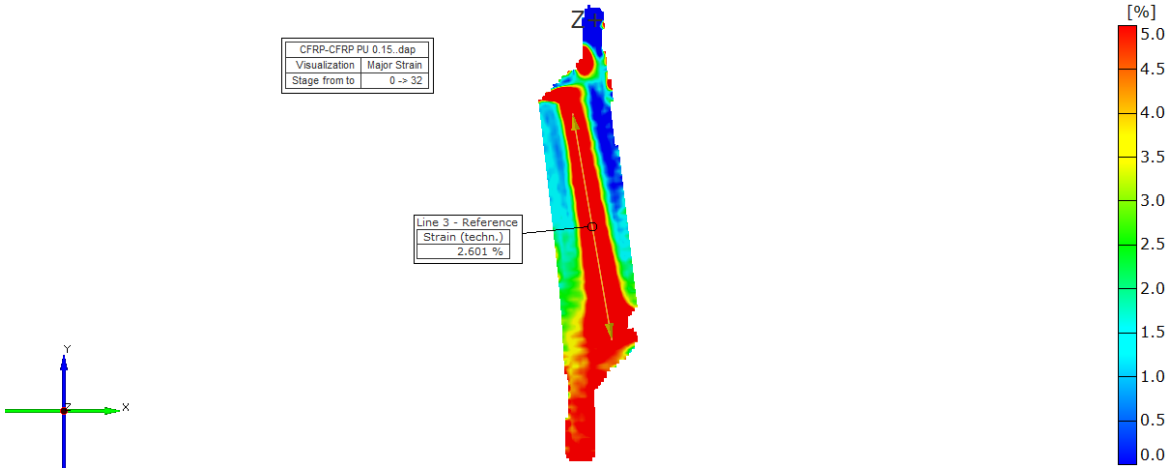


Figure 3.64 DIC strain distribution at failure for CFRP-CFRP SLJ bonded with urethane-based adhesive subjected to a strain rate of 0.15 $s^{-1}$.

## 3.2 Dynamic tensile testing

### 3.2.1 Aluminum alloy joints

Aluminum alloy joints were tested under tensile loading conditions at a strain rate of 15 $s^{-1}$ and 150 $s^{-1}$ which account to a crosshead speed of 14000 mm/min and 140000 mm/min. The aluminum joints were bonded with three adhesives chosen and similar to quasi-static loading, lap shear strength is produced from the mechanical testing unit, and strain distributions and peak strain values were obtained from 2D digital image correlation technique.

### 3.2.1.1 Al6061 – Al6061 with high strength epoxy

Figure 3.65 shows typical stress-strain curves of Al-Al SLJ bonded with high strength epoxy tested under tensile loading conditions at a strain rate of 15 $s^{-1}$. The lap joint was analyzed based on the lap shear strength and peak strain, can be observed that the lap joint exhibited an average shear strength of 8.84 MPa and an average peak strain of 0.16 %.

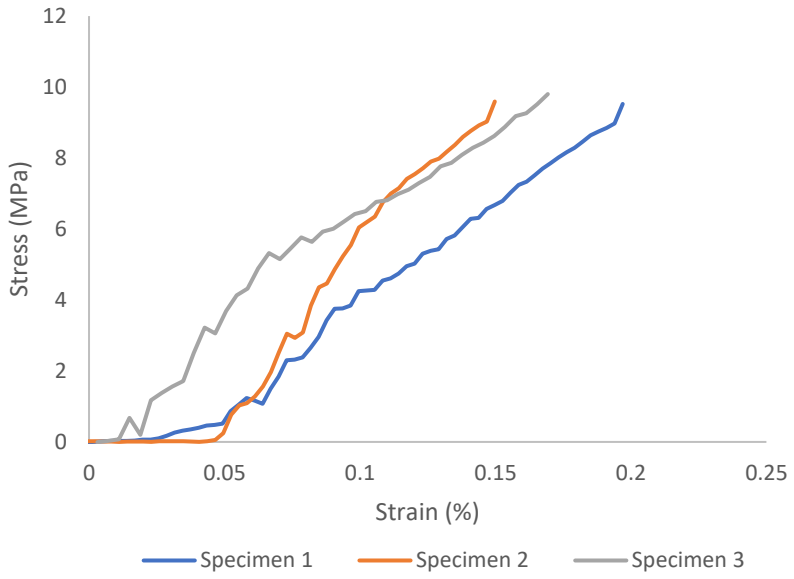


Figure 3.65 Typical stress-strain curve of Al-Al SLJ bonded with high strength epoxy tested under tensile loading conditions at a strain rate of 15 $s^{-1}$.

Figure 3.66 shows a low magnification optical microscopy image after the break for Al-Al SLJ bonded with high strength epoxy when tested under tensile loading conditions at a strain rate of 15 $s^{-1}$. From the figure, it can be observed that it is an interface failure between adhesive and adherend and a little cohesive failure in adhesive due to peeling.

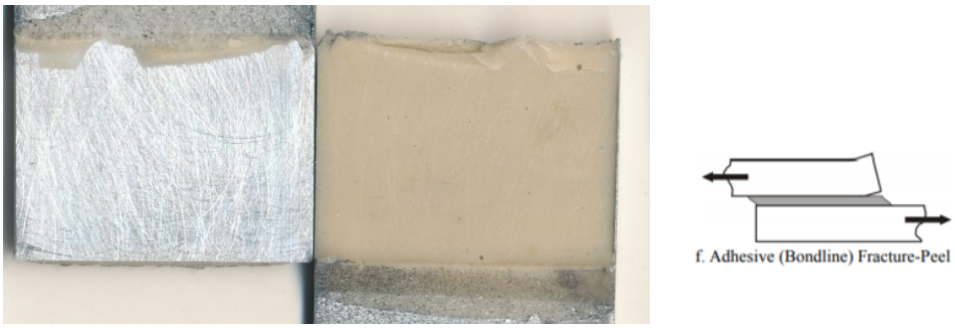


Figure 3.66 Low magnification image after failure for AL-Al SLJ bonded with high strength epoxy tested subjected to a strain rate of 15 $s^{-1}$.

Figure 3.67 shows a DIC strain distribution map near to failure for Al-Al SLJ bonded with high strength epoxy subjected to a strain rate of 15 $s^{-1}$. From the figure, the peak strain for the particular specimen was 0.161 %. From the figure, it is observed that the adhesive failure is due to peeling and peak strain are visibel at peel region in top and bottom. Figure 3.68 shows typical stress-strain curves of Al-Al SLJ bonded with high strength epoxy tested under tensile loading conditions at a strain rate of 150 $s^{-1}$. The lap joint was analyzed based on the lap shear strength and peak strain, and it can be observed that the lap joint exhibited an average shear strength of 11.2 MPa and an average peak strain of 0.155 %. There is noise observed across the curve which can be due to settling of specimen in the grips.

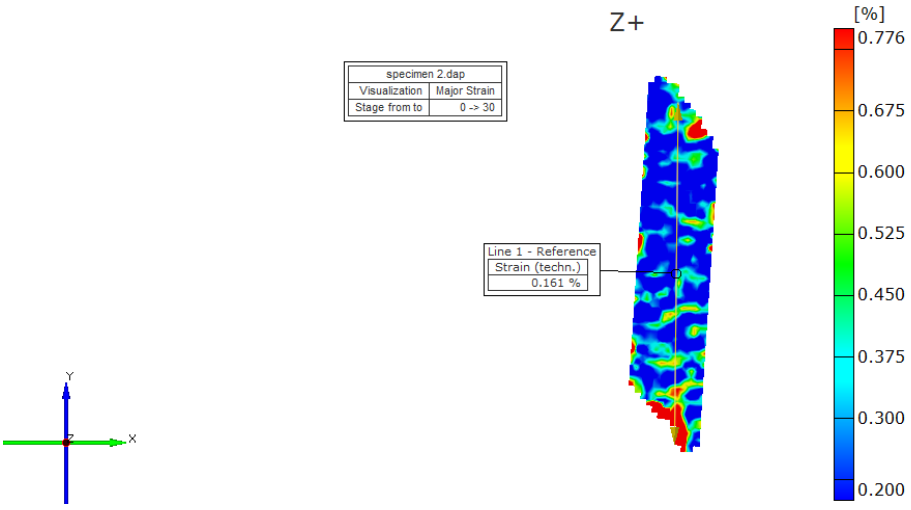


Figure 3.67 DIC strain distribution at failure for Al-Al SLJ bonded with high strength epoxy tested subjected to a strain rate of 15 $s^{-1}$.

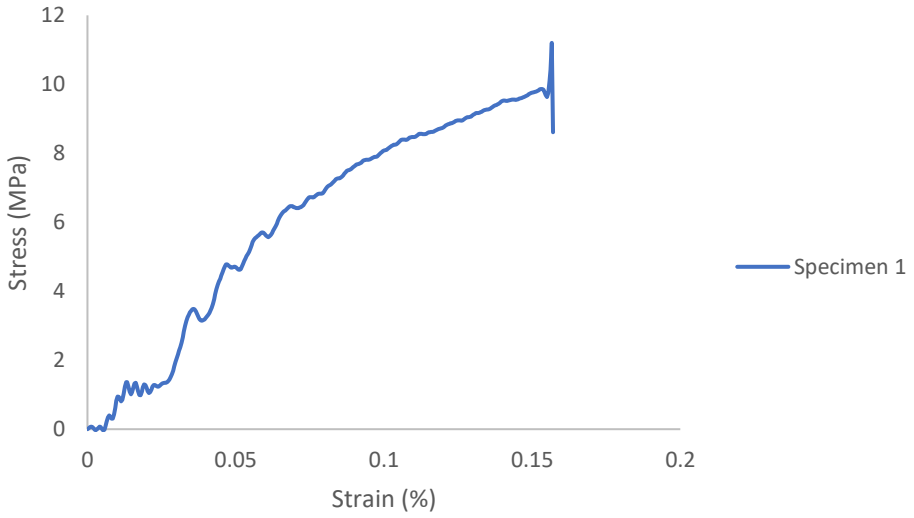


Figure 3.68 Typical stress vs strain behavior for Al-Al SLJ bonded with high strength epoxy at a strain rate of 150 $s^{-1}$.

Figure 3.69 shows a low magnification optical microscopy image after the break for Al-Al SLJ bonded with high strength epoxy when tested under tensile loading conditions at a strain rate of 150 $s^{-1}$. From the figure, it can be observed that it is an interface failure between adhesive and adherend and a little cohesive failure in adhesive due to peeling which is similar to the lower strain rate behavior.


Figure 3.69 Low magnification image after failure for AL-Al SLJ bonded with high strength epoxy subjected to a strain rate of 150 $s^{-1}$.

Figure 3.70 shows an optical microscopy image captured at 10 × magnification of Al-Al SLJ bonded with high strength epoxy tested under tensile loading conditions at a strain rate of 150 $s^{-1}$.

Here, it can be observed that the adhesion between the adherend and adhesive is good and there is no residue from the adhesive on the substrate.

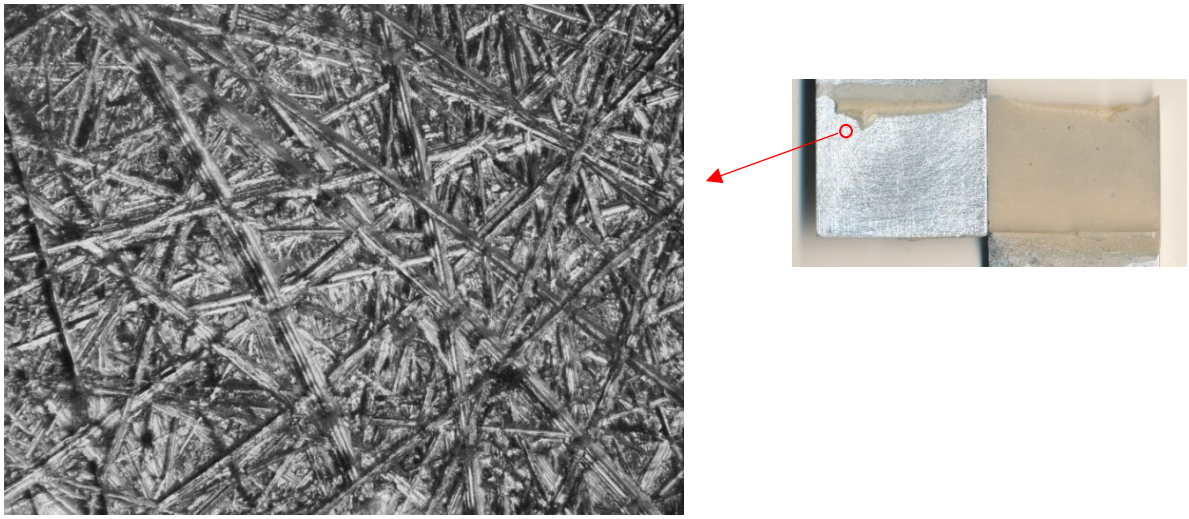

Figure 3.70 Optical microscopy image 10× magnification of Al-Al SLJ bonded with high strength epoxy tested at a strain rate of 150 $s^{-1}$.

Figure 3.71 shows a DIC strain distribution map near to failure for Al-Al SLJ bonded with high strength epoxy subjected to a strain rate of 150 $s^{-1}$. From the figure, the strain near to failure for the particular specimen was 0.167 % and it is observed that the adhesive failure is due to peeling in the bottom region and the optical microscopy image revealed that there is no residue of epoxy formed on the aluminum adherend. Ths conforms the brittle behavior of the high strength epoxy.

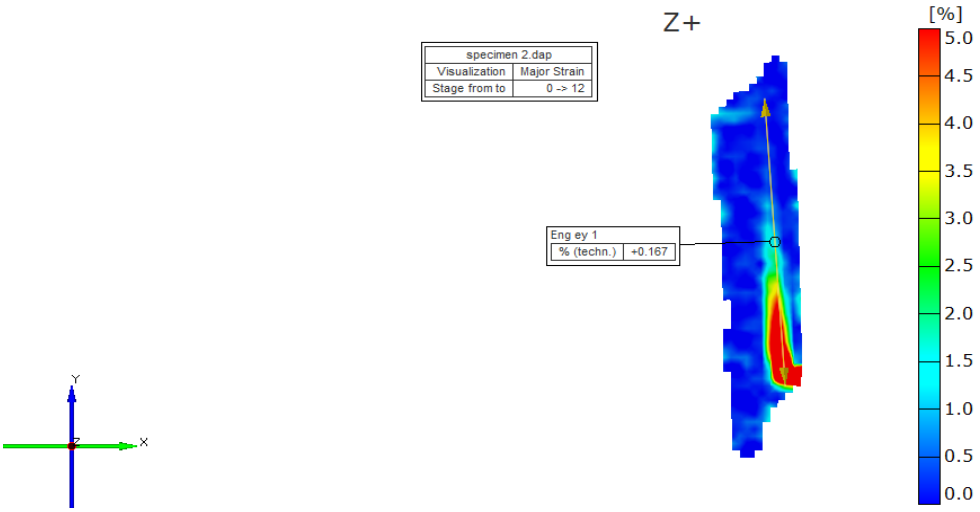


Figure 3.71 DIC strain distribution at failure for Al-Al SLJ bonded with high strength epoxy subjected to a strain rate of 150 $s^{-1}$.

### 3.2.1.2 Al6061 – Al6061 with quick set epoxy

Figure 3.72 shows typical stress-strain curves of Al-Al SLJ bonded with quick set epoxy tested under tensile loading conditions at a strain rate of 15 $s^{-1}$. The lap joint was analyzed, and it can be observed that the lap joint exhibited an average shear strength of 4.95 MPa and an average peak strain of 0.18 %. There is noise observed across the curve which can be due to settling of specimen in the grips.

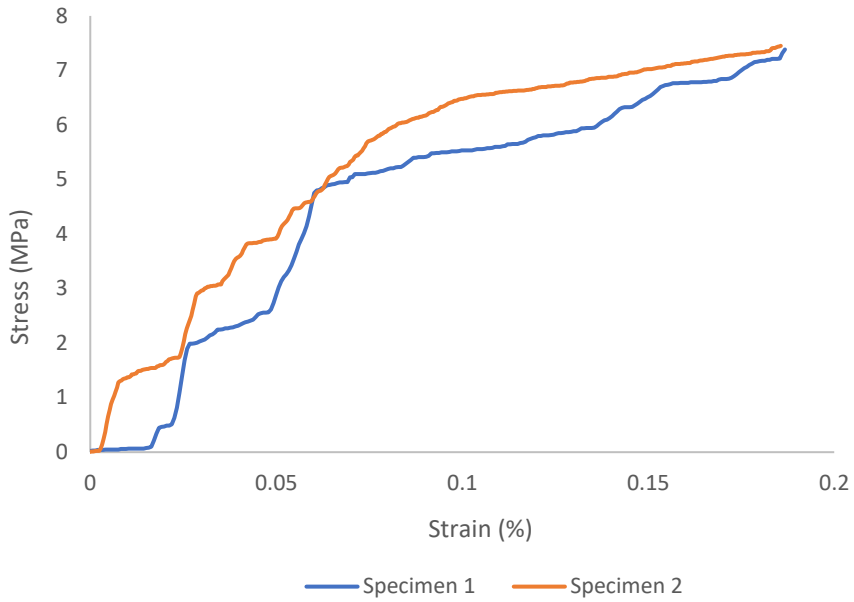


Figure 3.72 Typical stress vs strain behavior for Al-Al SLJ bonded with quick set epoxy at a strain rate of 15 $s^{-1}$.

Figure 3.73 shows a low magnification optical microscopy image after the break for Al-Al SLJ bonded with quick set epoxy when tested under tensile loading conditions at a strain rate of 15 $s^{-1}$. From the figure, it can be observed that it is an interface failure between adhesive and adherend and a little cohesive failure in adhesive due to peeling. Figure 3.74 shows a DIC strain distribution map near to failure for Al-Al SLJ bonded with quick set epoxy subjected to a strain rate of 15 $s^{-1}$. From the figure, the strain near failure for the particular specimen was 0.167 % and it is observed that the adhesive failure is due to peeling in the bottom and top region. A manually scaled of legend is presented to avoid the visibility of nosie in the deformation.

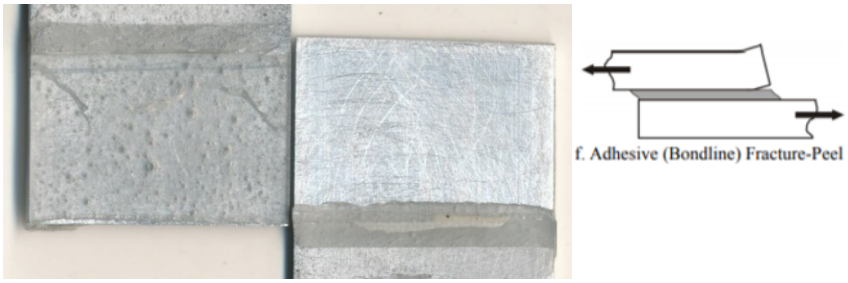


Figure 3.73 Low magnification image after failure for Al-Al SLJ bonded with quick set epoxy subjected to a strain rate of 15 $s^{-1}$.

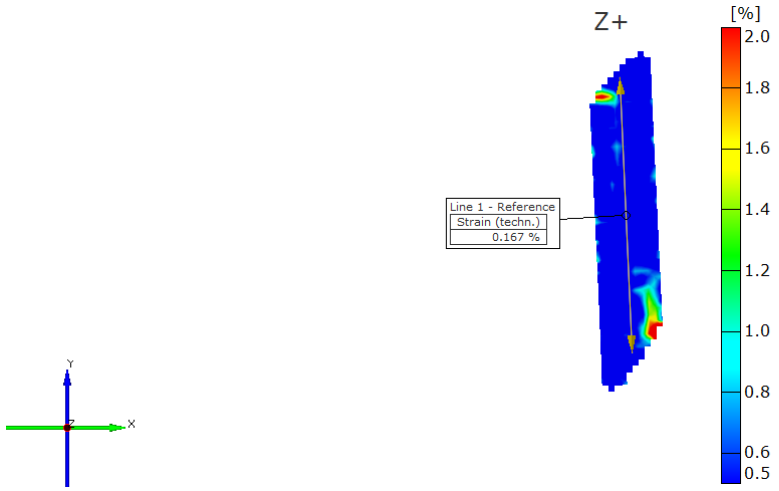


Figure 3.74 DIC strain distribution at failure for Al-Al SLJ bonded with quick set epoxy subjected to a strain rate of 15 $s^{-1}$.

Figure 3.75 shows typical stress-strain curves of Al-Al SLJ bonded with quick set epoxy tested under tensile loading conditions at a strain rate of 150 $s^{-1}$. The lap joint was analyzed, and it was observed that the lap joint exhibited an average shear strength of 15.94 MPa and an average peak strain of 0.115 %.

Figure 3.76 shows a low magnification optical microscopy image after break for Al-Al SLJ bonded with quick set epoxy when tested under tensile loading conditions at a strain rate of 150 $s^{-1}$. From the figure, it can be observed that it is an interface failure between adhesive and adherend and a little cohesive failure in adhesive due to peeling and we can see a large absorption of energy with adhesive system which resulted in the formation of pores. This is called as dissipative failure in adhesive [77].

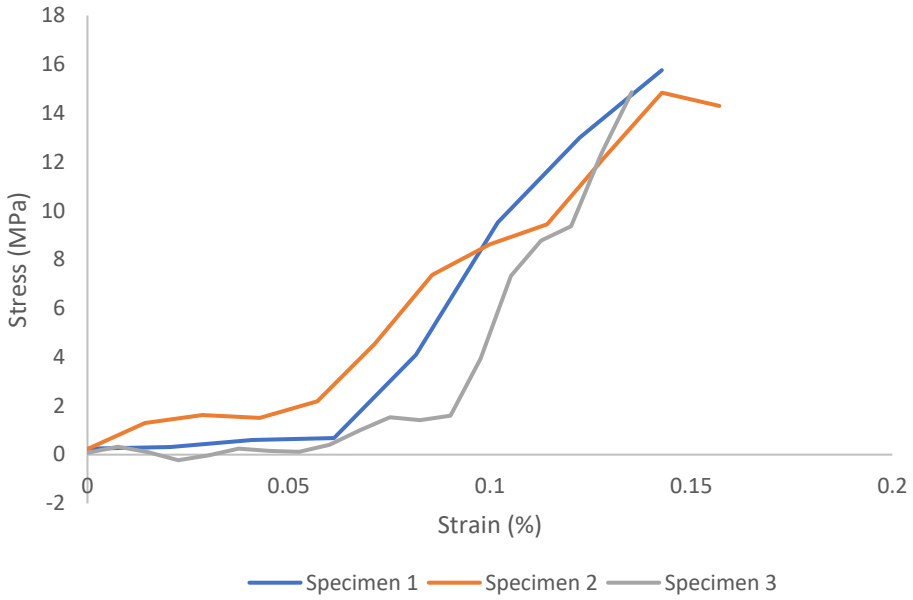


Figure 3.75 Typical stress vs strain behavior for Al-Al SLJ bonded with quick set epoxy under tensile loading conditions at a strain rate of 150 $s^{-1}$.

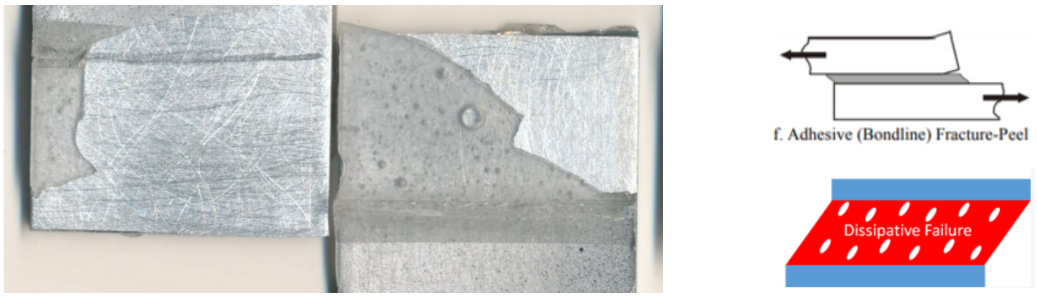


Figure 3.76 Low magnification image after failure for Al-Al SLJ bonded with quick set epoxy tested subjected to a strain rate of 150 $s^{-1}$.

Figure 3.77 shows an optical microscopy revealed that the aluminum oxide is formed on the adhesive which might have weakened the bond which lead to failure. Significantly, the break of bond could be due to peel as there is not much sign of shearing observed.

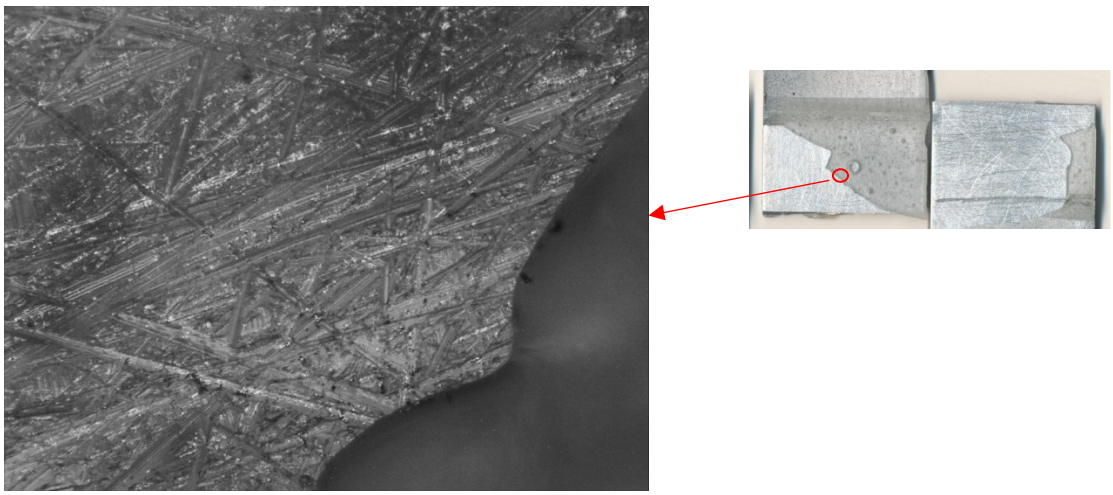

Figure 3.77 Optical microscopy image 10 × magnification of Al-Al SLJ bonded with quick set epoxy tested under tensile loading conditions at a strain rate of 150 $s^{-1}$.

Figure 3.78 shows DIC strain distribution map near to failure for Al-Al SLJ bonded with quick set epoxy subjected to a strain rate of 150 $s^{-1}$. From the figure, the peak strain for the particular specimen was 0.403 % and it is observed that the adhesive failure is due to peeling in the bottom and top region.

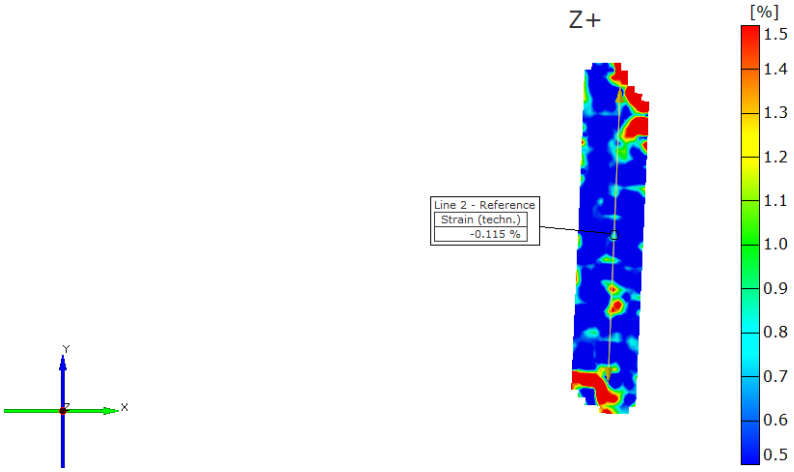


Figure 3.78 DIC strain distribution at failure for Al-Al SLJ bonded with quick set epoxy tested subjected to a strain rate of 150 $s^{-1}$.

### 3.2.1.3 Al6061 – Al6061 with urethane-based adhesive

Figure 3.79 shows typical stress-strain curves of Al-Al SLJ bonded with urethane-based adhesive tested under tensile loading conditions at a strain rate of 15 $s^{-1}$. It was observed that the lap joint exhibited an average shear strength of 17.25 MPa and an average peak strain of 1.43 %.

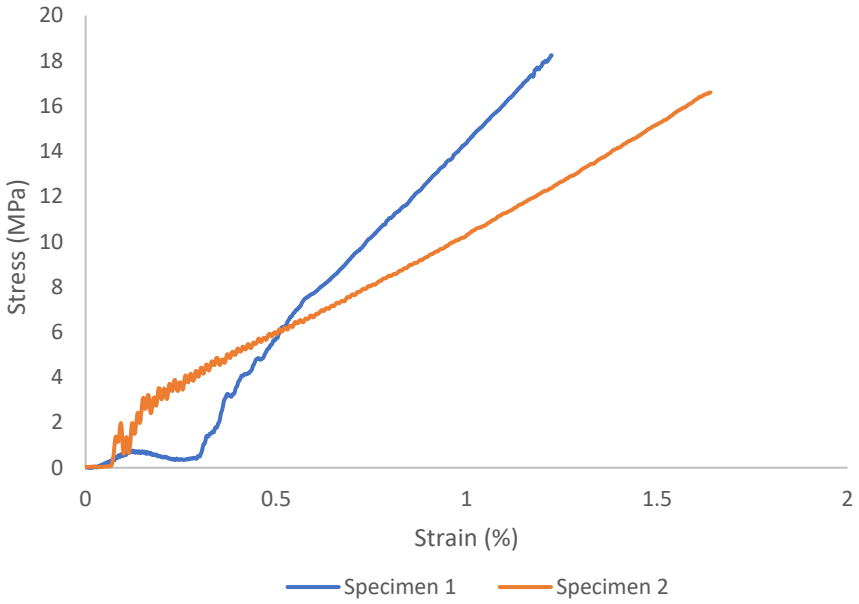


Figure 3.79 Typical stress vs strain behavior for Al-Al SLJ bonded with urethane-based adhesive at a strain rate of 15 $s^{-1}$.

Figure 3.80 shows a low magnification optical microscopy image after break for Al-Al SLJ bonded with urethane-based adhesive when tested under tensile loading conditions at a strain rate of 15 $s^{-1}$. From the figure, it can be observed that it is mixed mode failure with near interface failure between adhesive and adherend due to shear and a cohesive fracture in adhesive failure mode as cracks were initiated in the adhesive.


Figure 3.80 Low magnification image after failure for Al-Al SLJ bonded with urethane-based adhesive subjected to a strain rate of 15 $s^{-1}$.

Figure 3.81 shows a DIC strain distribution map near to failure for Al-Al SLJ bonded with urethane-based adhesive subjected to a strain rate of 15 $s^{-1}$. From the figure, the peak strain for the particular specimen was 0.849 %, and it is observed that the adhesive failure is due to peeling in the bottom and top region.

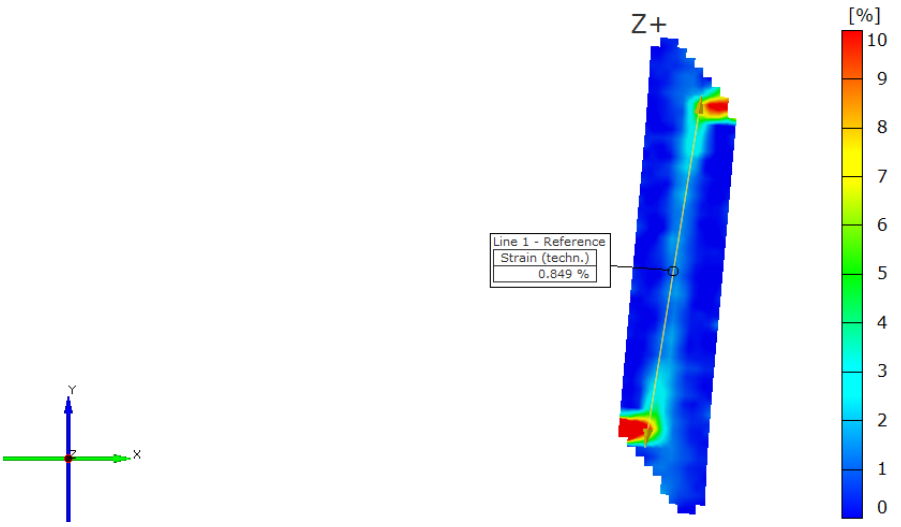


Figure 3.81 DIC strain distribution at failure for Al-Al SLJ bonded with urethane-based adhesive tested subjected to a strain rate of 15 $s^{-1}$.

Figure 3.82 shows typical stress-strain curves of Al-Al SLJ bonded with urethane-based adhesive tested under tensile loading conditions at a strain rate of 150 $s^{-1}$. The lap joint was analyzed based on the lap shear strength and peak strain, and it can be observed that the lap joint exhibited an average shear strength of 19.65 MPa and an average peak strain of 0.96 %.

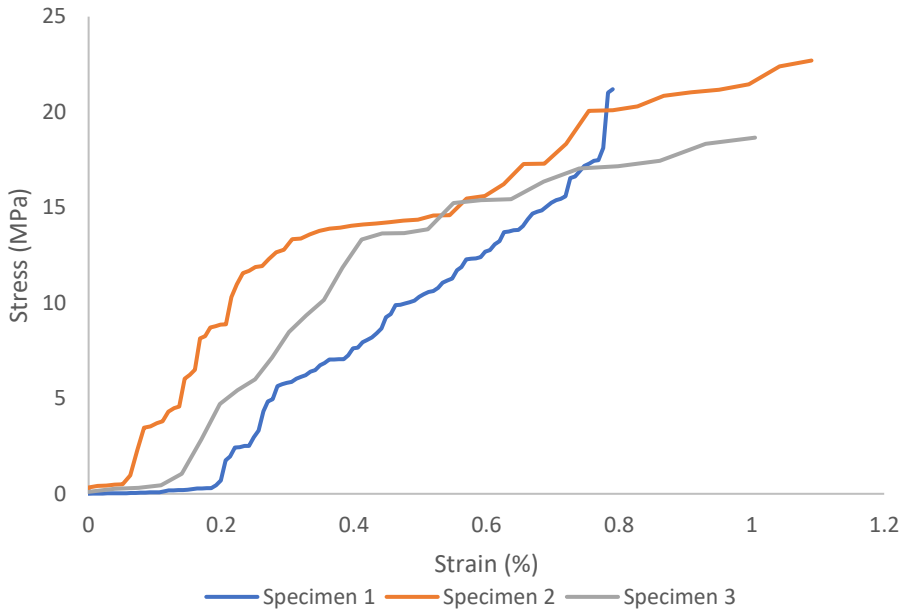


Figure 3.82 Typical stress vs. strain behavior for Al-Al SLJ bonded with urethane-based adhesive subjected to a strain rate of 150 $s^{-1}$.

Figure 3.83 shows a low magnification optical microscopy image after the break for Al-Al SLJ bonded with urethane-based adhesive when tested under tensile loading conditions at a strain rate of 150 $s^{-1}$. Furthermore, it can be observed that a near interface failure between adhesive and adherend due to shear which suggests that the adhesive and adherend were affected locally.

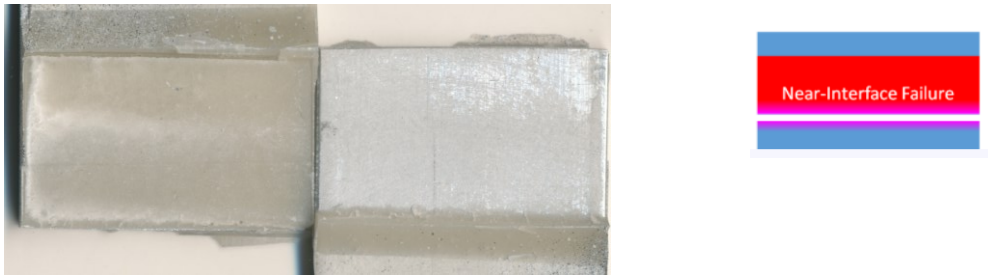


Figure 3.83 Low magnification image after failure for Al-Al SLJ bonded with urethane-based adhesive subjected to a strain rate of 150 $s^{-1}$.

Figure 3.84 shows an optical microscopy image captured at 10 × magnification of Al-Al SLJ bonded with urethane-based adhesive tested under tensile loading conditions at a strain rate of 150 $s^{-1}$. Particularly with the increase in strain rate, the bond with urethane adhesive shifted from

cohesive failure in adhesive to near interface failure between adhesive and adherend. This special type failure was also observed in the higher strain rates of urethane-based adhesive. From the figure, it can be perceived that the urethane-based adhesive has formed a good bond with aluminum adherend.

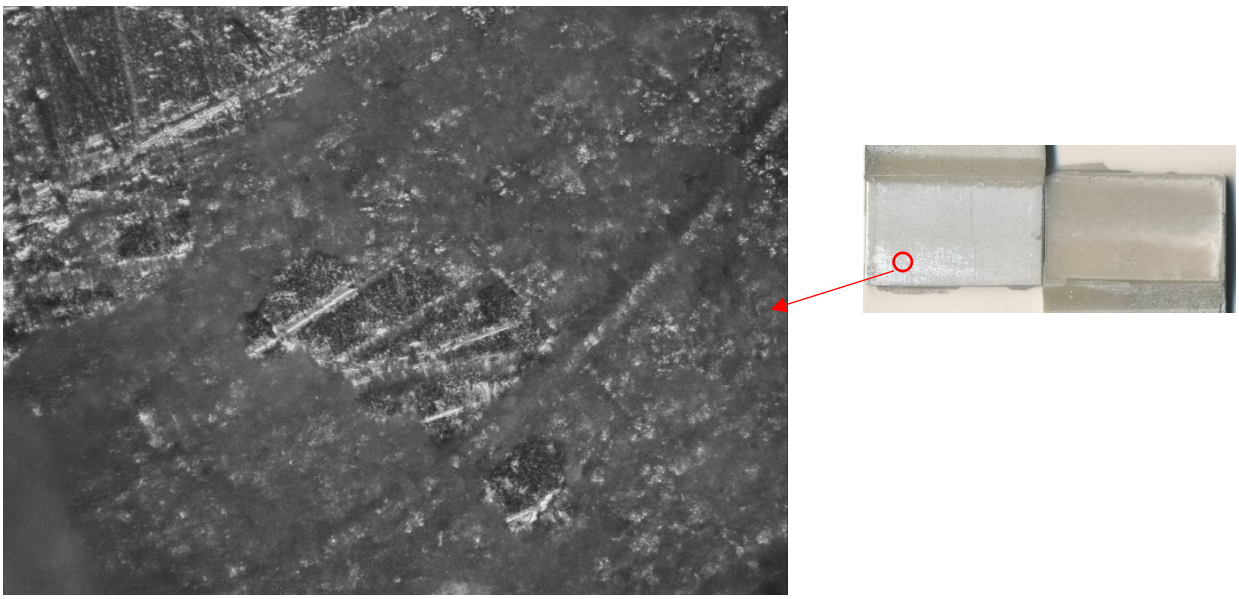

Figure 3.84 Optical microscopy image captured at 10 × magnification of Al-Al SLJ bonded with urethane-based adhesive tested subjected to a strain rate of 150 $s^{-1}$.

Figure 3.85 shows a DIC strain distribution map near to failure for Al-Al SLJ bonded with urethane-based adhesive tested under tensile loading conditions subjected to a strain rate of 150 $s^{-1}$. From the figure, the peak strain for the particular specimen was 0.659 % and it is observed that the adhesive failure is due to peeling in the bottom and top region. It can be seen that there is significant amount of strain spread out in the adhesive bondline region which can be due to shearing.

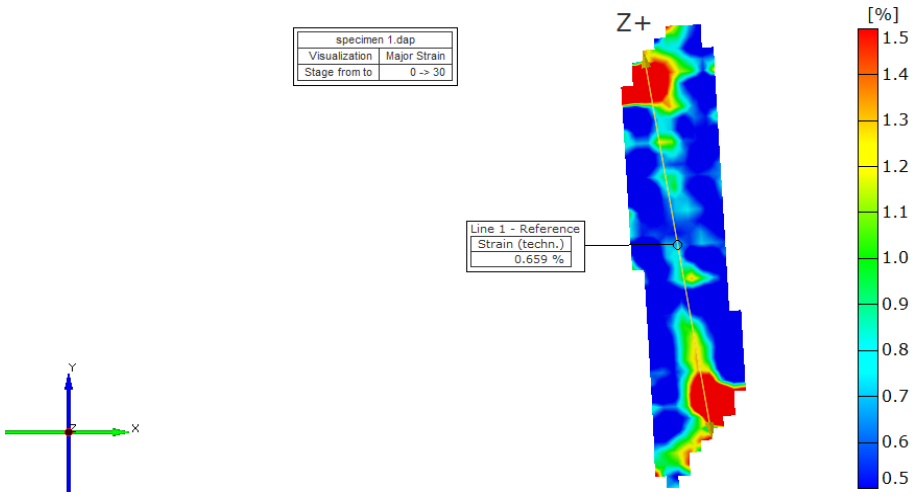


Figure 3.85 DIC strain distribution at failure for Al-Al SLJ bonded with urethane based adhesive subjected to a strain rate of 150 $s^{-1}$.

### 3.2.2 Aluminum – composite joints

#### 3.2.2.1 Al6061-CFRP with high strength epoxy

Figure 3.86 shows typical stress-strain curve of Al-CFRP SLJ bonded with high strength epoxy tested under tensile loading conditions at a strain rate of 15 $s^{-1}$. The lap joint was analyzed based on the lap shear strength and peak strain, and it can be observed that the lap joint exhibited an average shear strength of 13.49 MPa and an average peak strain of 0.12 %.

Figure 3.87 shows a low magnification optical microscopy image after the break for Al-CFRP SLJ bonded with high strength epoxy when tested under tensile loading conditions at a strain rate of 15 $s^{-1}$. From the figure, it can be observed that an interface failure between adhesive and aluminum alloy adherend. Furthermore, due to the crosshead speed, the adhesive broke in pieces during the test.

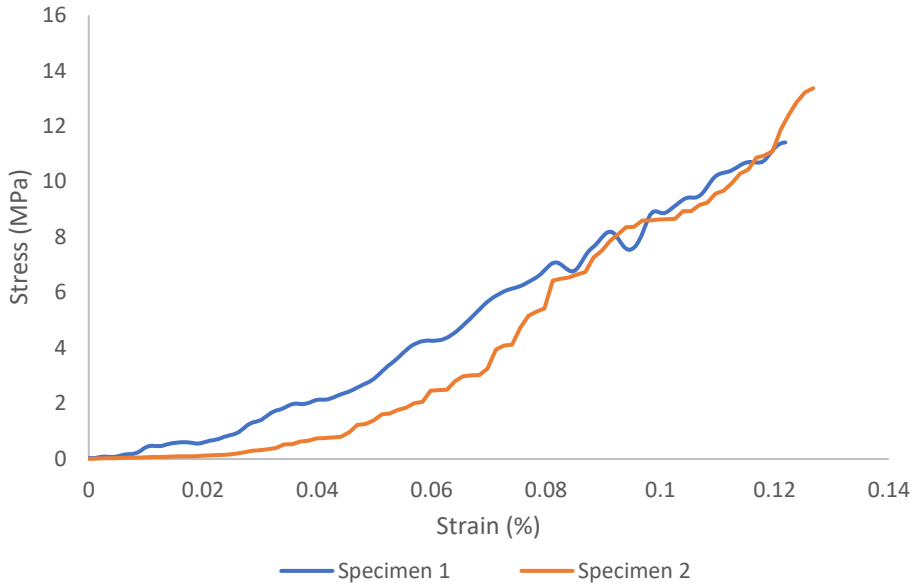


Figure 3.86 Typical stress vs. strain behavior for Al-CFRP SLJ bonded with high strength epoxy subjected to a strain rate of 15 $s^{-1}$.


Figure 3.87 Low magnification image after failure for Al-CFRP SLJ bonded with high strength epoxy subjected to a strain rate of 15 $s^{-1}$.

Figure 3.88 shows a DIC strain distribution map near to failure for Al-CFRP SLJ bonded with high strength epoxy subjected to a strain rate of 15 $s^{-1}$. From the figure, the strain near to failure for the particular specimen was 0.116 %, and it was observed that the adhesive failure was due to shear in the top region and the break in the adhesive (fig. 3.62) is due to the maximum strain accumulation in the top region.

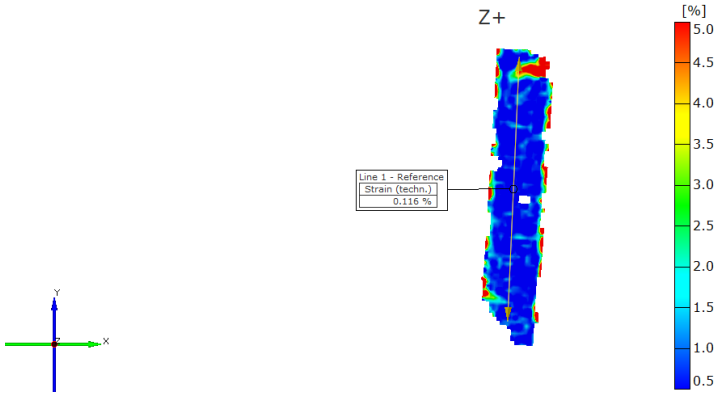


Figure 3.88 DIC strain distribution at failure for Al-CFRP SLJ bonded with high strength epoxy subjected to a strain rate of 15 $s^{-1}$.

Figure 3.89 shows typical stress-strain curves of Al-CFRP SLJ bonded with high strength epoxy tested under tensile loading conditions at a strain rate of 150 $s^{-1}$. The lap joint was analyzed based on the lap shear strength and peak strain, and it can be observed that the lap joint exhibited an average shear strength of 17.13 MPa and an average peak strain of 0.05 %.

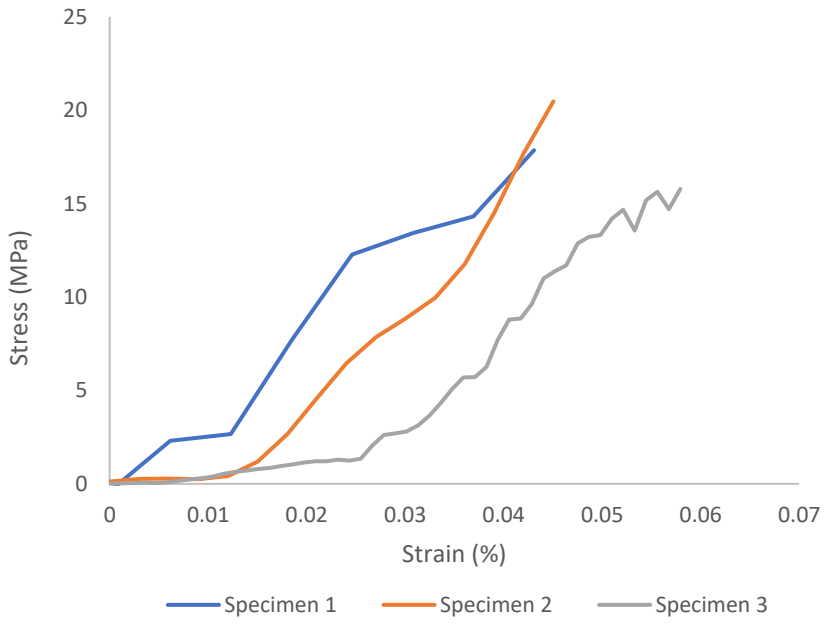


Figure 3.89 Typical stress vs. strain behavior for Al-CFRP SLJ bonded with high strength epoxy subjected to a strain rate of 150 $s^{-1}$.

Figure 3.90 shows a low magnification optical microscopy image after the break for Al-CFRP SLJ bonded with high strength epoxy when tested under tensile loading conditions at a strain rate of 150 $s^{-1}$. From the figure 3.90, it can be observed that an interface failure between adhesive and aluminum alloy adherend. The failure mode was similar to the lower strain rate but in this case, the adhesive was able to withstand the speed of crosshead.


Figure 3.90 Low magnification image after failure for Al-CFRP SLJ bonded with high strength epoxy tested subjected to a strain rate of 150 $s^{-1}$.

Figure 3.91 shows an optical microscopy image captured at 10 × magnification of Al-CFRP SLJ bonded with high strength epoxy tested under tensile loading conditions at a strain rate of 150 $s^{-1}$. Here, the aluminum substrate was investigated under microscope at 10 × magnification and it was found that there are traces of epoxy residue on the substrate which was not visible in the low magnification image.

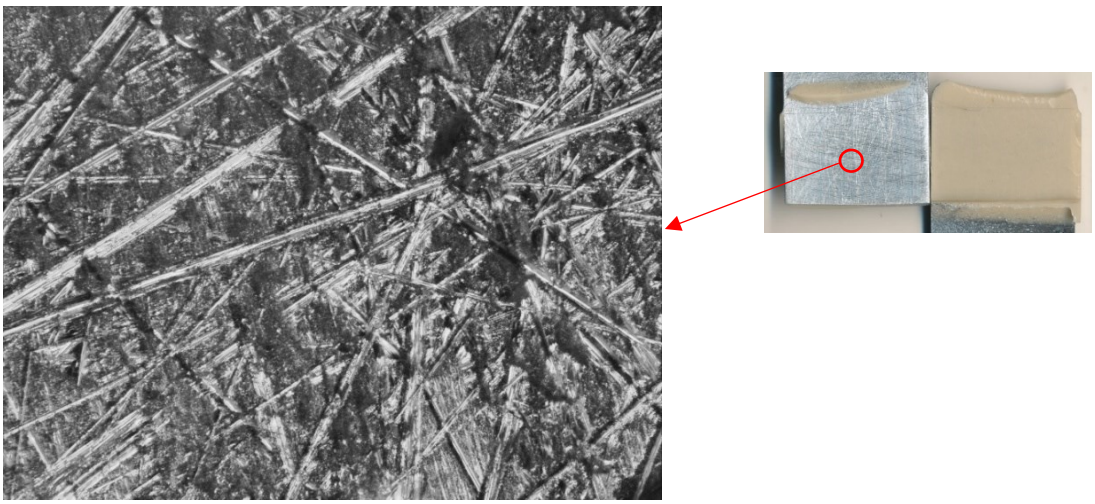

Figure 3.91 Optical microscopy image captured at 10 × magnification of Al-CFRP SLJ bonded with high strength epoxy tested at a strain rate of 150 $s^{-1}$.

Figure 3.92 shows a DIC strain distribution map near to failure for Al-CFRP SLJ bonded with high strength epoxy subjected to a strain rate of 150 $s^{-1}$. From the figure, the peak strain for the particular specimen was 0.045, and it was observed that the adhesive failure was due to shear between aluminum adherend and adhesive. The strain distribution is much pronounced in the higher strain rate test coupon.

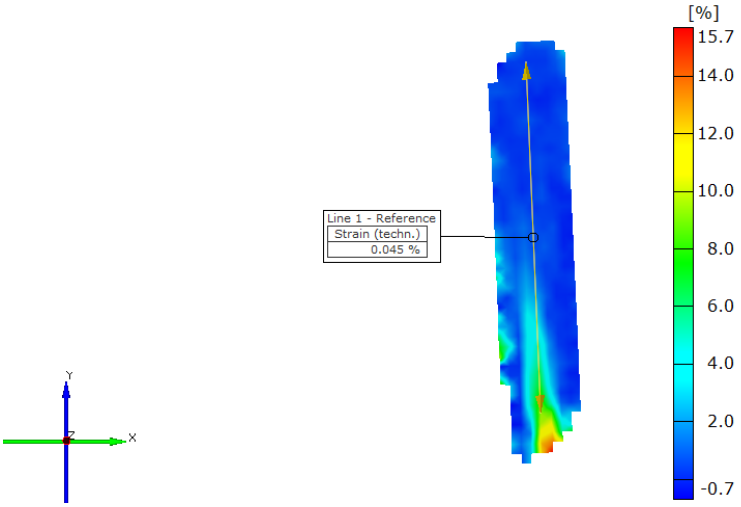


Figure 3.92 DIC strain distribution at failure for Al-CFRP SLJ bonded with high strength epoxy subjected to a strain rate of 150 $s^{-1}$.

### 3.2.2.2 Al6061-CFRP with quick set epoxy

Figure 3.93 shows typical stress-strain curves of Al-CFRP SLJ bonded with quick set epoxy tested under tensile loading conditions at a strain rate of 15 $s^{-1}$. The lap joint was analyzed based on the lap shear strength and peak strain, and it can be observed that the lap joint exhibited an average shear strength of 11.74 MPa and an average peak strain of 0.40 %.

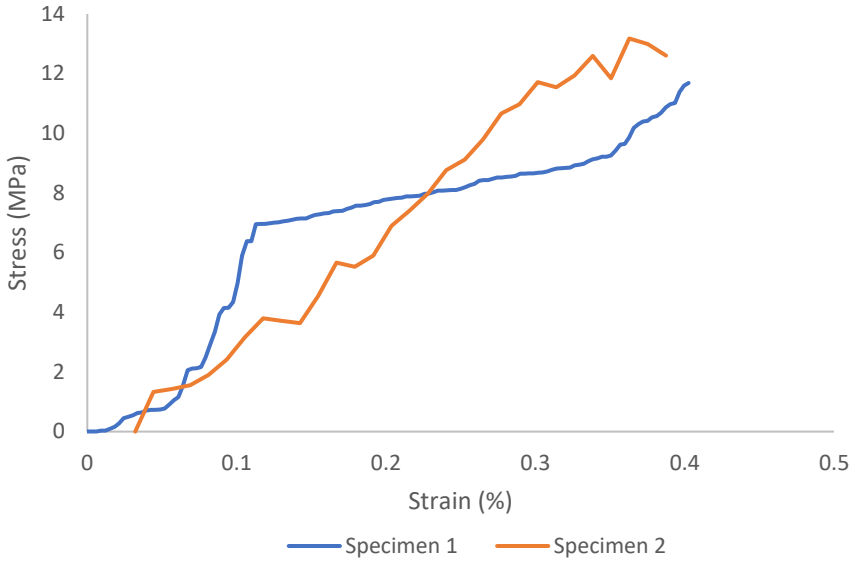


Figure 3.93 Typical stress vs strain behavior for Al-CFRP SLJ bonded with quick set epoxy tested subjected to a strain rate of 15 $s^{-1}$.

Figure 3.94 shows a low magnification optical microscopy image after the break for Al-CFRP SLJ bonded with quick set epoxy when tested under tensile loading conditions at a strain rate of 15 $s^{-1}$. From the figure, it was observed that it is a mixed mode failure with cohesive failure in carbon fiber substrate due to interlaminar fracture and some amount of interface failure between composite adherend and epoxy. The typical behavior of quick set epoxy i.e, formation of pores due to diffusion forces between adhesive and substrate can also be observed.


Figure 3.94 Low magnification image after failure for Al-CFRP SLJ bonded with quick set epoxy subjected to a strain rate of 15 $s^{-1}$.

Figure 3.95 shows a DIC strain distribution map near to failure for Al-CFRP SLJ bonded with quick set epoxy tested under tensile loading conditions subjected to a strain rate of 15 $s^{-1}$. From the figure 3.95, the peak strain for the particular specimen was 0.419 % and the there some amount of strain accumulated in the top portion and propogating towards the middle section which might have resulted in the shearing between composite adherend and epoxy adhesive.

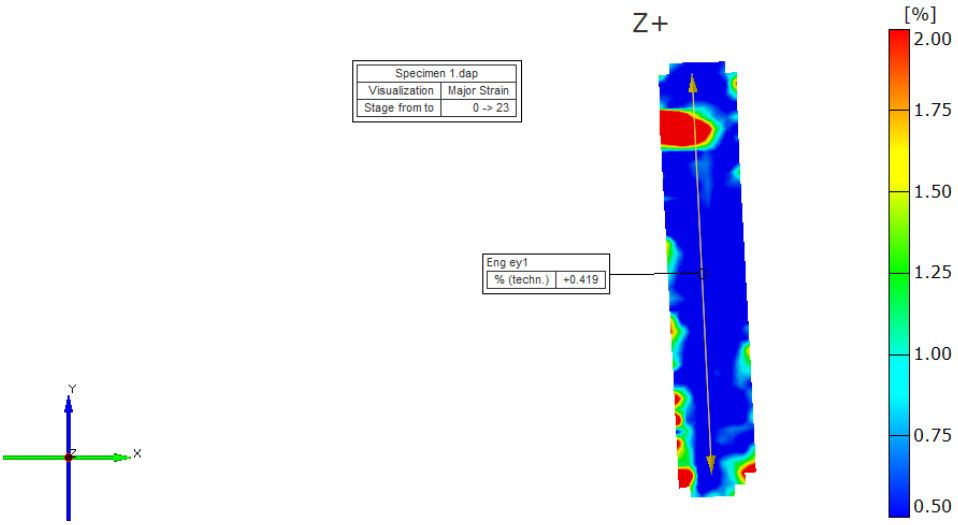


Figure 3.95 DIC strain distribution at failure for Al-CFRP SLJ bonded with quick set epoxy tested subjected to a strain rate of 15 $s^{-1}$.

Figure 3.96 shows typical stress-strain curves of Al-CFRP SLJ bonded with quick set epoxy tested under tensile loading conditions at a strain rate of 150 $s^{-1}$. The lap joint was analyzed based on the lap shear strength and peak strain, and it can be observed that the lap joint exhibited an average shear strength of 18.53 MPa and an average peak strain of 0.38 %. Figure 3.97 shows a low magnification optical microscopy image after the break for Al-CFRP SLJ bonded with quick set epoxy when tested under tensile loading conditions at a strain rate of 150 $s^{-1}$. From the figure, it was observed that it is a mixed mode failure with cohesive failure in carbon fiber substrate due to interlaminar fracture and some amount of interface failure between composite adherend and epoxy. The failure modes were similar to the lower strain rate. The evoultion of break pattern of this combination from quasi-static to dynamic loading conditions shifted from adhesive failure to cohesive failure in CFRP substrate.

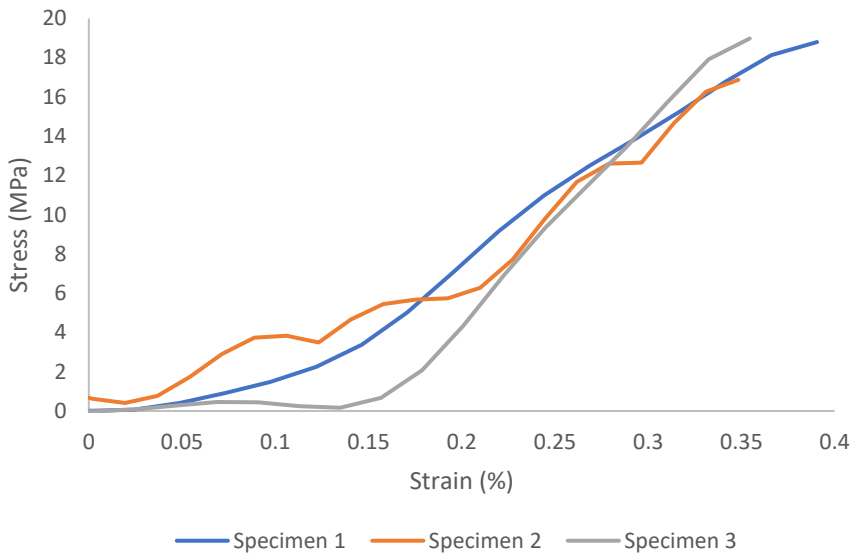


Figure 3.96 Typical stress vs strain behavior for Al-CFRP SLJ bonded with quick set epoxy tested subjected to a strain rate of 150 $s^{-1}$.

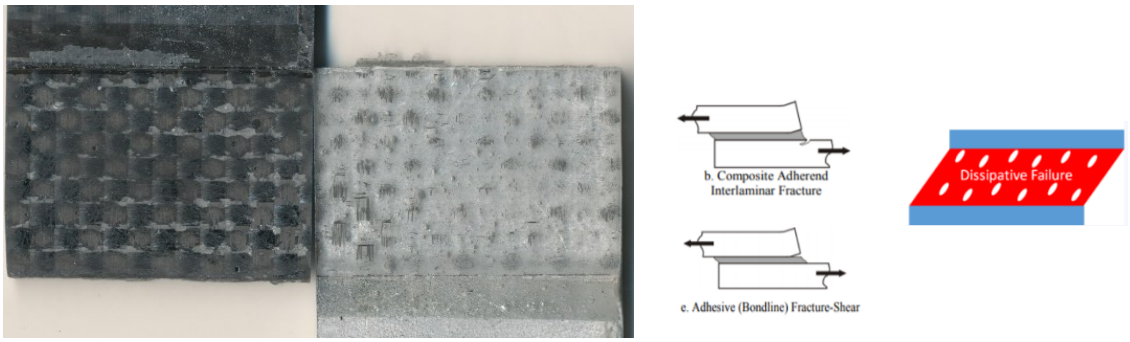


Figure 3. 97 Low magnification image after failure for Al-CFRP SLJ bonded with quick set epoxy tested subjected to a strain rate of 150 $s^{-1}$.

Figure 3.98 shows an optical microscopy image captured at 10 × magnification of Al-CFRP SLJ bonded with quick set epoxy tested under tensile loading conditions at a strain rate of 150 $s^{-1}$. Here, the aluminum substrate was investigated under microscope at 10 × magnification and the pore formation due to dissipative forces was spotted in the zoomed view.

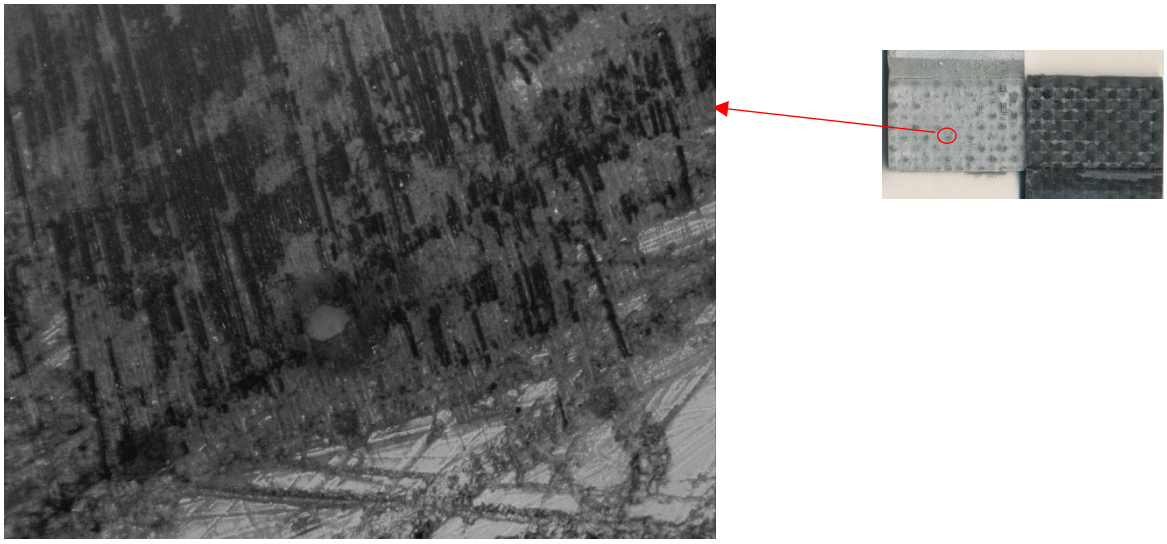

Figure 3.98 Optical microscopy image at 10 × magnification of Al-CFRP SLJ bonded with quick set epoxy subjected to a strain rate of 150 $s^{-1}$.

Figure 3.99 shows a DIC strain distribution map near to failure for Al-CFRP SLJ bonded with quick set epoxy tested under tensile loading conditions subjected to a strain rate of 150 $s^{-1}$. From the figure, the peak strain for the particular specimen was 0.116 % and there some amount of strain accumulated in the top portion and propogating towards the middle section which might have resulted in the shearing between composite adherend and epoxy adhesive.

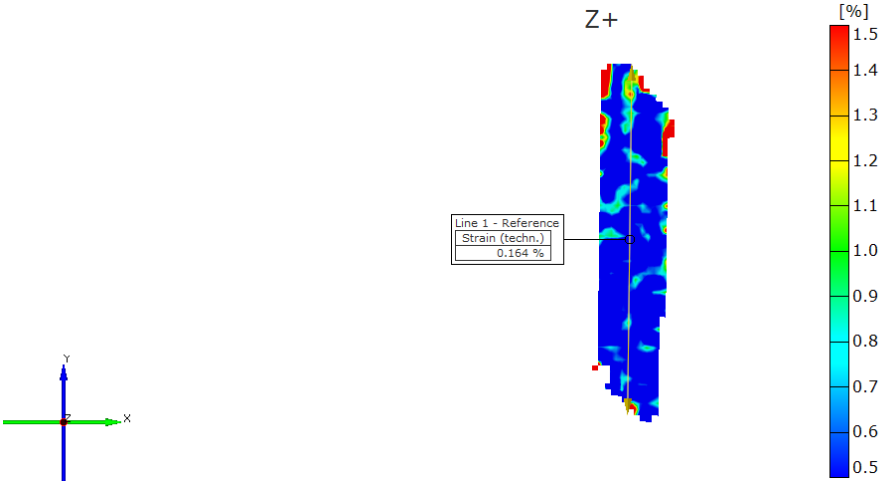


Figure 3.99 DIC strain distribution at failure for Al-CFRP SLJ bonded with quick set epoxy tested subjected to a strain rate of 150 $s^{-1}$.

### 3.2.2.3 Aluminum-composite with urethane-based adhesive

Figure 3.100 shows typical stress-strain curves of Al-CFRP SLJ bonded with urethane-based adhesive tested under tensile loading conditions at a strain rate of 15 $s^{-1}$. The lap joint was analyzed based on the lap shear strength and peak strain, and it can be observed that the lap joint exhibited an average shear strength of 14.4 MPa and an average peak strain of 0.55 %. The abnormalities in the graph are discussed previously as the settling of the specimen in the grips.

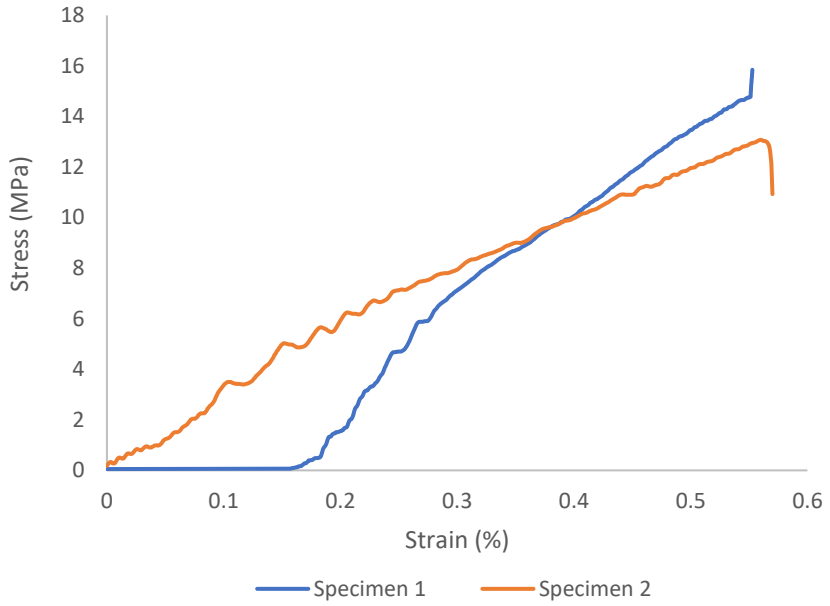


Figure 3.100 Typical stress vs strain behavior for Al-CFRP SLJ bonded with urethane-based adhesive tested a strain rate of 15 $s^{-1}$.

Figure 3.101 shows a low magnification optical microscopy image after the break for Al-CFRP SLJ bonded with urethane-based adhesive when tested under tensile loading conditions at a strain rate of 15 $s^{-1}$. From the figure, it was observed to be an interface failure between adhesive and aluminum adherend due to shear with some amount of residue leftover on the aluminum adherend.


Figure 3.101 Low magnification image after failure for Al-CFRP SLJ bonded with urethane-based adhesive subjected to a strain rate of 15 $s^{-1}$.

Figure 3.102 shows a DIC strain distribution map near to failure for Al-CFRP SLJ bonded with urethane-based adhesive tested under tensile loading conditions subjected to a strain rate of 15 $s^{-1}$. From the figure, the strain near failure for the particular specimen was 0.386 % and the strain distribution is observed to propogate from top and bottom region to the middle section and simultaneoulsy there is strain developed in region of adhesive bondline region as well.

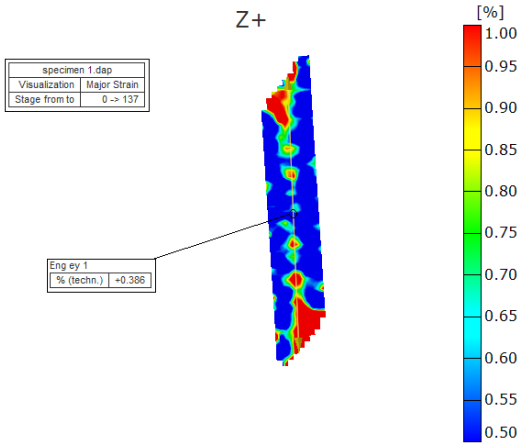


Figure 3.102 DIC strain distribution at failure for Al-CFRP SLJ bonded with urethane-based adhesive tested at a strain rate of 15 $s^{-1}$.

Figure 3.103 shows typical stress-strain curves of Al-CFRP SLJ bonded with urethane-based adhesive tested under tensile loading conditions at a strain rate of 15 $s^{-1}$. The lap joint was analyzed

based on the lap shear strength and peak strain, and it can be observed that the lap joint exhibited an average shear strength of 19.6 MPa and an average peak strain of 0.97 %.

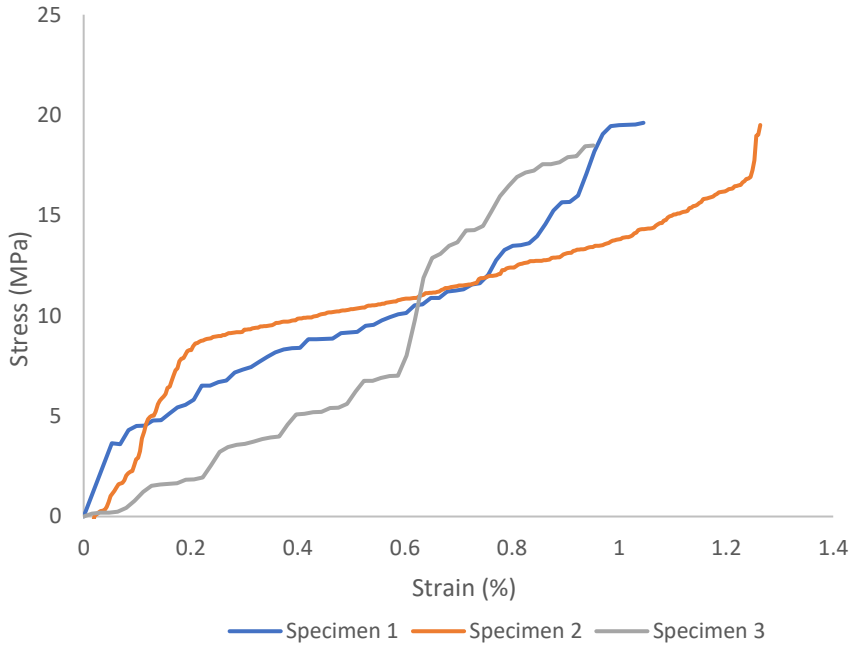


Figure 3.103 Typical stress vs strain behavior for Al-CFRP SLJ bonded with urethane adhesive subjected at a strain rate of 150 $s^{-1}$.

Figure 3.104 shows a low magnification optical microscopy image after the break for Al-CFRP SLJ bonded with urethane-based adhesive tested under tensile loading conditions at a strain rate of 150 $s^{-1}$. From the figure, it can be observed it is a mixed mode failure with interface failure between adhesive and both the substrate and yet again the adhesive was not able to withstand the crosshead speed and split into pieces. The adhesive failure from aluminum adherend can be concluded as a near interface failure mode due to the presence of a residue on the aluminum substrate.

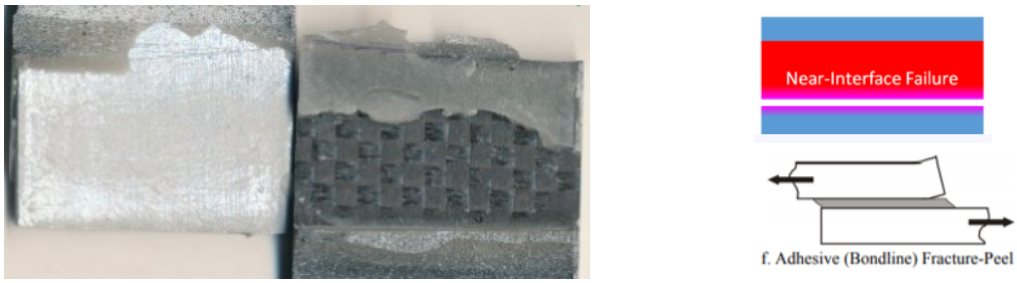


Figure 3.104 Low magnification image after failure for Al-Al SLJ bonded with urethane-based adhesive subjected to a strain rate of 150 $s^{-1}$.

Figure 3.105 shows the optical microscopy image captured at 10 × magnification of Al-CFRP SLJ bonded with urethane-based adhesive tested under tensile loading conditions at a strain rate of 150 $s^{-1}$. The CFRP adherend is observed under microscope to look at the shear behavior of adhesive from the aluminum substrate.

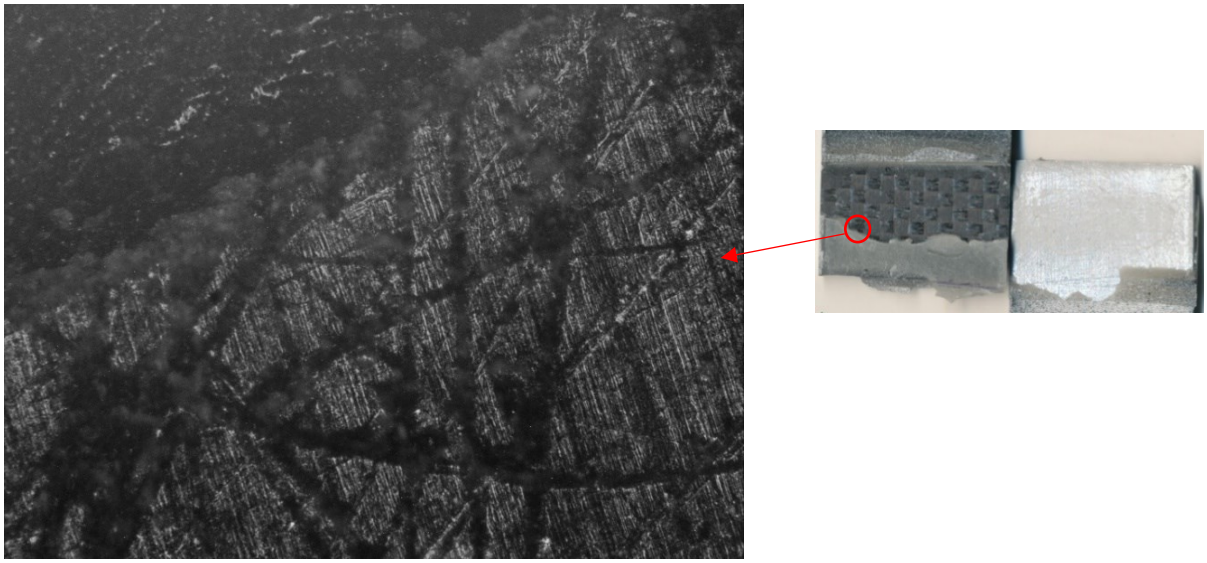

Figure 3.105 Optical microscopy image at 10 × magnification of Al-CFRP SLJ bonded with high strength epoxy tested at a strain rate of 150 $s^{-1}$.

Figure 3.106 shows a DIC strain distribution map near to failure for Al-CFRP SLJ bonded with urethane-based adhesive tested under tensile loading conditions subjected to a strain rate of 15 $s^{-1}$. From the figure, the peak strain for the particular specimen was 0.974 %, and the strain distribution is observed to propagate from top and bottom region to the middle section until failure, and when subjected to a higher strain rate of 150 $s^{-1}$, the strain distribution is more prominent and is propagating towards the adherends.

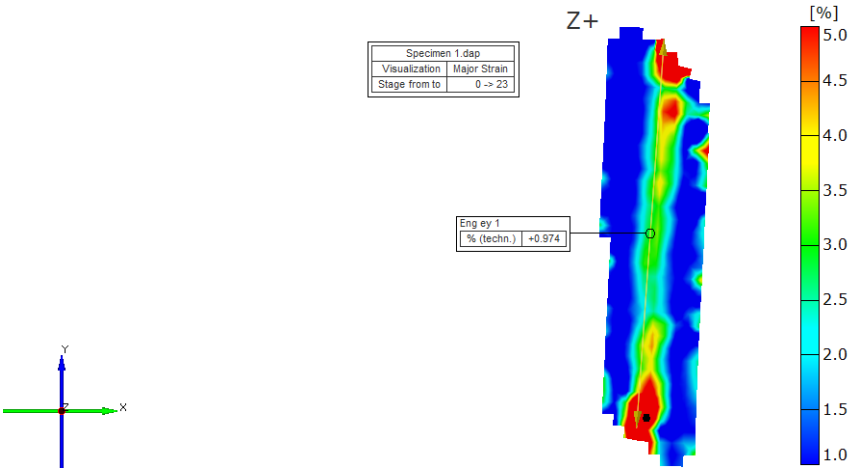


Figure 3.106 DIC strain distribution at failure for Al-CFRP SLJ bonded with urethane adhesive subjected to a strain rate of 150 $s^{-1}$.

### 3.2.3 Composite Joints

#### 3.2.3.1 CFRP-CFRP joints with high strength epoxy

Figure 3.107 shows typical stress-strain curves of CFRP-CFRP SLJ bonded with high strength epoxy tested under tensile loading conditions at a strain rate of 15 $s^{-1}$. The lap joint was analyzed based on the lap shear strength and peak strain, and it can be observed that the lap joint exhibited an average shear strength of 16.39 MPa and an average peak strain of 0.566 %. The serrations in the graph are probably due to load cell ringing in the test machine and can be ignored. The third specimen data was discarded as it prematurely broke during the beginning of the test.

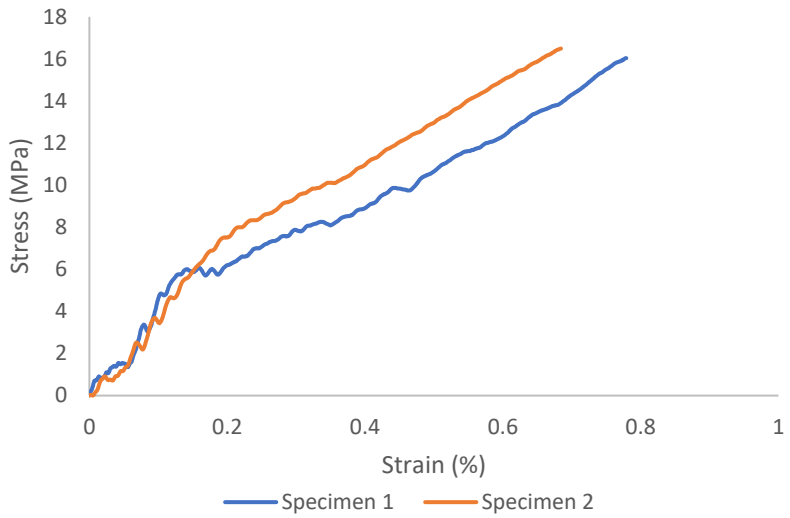


Figure 3.107 Typical stress vs. strain behavior for CFRP-CFRP SLJ bonded with high strength epoxy subjected to a strain rate of 15 $s^{-1}$.

Figure 3.108 shows a low magnification optical microscopy image after the break for CFRP-CFRP SLJ bonded with high strength epoxy tested under tensile loading conditions at a strain rate of 15 $s^{-1}$. From the figure, it can be observed that it is a mixed mode failure where maximum failure is due to composite adherend interlaminar fracture and some amount of adhesive failure due to shear. The high strength epoxy has a brittle nature which induce the crack formation in the composite adherend causing failure.

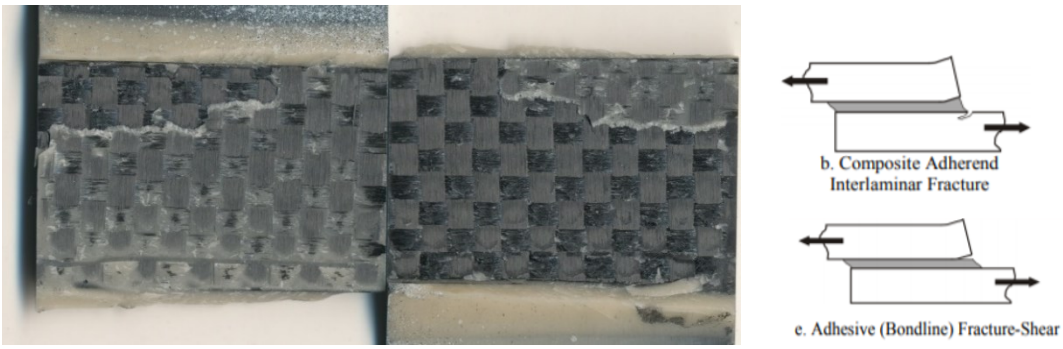


Figure 3.108 Low magnification image after failure for CFRP-CFRP SLJ bonded with high strength epoxy subjected to a strain rate of 15 $s^{-1}$.

Figure 3.109 shows the DIC strain distribution map near to failure for CFRP-CFRP SLJ bonded with high strength epoxy tested under tensile loading conditions subjected to a strain rate of 15 $s^{-1}$. From the figure, the peak strain for the particular specimen was 0.566 %, and the strain distribution is observed to accumulate in the top and bottom region and propagating to the composite adherends until failure. This behavior has resulted in the cohesive fracture in the substrate due to peeling.

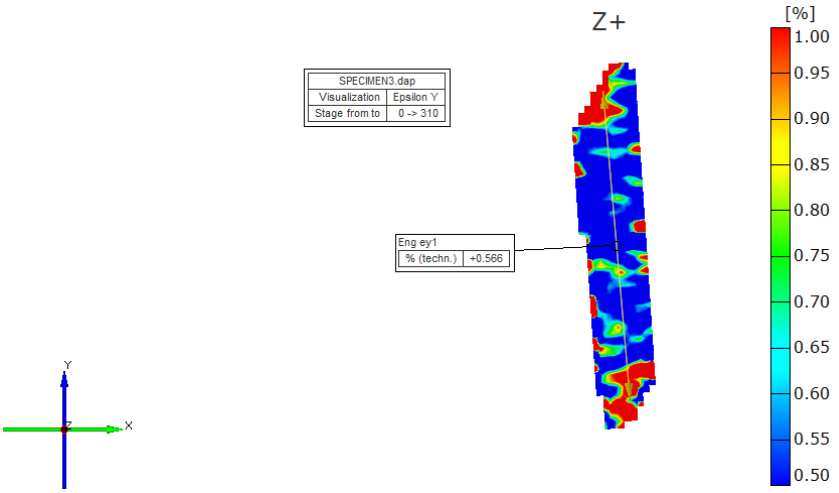


Figure 3.109 DIC strain distribution at failure for CFRP-CFRP SLJ bonded with high strength epoxy subjected to a strain rate of 15 $s^{-1}$.

Figure 3.110 shows typical stress-strain curves of CFRP-CFRP SLJ bonded with high strength epoxy tested under tensile loading conditions at a strain rate of 150 $s^{-1}$. The lap joint was analyzed based on the lap shear strength and peak strain, and it can be observed that the lap joint exhibited an average shear strength of 19.5 MPa and an average peak strain of 0.36 %. Due to vibrations present during the test, the high-speed digital images capture them and when analyzed in DIC typical deviations in the slope can be observed.

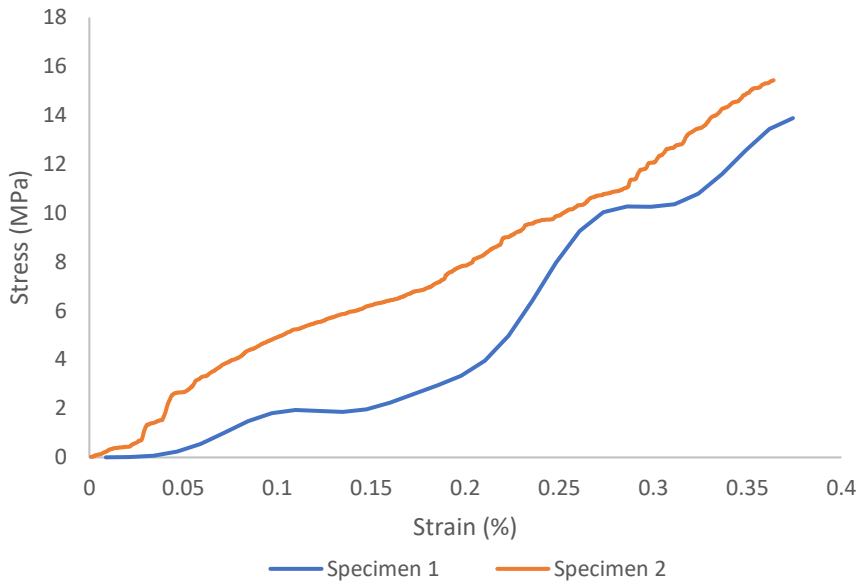


Figure 3.110 Typical stress vs. strain behavior for CFRP-CFRP SLJ bonded with high strength epoxy subjected to a strain rate of 150 $s^{-1}$.

Figure 3.111 shows a low magnification optical microscopy image after the break for CFRP-CFRP SLJ bonded with high strength epoxy tested under tensile loading conditions at a strain rate of 150 $s^{-1}$. From the figure, it can be observed that it is a mixed mode failure where failure is due to composite adherend interlaminar fracture and interfacial adhesive failure due to shear.

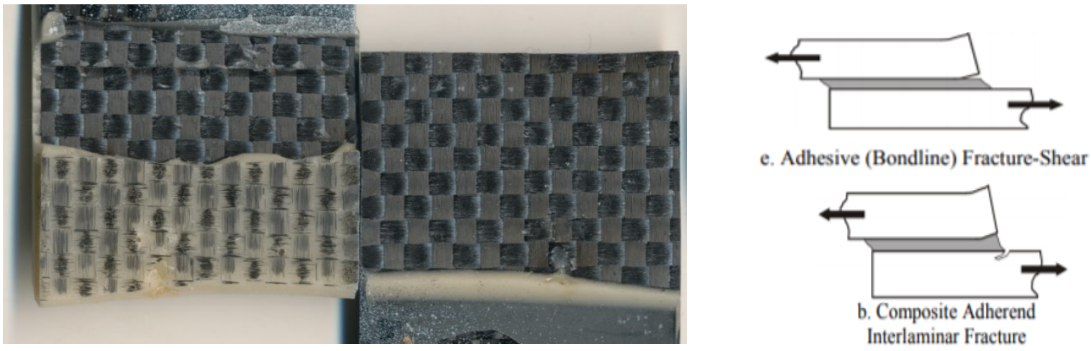


Figure 3.111 Low magnification image after failure for CFRP-CFRP SLJ bonded with high strength epoxy tested under tensile loading conditions subjected to a strain rate of 150 $s^{-1}$.

Figure 3.112 shows the optical microscopy image captured at 10 × magnification of CFRP-CFRP SLJ bonded with high strength epoxy tested under tensile loading conditions at a strain rate of 150

$s^{-1}$. It shows some uncured epoxy and some interlaminar failure occurring in the composite substrate.

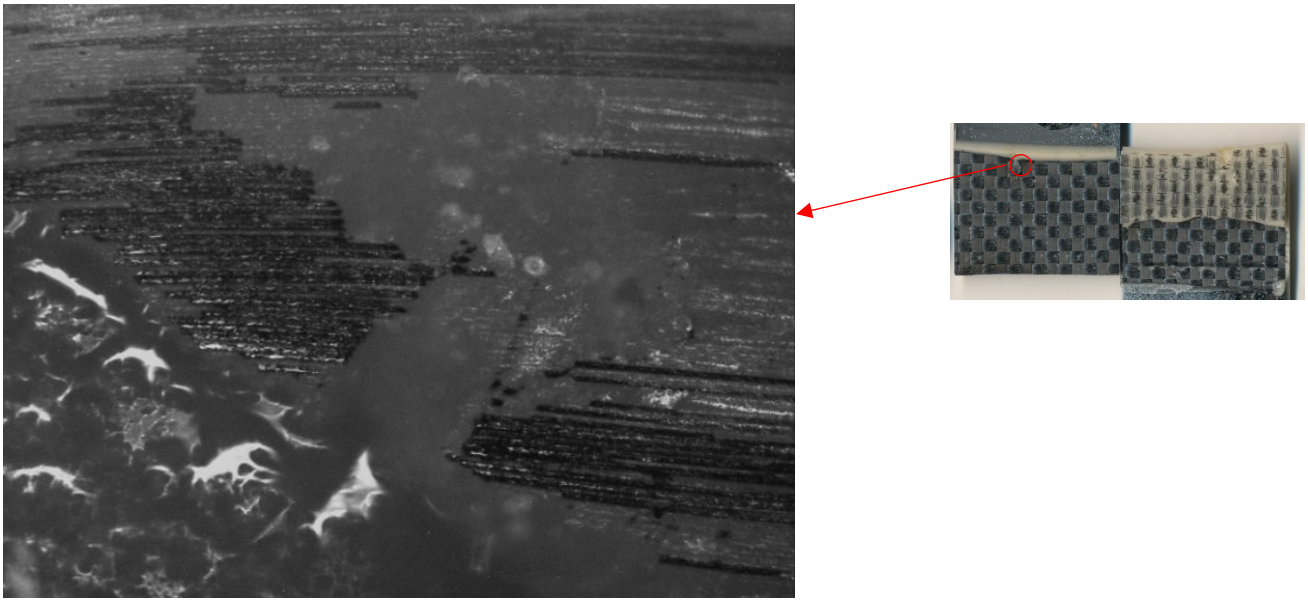

Figure 3.112 Optical microscopy image captured at 10 × magnification of CFRP-CFRP SLJ bonded with high strength epoxy tested at a strain rate of 150 $s^{-1}$.

Figure 3.113 shows a DIC strain distribution map near to failure for CFRP-CFRP SLJ bonded with high strength epoxy tested under tensile loading conditions to a strain rate of 150 $s^{-1}$. From the figure, the strain near to failure for the particular specimen was 0.186 %, and a large amount of strain is observed not be accumulated in the top region between adhesive and adherend which could have been the cause for composite interlaminar fracture due to peel.

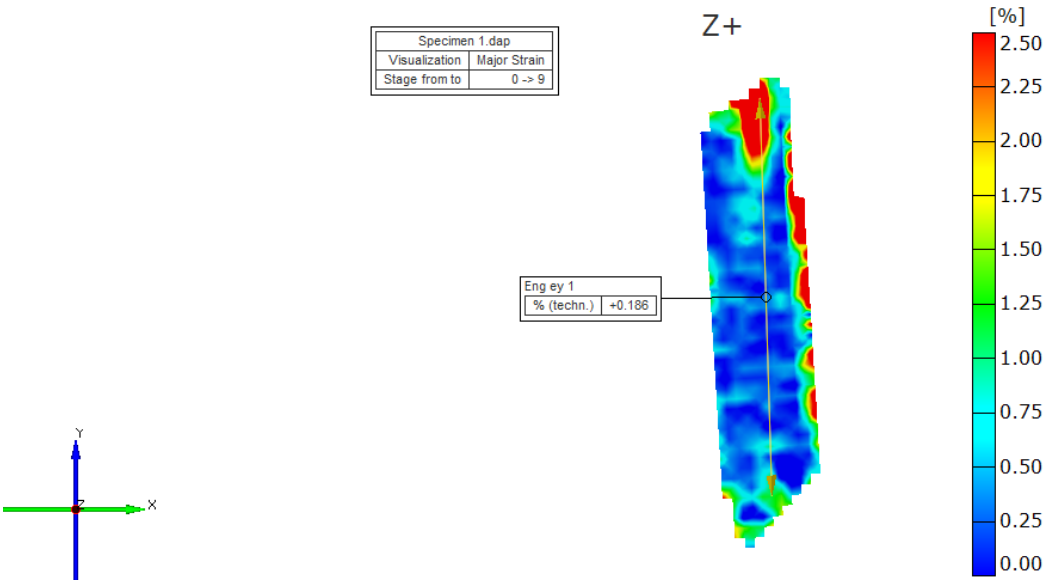


Figure 3.113 DIC strain distribution at failure for CFRP-CFRP SLJ bonded with high strength epoxy tested under tensile loading conditions subjected to a strain rate of 150 $s^{-1}$.

### 3.2.3.2 CFRP-CFRP joints with quick set epoxy

Figure 3.114 shows typical stress-strain curves of CFRP-CFRP SLJ bonded with quick set epoxy tested under tensile loading conditions at a strain rate of 15 $s^{-1}$. The lap joint was analyzed based on the lap shear strength and peak strain, and it can be observed that the lap joint exhibited an average shear strength of 18.31 MPa and an average peak strain of 0.47 %. The serrations in the graph are probably due to load cell ringing in the test machine and can be ignored. The dips in graphs due to load drop is when specimens are settling in the grips.

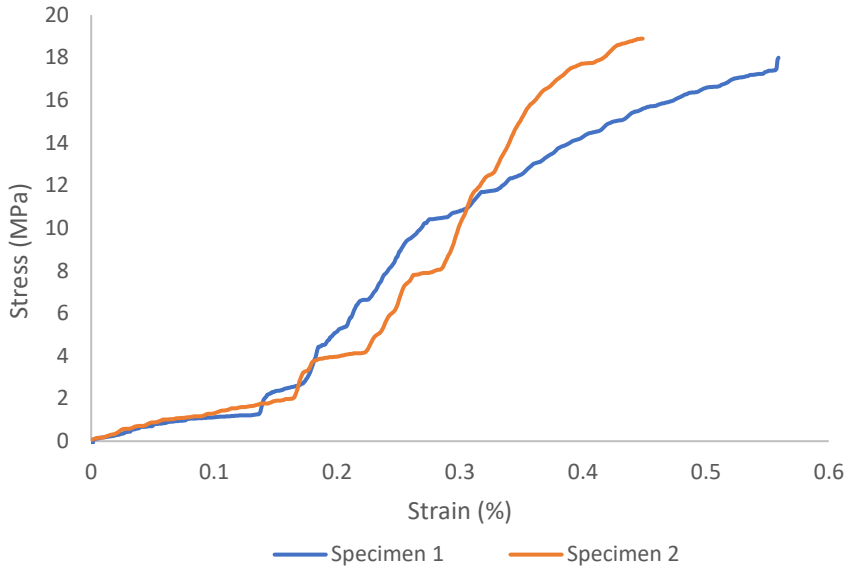


Figure 3.114 Typical stress vs. strain behavior for CFRP-CFRP SLJ bonded with quick set epoxy tested under tensile loading conditions at a strain rate of 15 $s^{-1}$.

Figure 3.115 shows a low magnification optical microscopy image after the break for CFRP-CFRP SLJ bonded with quick epoxy tested under tensile loading conditions at a strain rate of 15 $s^{-1}$. From the figure, it is evident that the failure mode in interfacial fracture between composite adherend and epoxy adhesive. There is no residue formation on the other substrate, but there are pores formed in the epoxy.

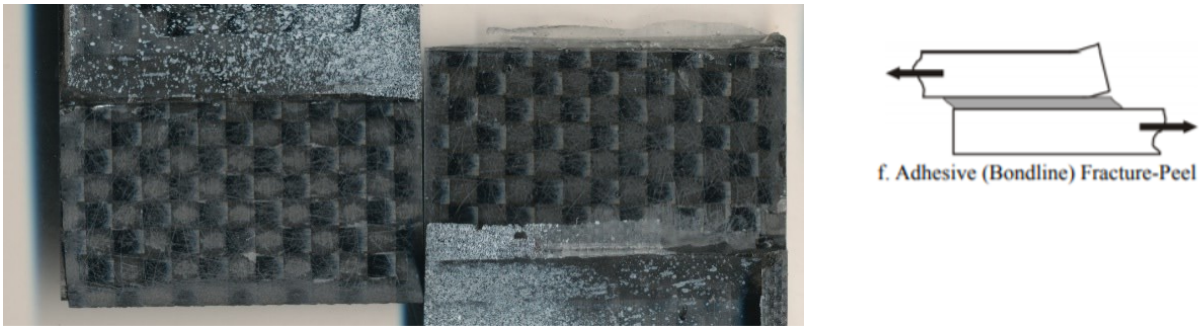


Figure 3.115 Low magnification image after failure for CFRP-CFRP SLJ bonded with quick set epoxy tested under tensile loading conditions subjected to a strain rate of 15 $s^{-1}$.

Figure 3.116 shows a DIC strain distribution map near to failure for CFRP-CFRP SLJ bonded with quick set epoxy tested under tensile loading conditions subjected to a strain rate of 15 $s^{-1}$. From the figure, the strain near to failure for the particular specimen was 0.473 %, and typical behavior of lap joints can be seen where the cracks are initiating from the top and bottom region and propagating to the middle section.

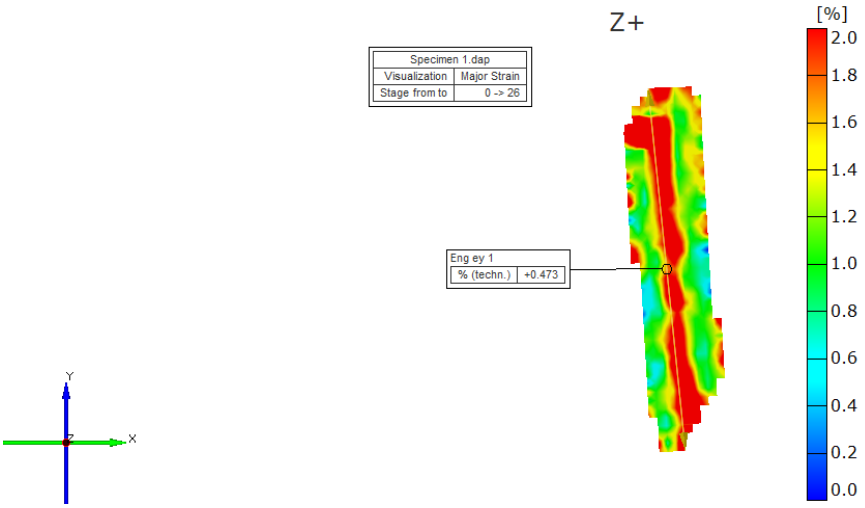


Figure 3.116 DIC strain distribution at failure for CFRP-CFRP SLJ bonded with quick set epoxy subjected to a strain rate of 15 $s^{-1}$.

Figure 3.117 shows typical stress-strain curves of CFRP-CFRP SLJ bonded with quick set epoxy tested under tensile loading conditions at a strain rate of 150 $s^{-1}$. The lap joint was analyzed based on the lap shear strength and peak strain, and it can be observed that the lap joint exhibited an average shear strength of 21.98 MPa and an average peak strain of 0.31 %. The serrations in the graph are probably due to load cell ringing in the test machine and can be ignored. The dips in graphs due to load drop is when specimens are settling in the grips.

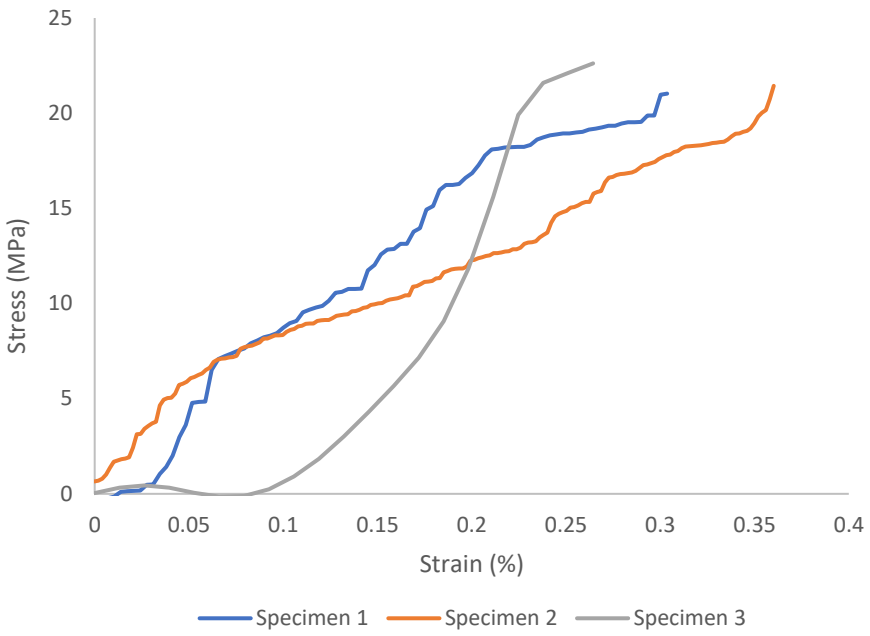


Figure 3.117 Typical stress vs. strain behavior for CFRP-CFRP SLJ bonded with quick set epoxy tested at a strain rate of 150 $s^{-1}$.

Figure 3.118 shows a low magnification optical microscopy image after the break for CFRP-CFRP SLJ bonded with quick epoxy tested under tensile loading conditions at a strain rate of 150 $s^{-1}$. From the figure, it is evident that the failure mode is an interfacial fracture between composite adherend and epoxy adhesive and cohesive failure in adhesive which is very rare failure mode with this adhesive.

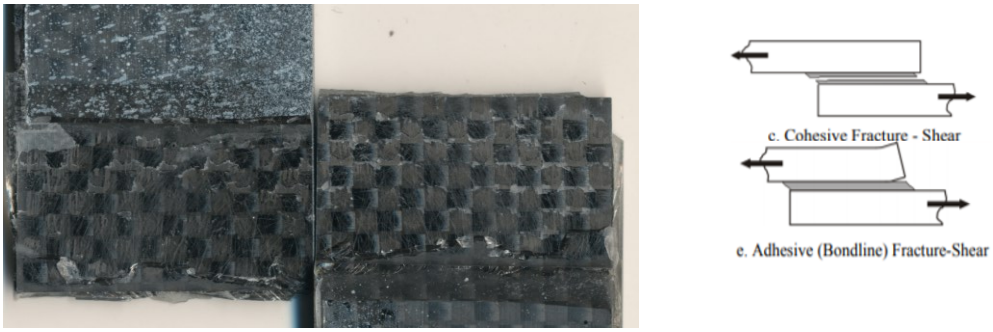


Figure 3.118 Low magnification image after failure for CFRP-CFRP SLJ bonded with quick set epoxy subjected to a strain rate of 150 $s^{-1}$.

Figure 3.119 shows an optical microscopy image captured at 10 × magnification of CFRP-CFRP SLJ bonded with high strength epoxy tested under tensile loading conditions at a strain rate of 150 $s^{-1}$. Here, it was observed that the epoxy showed a shear behavior which is usually observed in lower strain rates in other adhesives.

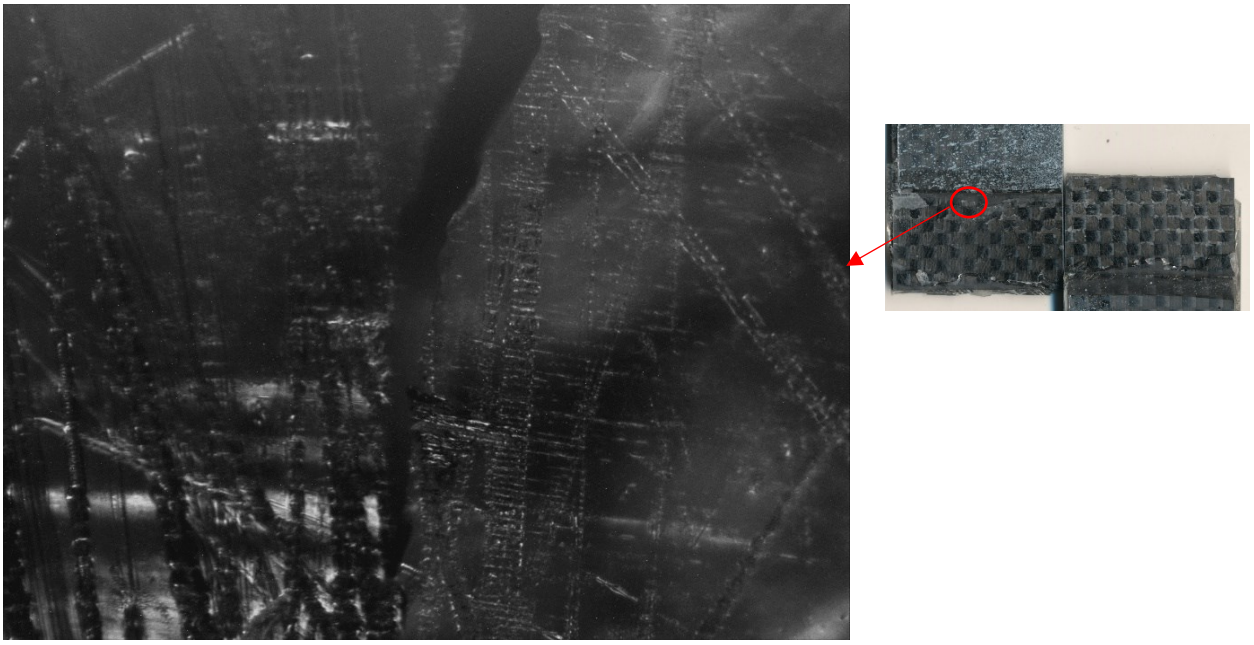

Figure 3.119 Optical microscopy image at 10 × magnification of CFRP-CFRP SLJ bonded with quick set epoxy subjected to a strain rate of 150 $s^{-1}$.

Figure 3.120 shows a DIC strain distribution map near to failure for CFRP-CFRP SLJ bonded with quick set epoxy tested under tensile loading conditions subjected to a strain rate of 150 $s^{-1}$. From the figure, the strain near to failure for the particular specimen was 0.47 %, and the strain is distributed all over the lap joint but very prominent in the adhesive bondline region which caused the failure.

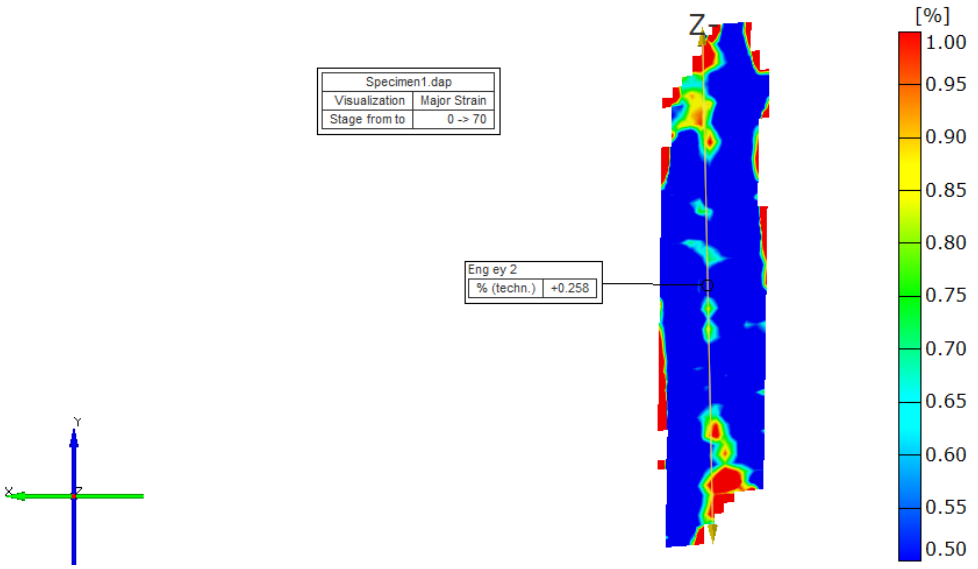


Figure 3.120 DIC strain distribution at failure for CFRP-CFRP SLJ bonded with quick set epoxy subjected to a strain rate of 150 $s^{-1}$.

### 3.2.3.3 CFRP-CFRP joints with urethane-based adhesive

Figure 3.121 shows typical stress-strain curves of CFRP-CFRP SLJ bonded with urethane-based adhesive tested under tensile loading conditions at a strain rate of 15 $s^{-1}$. The lap joint was analyzed based on the lap shear strength and peak strain, and it can be observed that the lap joint exhibited an average shear strength of 22.15 MPa and an average peak strain of 1.28 %. The non-linearity in the graph can be explained by the shifting of the load bearing capacity from the substrate end to adhesive bondline. The first part of the graph could be the tensile behavior of carbon fiber substrate and after the shift in the curve it could have been the ductile behavior of urethane adhesive.

Figure 3.122 shows a low magnification optical microscopy image after the break for CFRP-CFRP SLJ bonded with quick epoxy tested under tensile loading conditions at a strain rate of 150 $s^{-1}$. From the figure, it can be obserevd that it is a mixed mode failure with composite interlaminar fracture and some amount of an interfacial fracture between composite adherend and urthane adhesive. There is even some amount of fiber tear visible. This mode is clearly evident in the higher strain of similar combination.

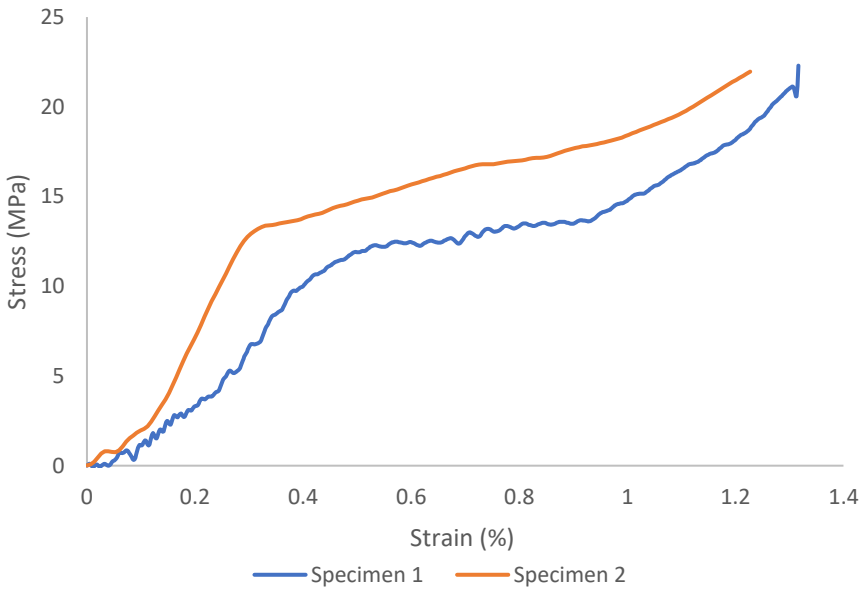


Figure 3.121 Typical stress vs strain behavior for CFRP-CFRP SLJ bonded with urethane-based adhesive tested under tensile loading conditions at a strain rate of 15 $s^{-1}$.

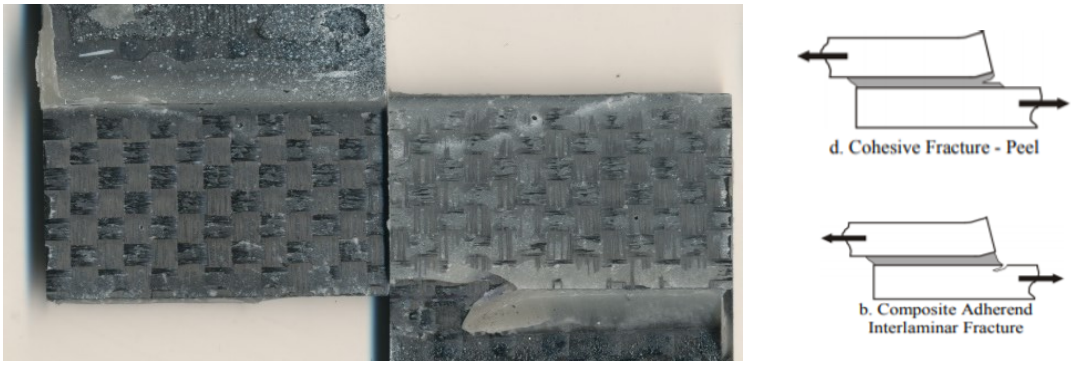


Figure 3.122 Low magnification image after failure for CFRP-CFRP SLJ bonded with urethane-based adhesive subjected to a strain rate of 15 $s^{-1}$.

Figure 3.123 shows a DIC strain distribution map near to failure for CFRP-CFRP SLJ bonded with urethane-based adhesive tested under tensile loading conditions subjected to a strain rate of 15 $s^{-1}$. From the figure, the strain near to failure for the particular specimen was 0.989 %, and the strain is distributed all over the lap joint but very prominent in the adhesive bondline region which caused the failure.

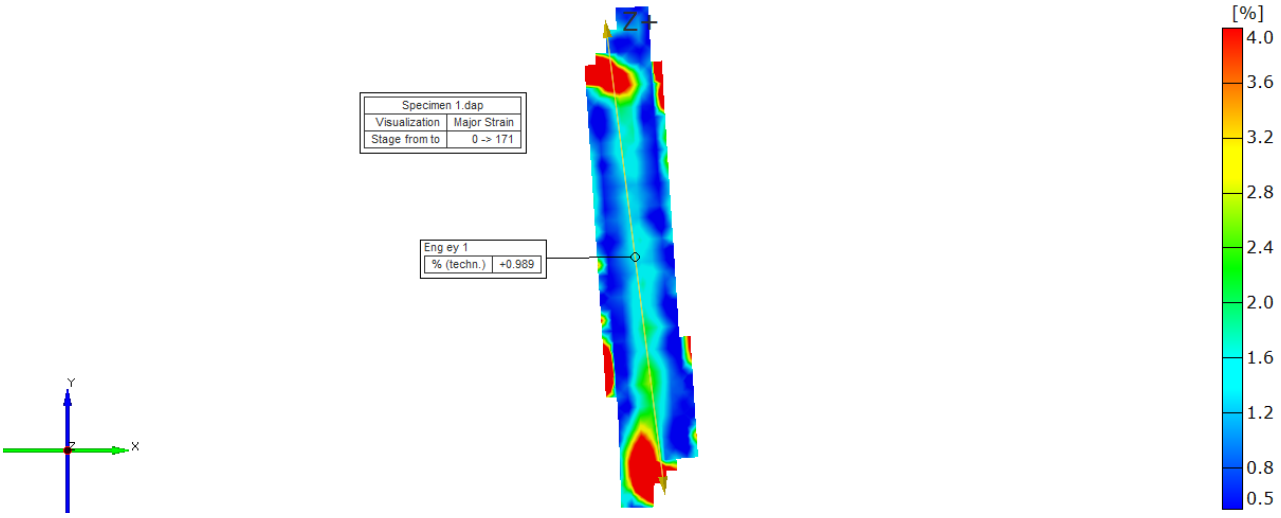


Figure 3.123 DIC strain distribution at failure for CFRP-CFRP SLJ bonded with urethane-based adhesive subjected to a strain rate of 15 $s^{-1}$.

Figure 3.124 shows typical stress-strain curves of CFRP-CFRP SLJ bonded with urethane-based adhesive tested under tensile loading conditions at a strain rate of 150 $s^{-1}$. The lap joint was analyzed based on the lap shear strength and peak strain, and it can be observed that the lap joint exhibited an average shear strength of 26.89 MPa and an average peak strain of 0.64 %. The stress strain graph is mainly exhibiting the tensile behavior of composite substrate rather than the shear behavior of adhesive as the shear strength of urethane-based adhesive seems to be higher than tensile strength of the substrate.

Figure 3.125 shows a low magnification optical microscopy image after the break for CFRP-CFRP SLJ bonded with urethane-based adhesive tested under tensile loading conditions at a strain rate of 150 $s^{-1}$. From the figure, it can be evidently stated that the failure was due to fiber tear and fiber pull out in composite adherend in one portion of bond area and other portion shows a mixed mode failure in form of composite interlaminar fracture with debonding from fibers and some amount of cohesive failure in adhesive.

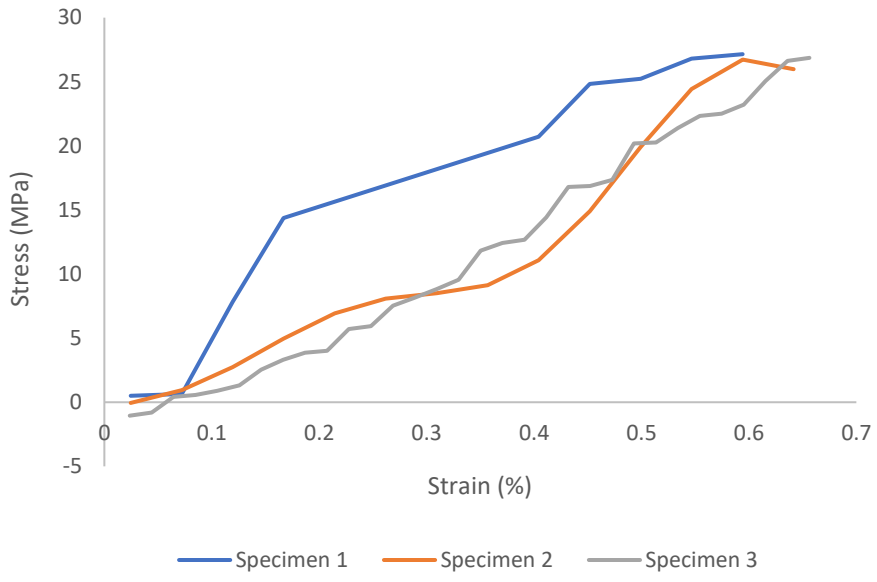


Figure 3.124 Typical stress vs strain behavior for CFRP-CFRP SLJ bonded with urethane-based adhesive subjected to a strain rate of 150 $s^{-1}$.

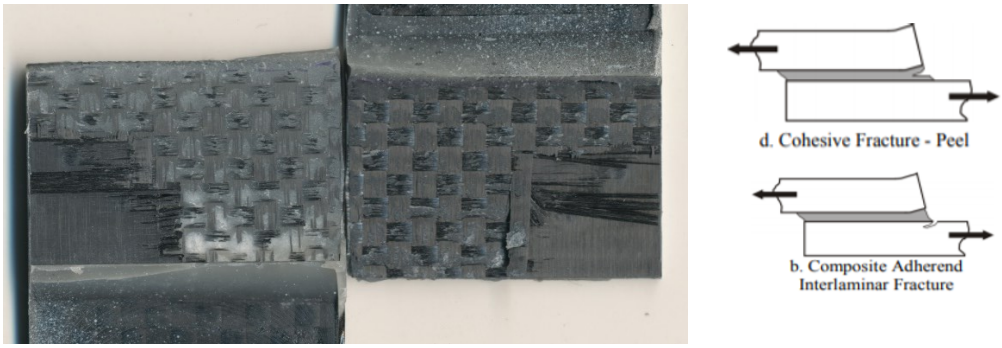


Figure 3.125 Low magnification image after failure for CFRP-CFRP SLJ bonded with urethane-based adhesive subjected to a strain rate of 150 $s^{-1}$.

Figure 3.126 shows an optical microscopy image captured at 10 × magnification of CFRP-CFRP SLJ bonded with urethane-based adhesive tested under tensile loading conditions at a strain rate of 150 $s^{-1}$. Since, the fracture was mostly due to interlaminar fiber breakage in composite. It was more clearly observed under optical microscope to understand the type of failure mode in the composite and it appears to debonding (matrix failure).

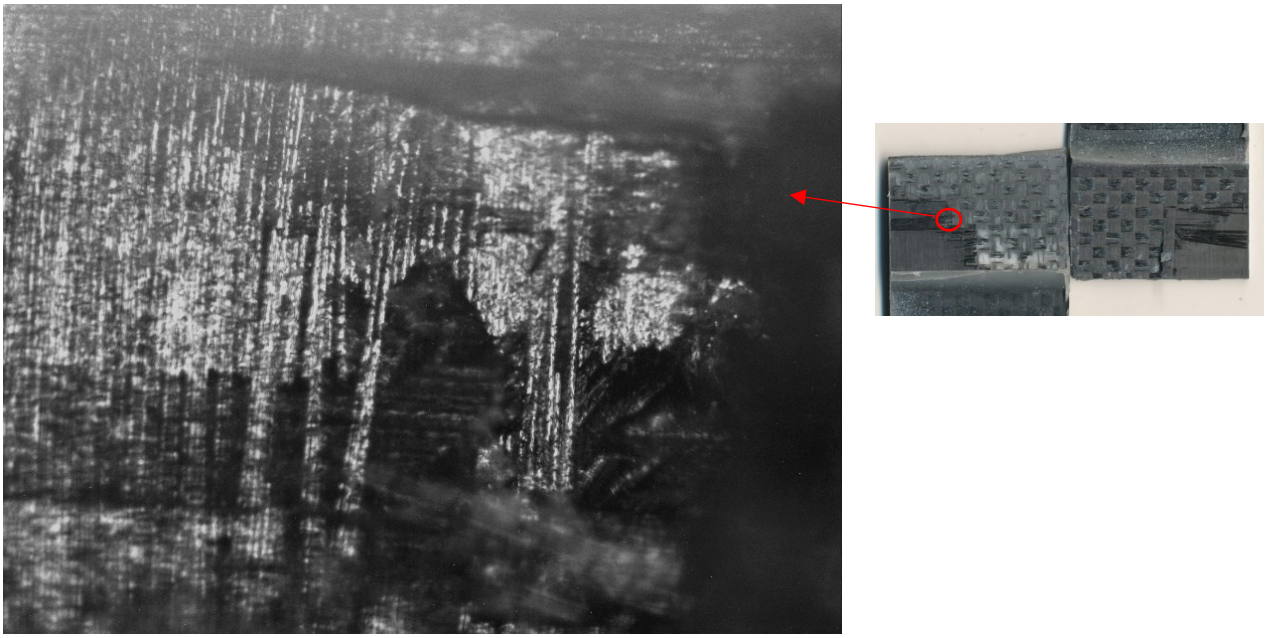

Figure 3.126 Optical microscopy image at 10 × magnification of CFRP-CFRP SLJ bonded with urethane-based adhesive subjected to a strain rate of 150 $s^{-1}$.

Figure 3.127 shows a DIC strain distribution map near to failure for CFRP-CFRP SLJ bonded with urethane-based adhesive tested under tensile loading conditions subjected to a strain rate of 150 $s^{-1}$. From the figure, the strain near to failure for the particular specimen was 0.495 %, and the strain accumulation is evident in the adherend and adhesive of bottom section which is area where fiber pull out was observed.

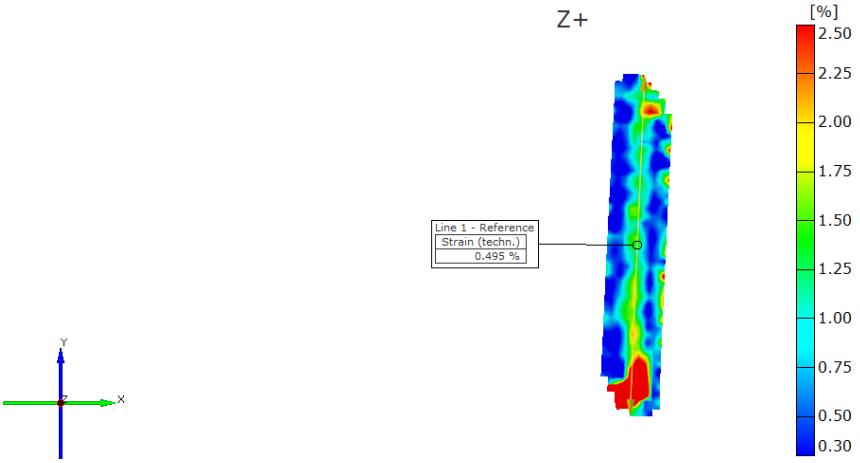


Figure 3.127 DIC strain distribution at failure for CFRP-CFRP SLJ bonded with urethane-based adhesive subjected to a strain rate of 150 $s^{-1}$.

### 3.3 Summary

In this research project, a combination of nine SLJs were studied under tensile loading conditions subjected to strain rates (0.0015 $s^{-1}$, 0.15 $s^{-1}$, 15 $s^{-1}$, 150 $s^{-1}$). Results presented in this chapter included lap shear strength, peak load, maximum strain before failure, failure modes and optical microscopy analysis. A summary of results is presented to show a comparative analysis between different adhesives and different combinations.

Figure 3.128 shows maximum principal strain as a function of the applied load for AL- AL single lap joint with urethane-based adhesive at a strain rate of 0.0015 s-1. From the figure, it is clear how as the longitudinal strain increase, so is the concentration of the shear strain towards the central region of the adhesive. It is also evident that the maximum values of strain are always located towards the edges of the bond region. Such strain concentrations were also evident in the rest of the SLJ system investigated in this project.

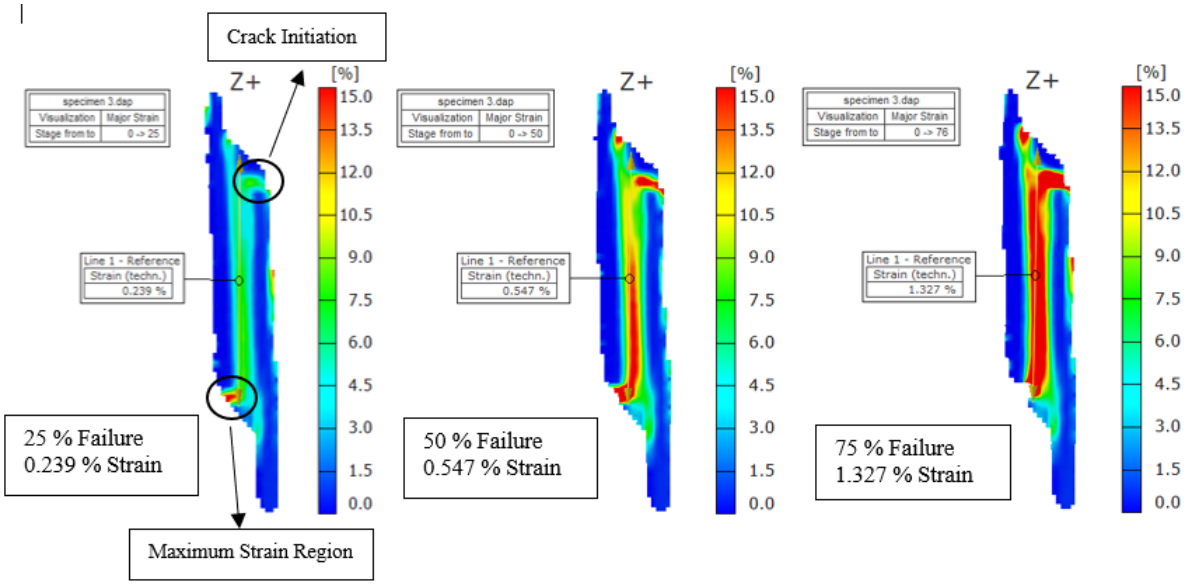


Figure 3.128 Principal strain along the bondline as the function of load level for Al - Al single lap joint with urethane-based adhesive at a strain rate of 0.0015 $s^{-1}$.

Figure 3.129 shows a variation of major strain along the overlap region for Al-CFRP with urethane based adhesive joint at a strain rate of 0.0015 $s^{-1}$. The figure highlights the importance of measuring the strain distribution along and across the bond region. Here, it is evident that the strains reach a lower value close to the substrates and higher values towards the center of the bond thickness. Moreover, from the graph, it is evident that the major strain is maximum in the Peel region of the adhesive and adherend and gradually decreases towards the middle of the bondline.

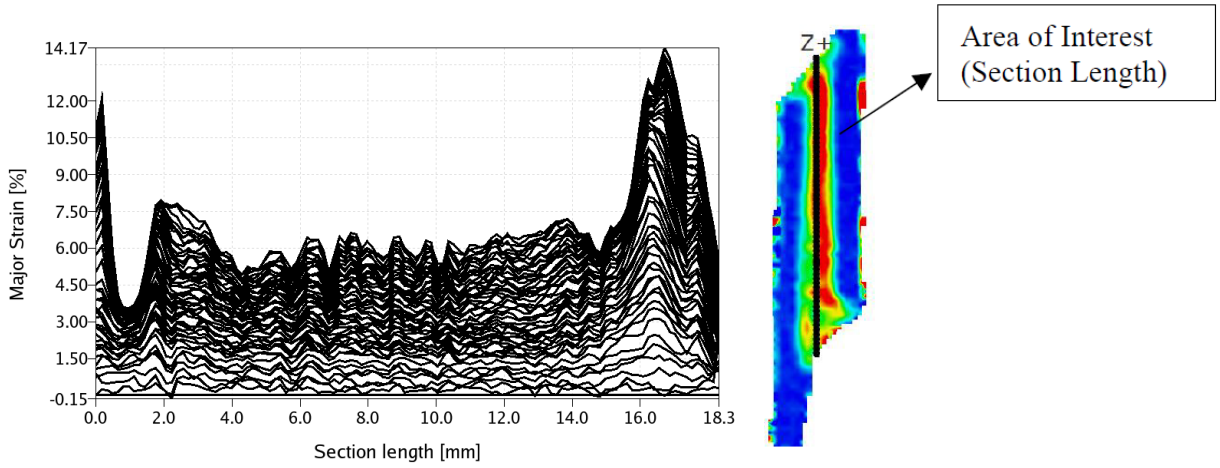


Figure 3.129 Variation of major strain along the overlap region (x/L) in the bondline from DIC.

Table 3.1 shows summary of results for all the SLJs considered in this project. The table includes average peak load, lap shear strength, average peak strain and failure modes differentiated in cohesive failure adhesive and substrate and, interfacial failure between adhesive and adherend. The failure modes were focused on the adhesive failure, cohesive failure in adhesive and, cohesive failure in substrate.

It can be seen that in the case of dissimilar adherend combination, the quick-setting epoxy exhibited higher strength than high strength epoxy in low strain rates, unlike other cases. This behavior can be due to the difference in CTE of metal and composite, the layers are building up temperature change, and these stresses need to be equal to zero in the unloaded state. In the case of metal-metal bonding, the residual thermal stresses are small and can be neglected [78]. However, due to dissimilar adherends such as Al/CFRP, these strains need to be considered in any prediction of in-service joint behavior.

To understand these stresses, Hausmann developed an equation to estimate the residual thermal stresses in composite and metal after curing the fiber-metal composite [79]. This equation can be used in this case to understand the residual thermal stresses induced in the lap joint when bonded with high strength epoxy which was cured at a temperature of 140 ˚F for 45 min.
The equation to estimate the residual thermal stresses of metal fraction $\sigma_m$:

$$\sigma_M = \frac{\Delta T(\alpha_C - \alpha_M)}{\frac{1}{E_C}\cdot\frac{1-vC}{v_C} + \frac{1}{E_M}} \quad (1)$$

$$\sigma_C = -\frac{1-vC}{v_C}\cdot\sigma_M \quad (2)$$

Where ΔT is the temperature difference between curing temperature and room temperature,

$\alpha_c$ and $\alpha_m$ are the CTE of composite and metal, respectively. $E_c$ and $E_m$ are the Young's Modulus of composite and metal, respectively. $V_c$ is the volume fraction of the composite layers about the overall thickness of the laminate. Table 3.1 Typical values for CFRP and Aluminum 6061 – T6 obtained from the manufacturer to calculate the thermal residual stresses.

Table 3. 1 Properties of CFRP and Aluminum 6061 – T6 to understand thermal residual stresses.

| Vc (%) | Vm (%) | Ec (GPa) | Em (GPa) | αc (℃−1) | αm (℃−1) |
|---|---|---|---|---|---|
| 53.55 | 46.45 | 121.5 | 68.9 | 0 × 10-6 | 23 × 10-6 |

From the above equation (1) and (2), the residual thermal stress of the composite in the 0˚ direction was found to be 35.42 MPa ($\sigma_c$). These residual thermal stresses can cause defects of micro-cracks in the fiber-matrix interface. This delamination are formed as the thermo-residual stress was higher than the interfacial strength and these stresses will expand the resin and form cracks [80].

Figure 3.130 shows typical stress vs strain graphs for the single lap joints at a strain rate 0.0015 s-1 for selected test coupons. It is clearly evident from the graphs that urethane-based adhesive can withstand more strain than other adhesives irrespective of the combination. For lower strain rate, the high strength epoxy had higher shear strength than quick set epoxy. Figure 3.131 shows typical stress vs strain graphs for the single lap joints at a strain rate 0.15 s-1. In case of Al-CFRP joints, there was decrease in the shear strength for high strength epoxy compared to quick set epoxy. The composite joints had maximum shear strengths compared to other combinations followed by Al-CFRP joints and then Aluminum joints. It can be observed that as the yield strength of the combination increases, the lap shear strength increases. Figure 3.132 shows typical stress vs strain graphs for the single lap joints at a strain rate 15 s-1. Figure 3.133 shows typical stress vs strain graphs for the single lap joints at a strain rate 150 s-1. In case of dynamic loading, the quick set epoxy exhibited higher strength values compared to high strength epoxy.

Table 3.2 Summary of results for all the SLJs considered in this project.

| Substrates | Adhesive Type | Strain rate | Max. load | Peak Stress | Peak Strain | Failure mode (Approx. %) | | | Typical Deviation |
|---|---|---|---|---|---|---|---|---|---|
| | | $s^{-1}$ | N | MPa | % | Interfacial | Coh (adh) | Coh (Sub) | MPa |
| Al-Al | High strength epoxy | 0.0015 | 2432 | 6.17 | 0.122 | 100 | 0 | 0 | 1.29 |
| | | 0.15 | 3363 | 8.54 | 0.141 | 100 | 0 | 0 | 0.95 |
| | | 15 | 3777 | 9.6 | 0.161 | 95 | 5 | 0 | 1.22 |
| | | 150 | 4407 | 11.2 | 0.167 | 95 | 5 | 0 | 0.47 |
| | Quick set epoxy | 0.0015 | 979 | 2.487 | 0.92 | 100 | 0 | 0 | 0.24 |
| | | 0.15 | 2359 | 5.99 | 0.66 | 80 | 20 | 0 | 0.6 |
| | | 15 | 2904 | 7.38 | 0.185 | 100 | 0 | 0 | 0.76 |
| | | 150 | 5863 | 14.9 | 0.115 | 90 | 10 | 0 | 2.07 |
| | Urethane adhesive | 0.0015 | 1188 | 3.01 | 2.8 | 80 | 20 | 0 | 0.3 |
| | | 0.15 | 4460 | 11.34 | 3.32 | 40 | 60 | 0 | 1.1 |
| | | 15 | 6800 | 17.27 | 1.43 | 80 | 20 | 0 | 0.38 |
| | | 150 | 7733 | 19.65 | 1.09 | 100 | 0 | 0 | 1.45 |
| Al-CFRP | High strength epoxy | 0.0015 | 1946 | 4.94 | 0.216 | 95 | 5 | 0 | 1.07 |
| | | 0.15 | 2279.3 | 5.79 | 0.154 | 90 | 0 | 10 | 1.98 |
| | | 15 | 4364 | 12.5 | 0.116 | 80 | 5 | 15 | 0.89 |
| | | 150 | 6500 | 16.51 | 0.045 | 90 | 0 | 10 | 0.43 |
| | Quick set epoxy | 0.0015 | 1685.5 | 4.28 | 0.6 | 100 | 0 | 0 | 1.27 |
| | | 0.15 | 3021.3 | 7.67 | 0.49 | 90 | 0 | 10 | 1.23 |
| | | 15 | 4621 | 11.74 | 0.41 | 80 | 5 | 15 | 1.47 |
| | | 150 | 7293 | 18.53 | 0.38 | 90 | 0 | 10 | 2.93 |
| | Urethane adhesive | 0.0015 | 2667 | 6.77 | 1.31 | 95 | 5 | 0 | 1.58 |
| | | 0.15 | 5115.3 | 12.99 | 1.34 | 0 | 100 | 0 | 1.35 |
| | | 15 | 5674 | 14.4 | 0.55 | 100 | 0 | 0 | 2.9 |
| | | 150 | 7720 | 19.6 | 0.97 | 80 | 10 | 10 | 1.57 |
| CFRP - CFRP | High strength epoxy | 0.0015 | 4638.3 | 11.78 | 0.35 | 30 | 0 | 70 | 1.52 |
| | | 0.15 | 5076 | 12.9 | 0.21 | 30 | 10 | 60 | 1.06 |
| | | 15 | 6453 | 16.39 | 0.56 | 15 | 0 | 85 | 0.3 |
| | | 150 | 7690 | 19.5 | 0.36 | 30 | 5 | 65 | 0.95 |
| | Quick set epoxy | 0.0015 | 3752.5 | 9.53 | 1.84 | 60 | 40 | 0 | 0.3 |
| | | 0.15 | 5342.6 | 13.57 | 0.84 | 90 | 10 | 0 | 1.9 |
| | | 15 | 7207 | 18.03 | 0.47 | 100 | 0 | 0 | 5.92 |
| | | 150 | 8653 | 21.98 | 0.31 | 90 | 10 | 0 | 0.13 |
| | Urethane adhesive | 0.0015 | 6828.5 | 17.35 | 2.8 | 15 | 80 | 5 | 1.52 |
| | | 0.15 | 8737.3 | 22.2 | 2.61 | 0 | 3 | 97 | 2.79 |
| | | 15 | 8716 | 22.15 | 1.28 | 25 | 0 | 75 | 0.85 |
| | | 150 | 10583 | 26.89 | 0.64 | 5 | 5 | 90 | 2.85 |

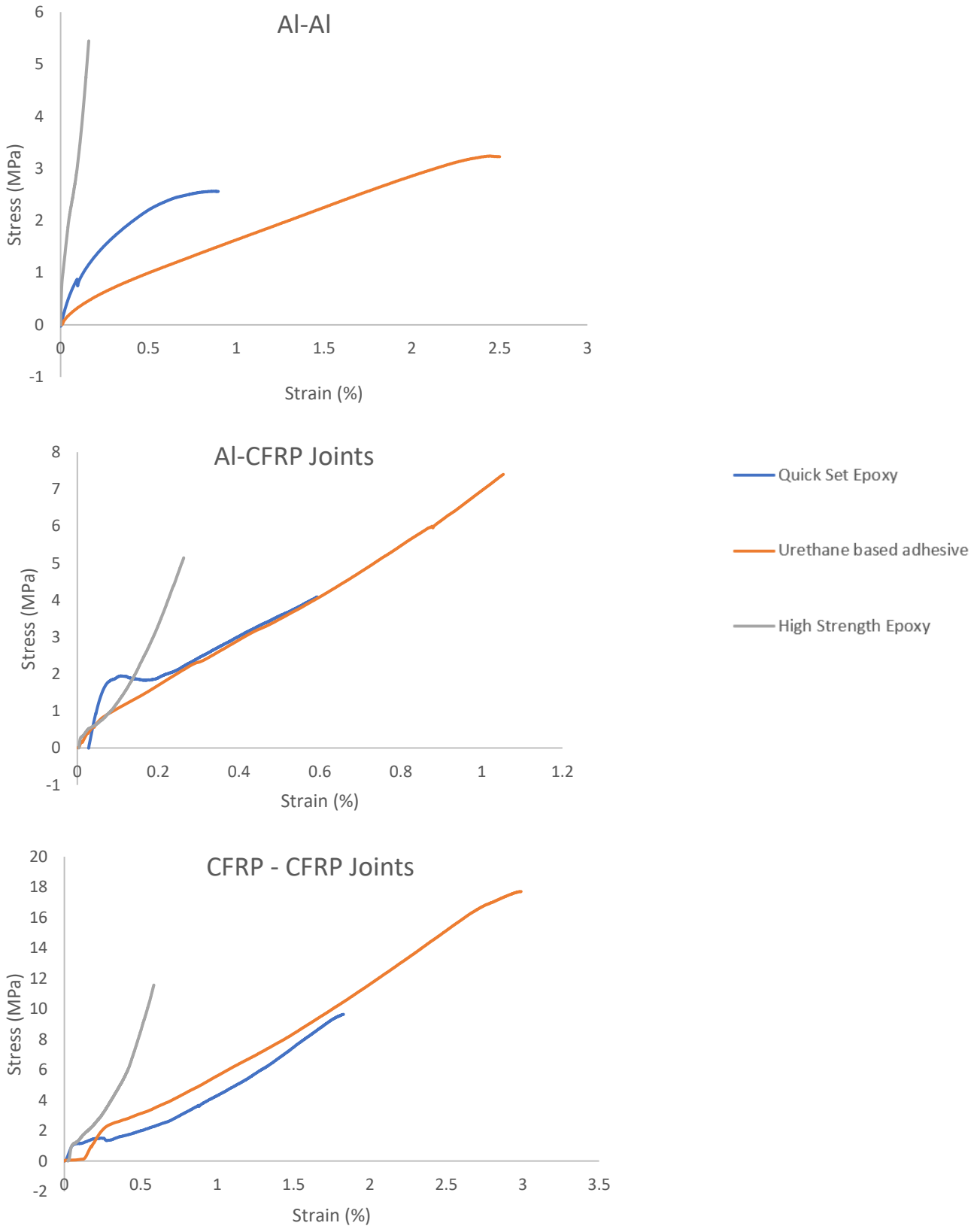


Figure 3.130 Typical stress vs strain graphs for the single lap joints at a strain rate 0.0015 $s^{-1}$.

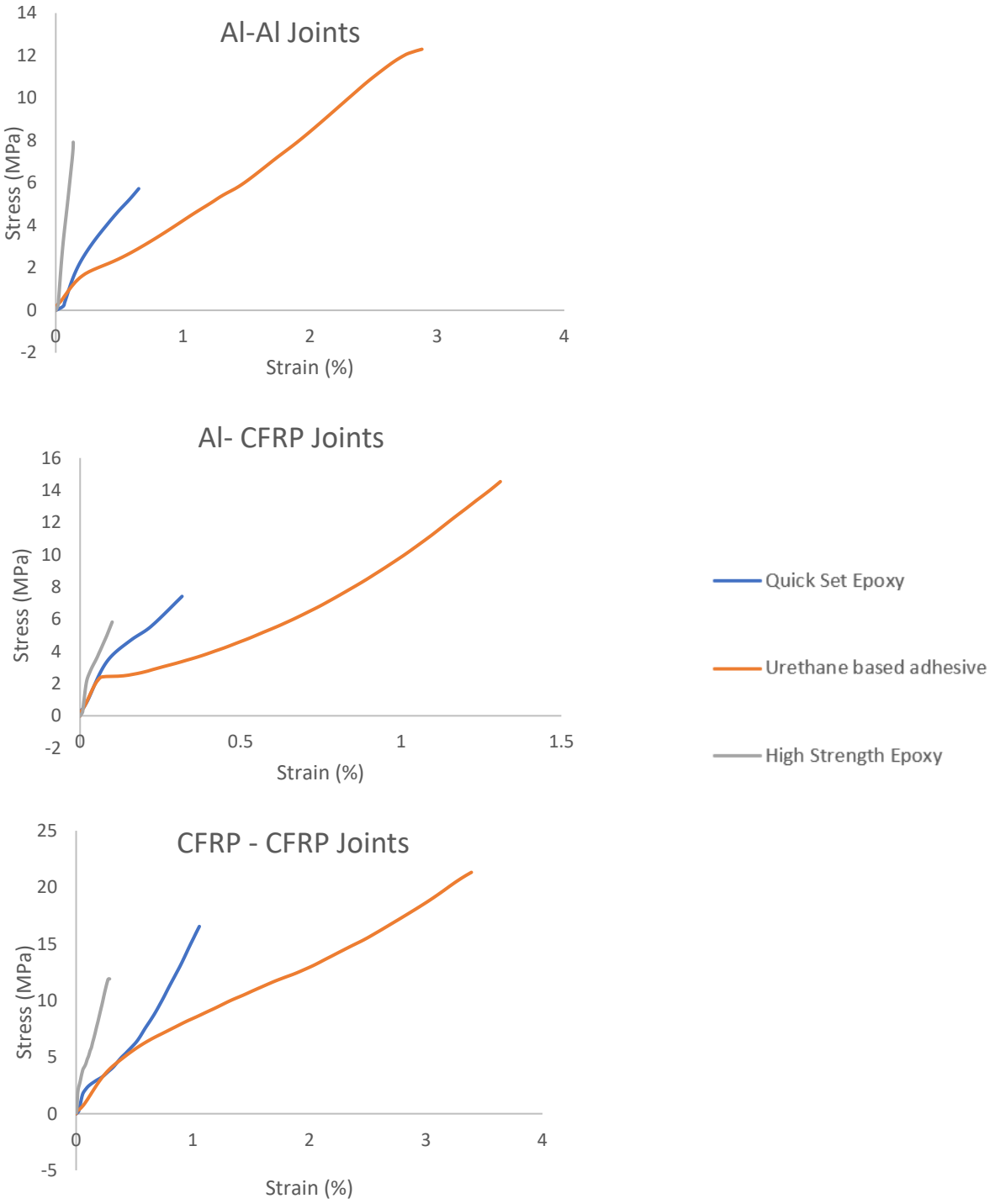


Figure 3.131 Typical stress vs strain graph for the single lap joints at a strain rate 0.15 $s^{-1}$.

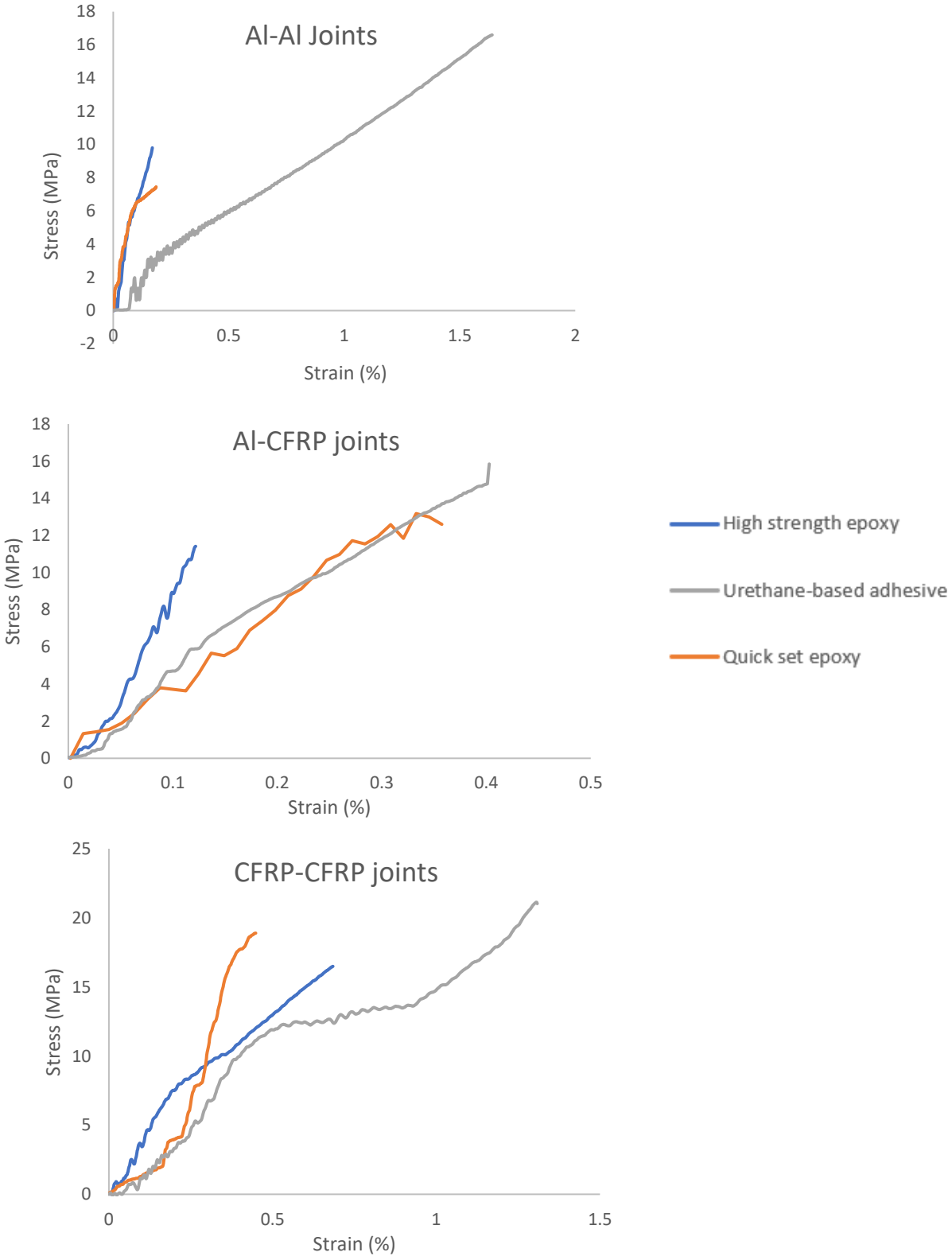


Figure 3.132 Typical stress vs strain graph for the single lap joints at a strain rate 15 $s^{-1}$.

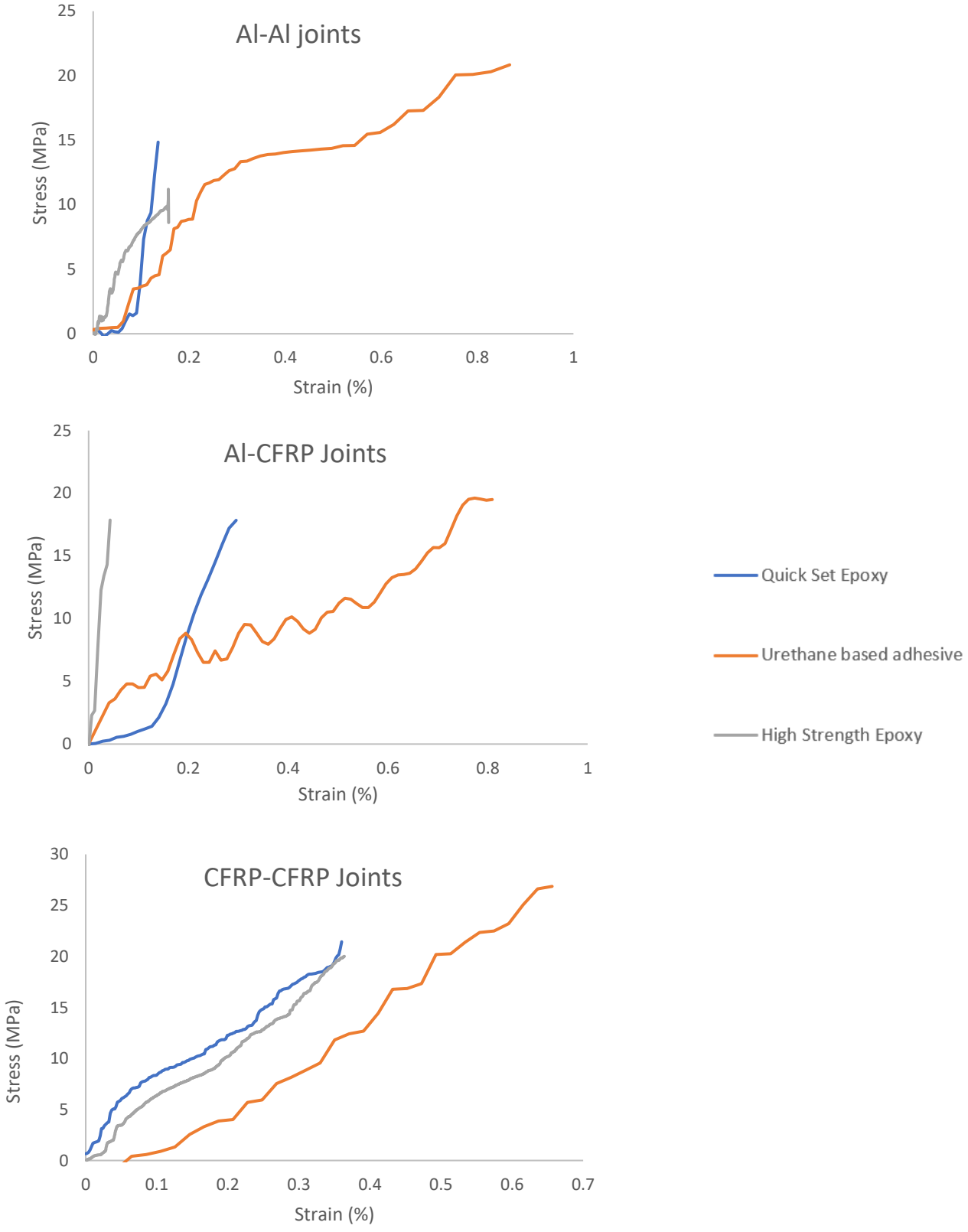


Figure 3.133 Typical stress vs strain graph for the single lap joints at a strain rate 150 $s^{-1}$.

From the figure 3.134, the graph depicts the effect of strain rate with Al-Al joints and it can be seen that with the increase in strain rate the lap shear strength increased in all the cases. Moreover, the effect of strain rate is more visible in quick set epoxy where the shear strength increased by double from strain rate 15 $s^{-1}$ and 150 $s^{-1}$. Similarly, from the figure 3.135, the effect of strain rate in Al-CFRP joints is presented and it can be seen that there is a significant increase in maximum loads in all the adhesive tested with the increase in strain rate. Figure 3.136 shows the effect of strain rate on the peak loads for CFRP-CFRP SLJs. This trend is even followed in composite joints as well. Furthermore, it was observed that the sensitivity to strain rate is least in composite joints. The maximum loads of the joint did not increase much in the dynamic loading conditions as it changed in quasi-static conditions. The error bars have been presented with regards to the three specimens tested in all the SLJ cases and it was observed that the urethane-based adhesive had the least error percentage. Similarly, the error percentage for the quick setting epoxy is more which might be due to the less work time provided by the adhesive which have resulted in the formation of voids during the curing cycle.

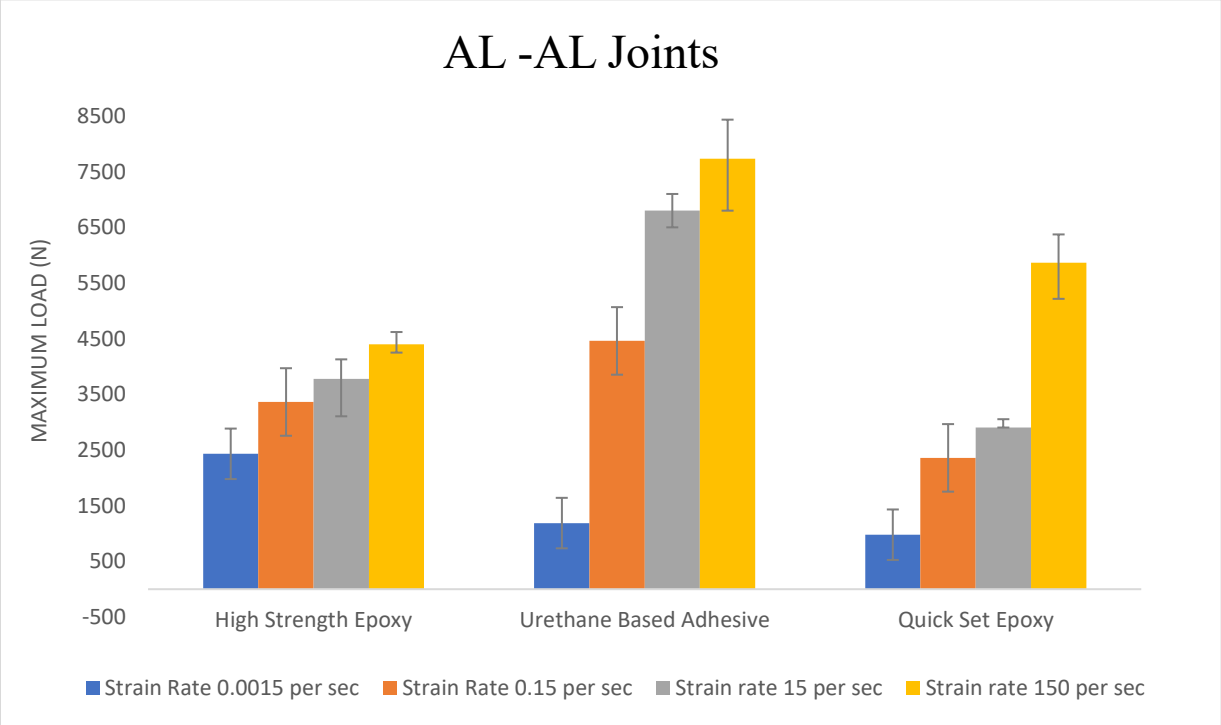


Figure 3.134 Effect of strain rate on the peak loads for Al-Al SLJs

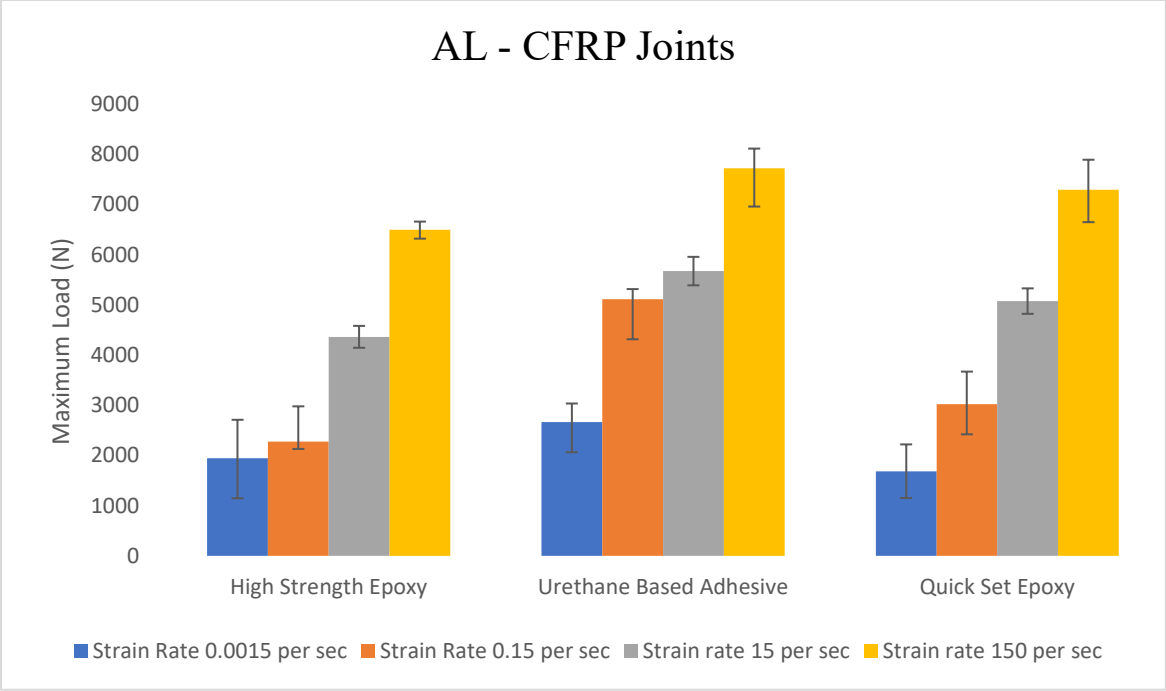


Figure 3.135 Effect of strain rate on the peak loads for Al-CFRP SLJs.

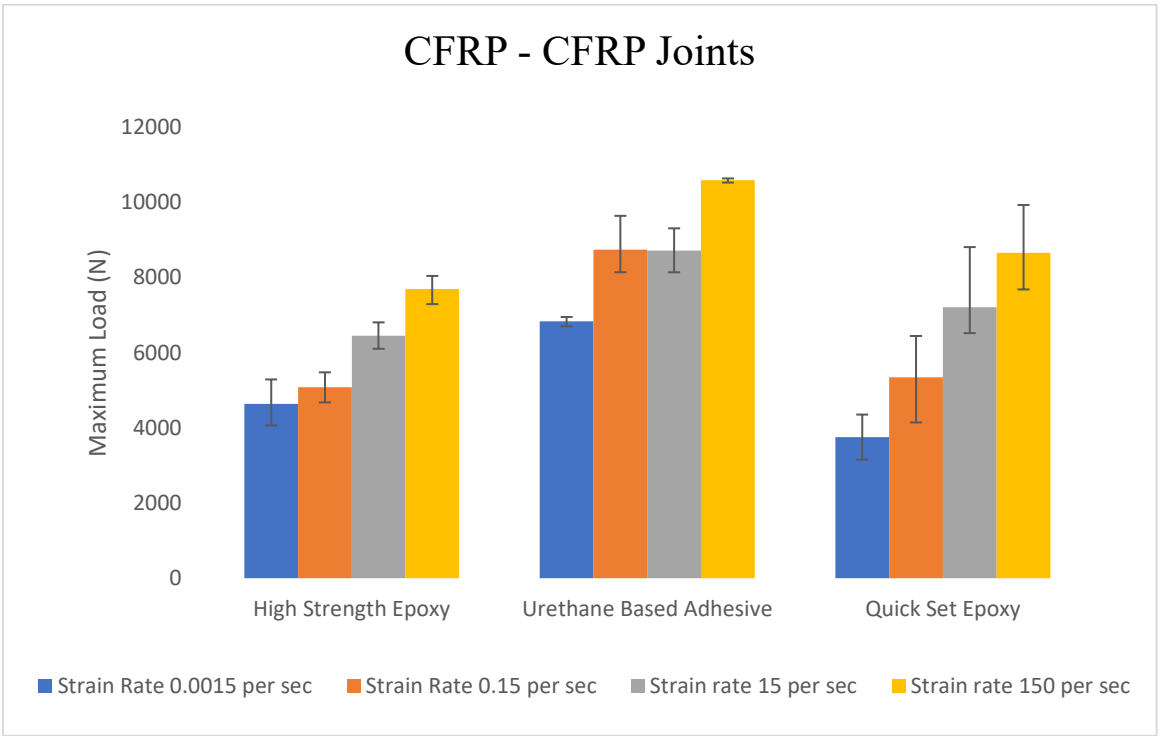


Figure 3.136 Effect of strain rate on the peak loads for CFRP-CFRP SLJs.

### 3.4 ANOVA Analysis

The ANOVA analysis of variance of the experimental results gives the understanding and significance of all the variables relative to one another. The main factors influencing the failure load are the strain rate (46 %), the substrate combination (31.74 %) and the adhesive type (14.21 %). The other resisul errors can be ignored as they are the variation amongst sampling units with each sample. It can be seen that the influence of strain rate is higher than the change in substrate combination or the adhesive type. In a similar way, an ANOVA analysis was performed on the peak strain values and it was seen that the adhesive type has the highest contribution on the peak strain (53 %) followed by the strain rate (15 %) and finally the substrate combination (6 %).

The main effect of substrate combination can be seen in the figure 3.137. As expected, the failure load increases with the adherend yield strength. Furthermore, as the adherend plastic deformation decreases, the adhesive can withstand higher shear stress and give a higher joint strength. Moreover, the means of peak strain has been observed to decrease with the increase in strain rate highlighting the behavior of adhesive nature with the increase in strain rate.

Figure 3.138 shows the means of failure load and peak strain are found to be higher for urethane-based adhesive. Furthermore, it was observed that the high strength epoxy had lower strength and strain at failure means than the quick set epoxy.

Figure 3.139 shows the effect of substrate combination on the means of failure load and peak strain and it can be observed that the maximum load capacity and strain at failure is higher for the composite joints. Furthermore, it can be seen that the dissimilar adherend combination had lower strain at failure which can be due to the eccentricity of the load path as a result of the difference in adherend stiffness.

Figure 3.140 shows the interaction plot for the maximum load with the change of substrate combination, adhesive type and strain rate. Here, the substrate 1 is Al-Al , Substrate 2 is Al-CFRP and substrate 3 is CFRP-CFRP and similarly adhesive type 1 is high strength epoxy, adhesive type 2 is quick set epoxy and adhesive type 3 is urethane-based adhesive. The figure highlights the effect of adherend combination, adhesive type and strain rate on the maximum load capacity of the joint.

Table 3.3 Analysis of variance (ANOVA) results for failure load.

| Source | DF | Adj SS | Adj MS | F-Value | P-Value | % of contribution |
|---|---|---|---|---|---|---|
| Substrate | 2 | 67559549 | 33779774 | 57.29 | 0.0000000000 | 31.74 |
| Adhesive Type | 2 | 30254809 | 15127404 | 25.66 | 0.0000000001 | 14.21 |
| Strain Rate | 3 | 98516090 | 32838697 | 55.69 | 0.0000004671 | 46.29 |
| Residual Error | 28 | 16509336 | 589619 | | 0.0000000000 | 7.76 |
| Total | 35 | 212839783 | | | | 100 |

Table 3.4 Analysis of variance (ANOVA) results for peak strain.

| Source | DF | SS | MS | F-Value | P- Value | % of contribution |
|---|---|---|---|---|---|---|
| Substrate | 2 | 1.506 | 0.7532 | 3.03 | 0.0640 | 5.78 |
| Adhesive Type | 2 | 13.773 | 6.8866 | 27.7 | 0.0000 | 52.88 |
| Strain Rate | 3 | 3.808 | 1.2693 | 5.11 | 0.0060 | 14.62 |
| Residual Error | 28 | 6.961 | 0.2486 | | | 26.72 |
| Total | 35 | 26.048 | | | | 100 |

DF, degrees of freedom; SS, Sum of squares; MS, Mean square

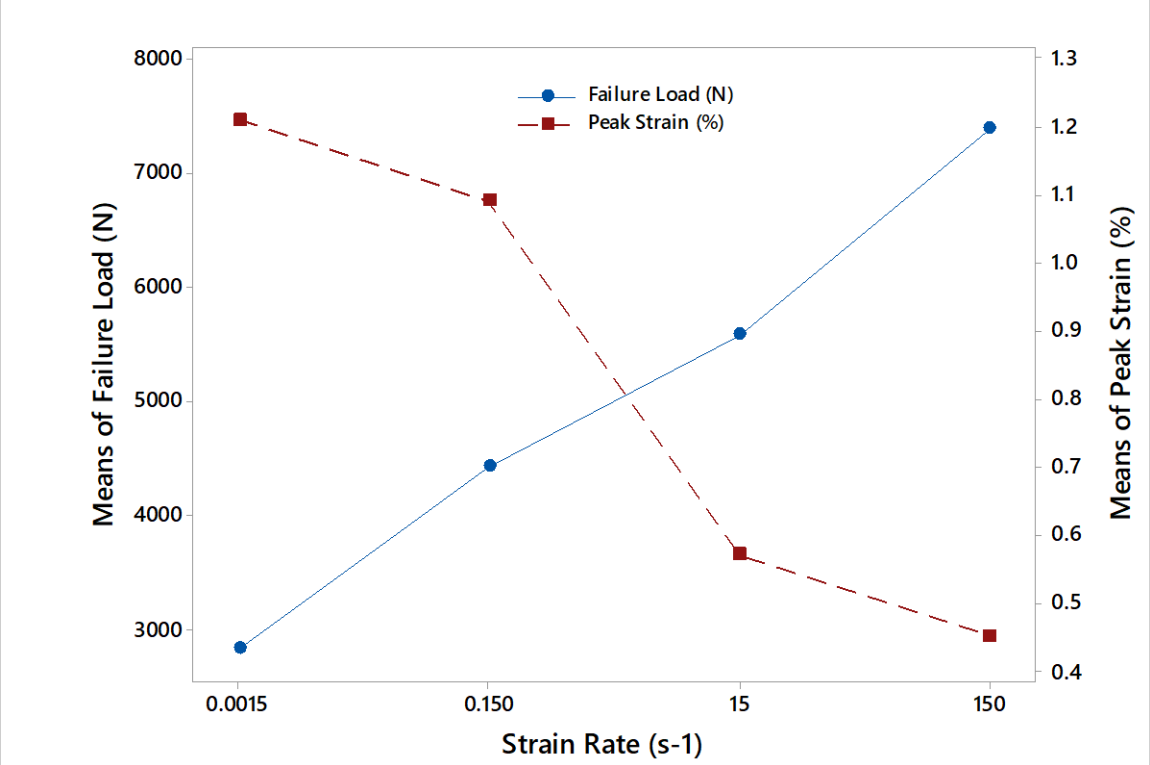


Figure 3.137: Response graph for the main effect of strain rate

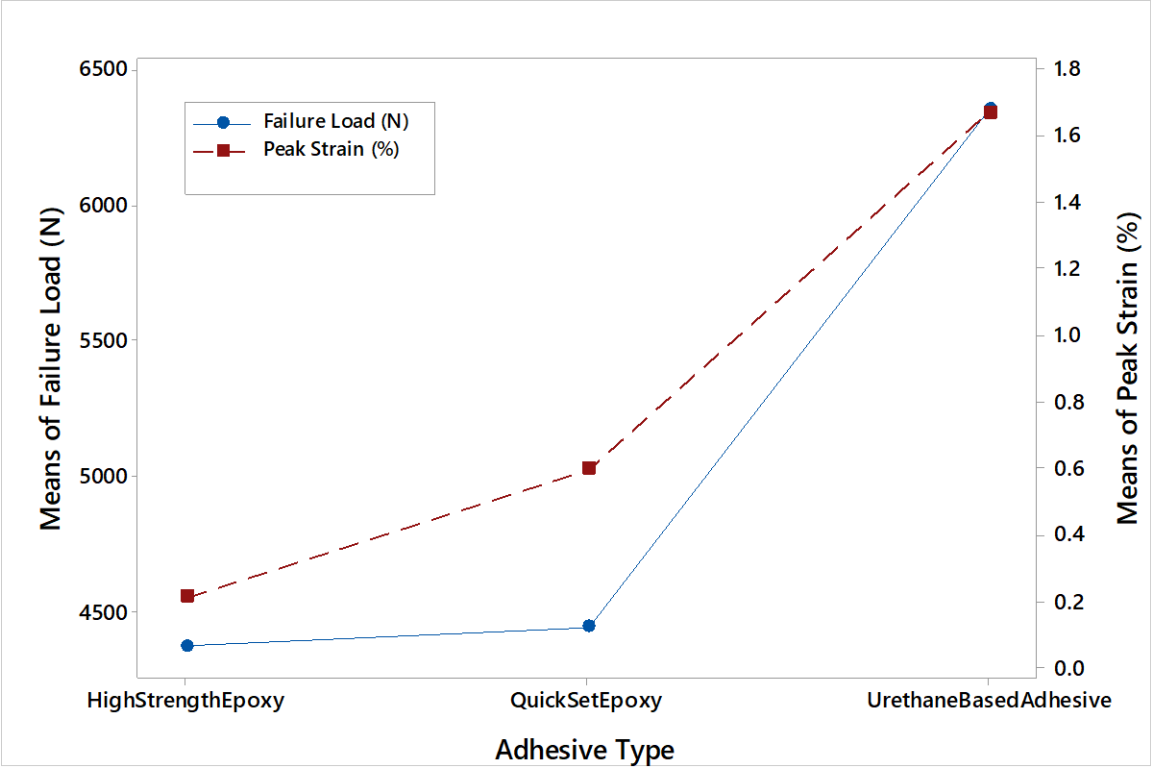


Figure 3.138: Response graph for the main effect of adhesive type

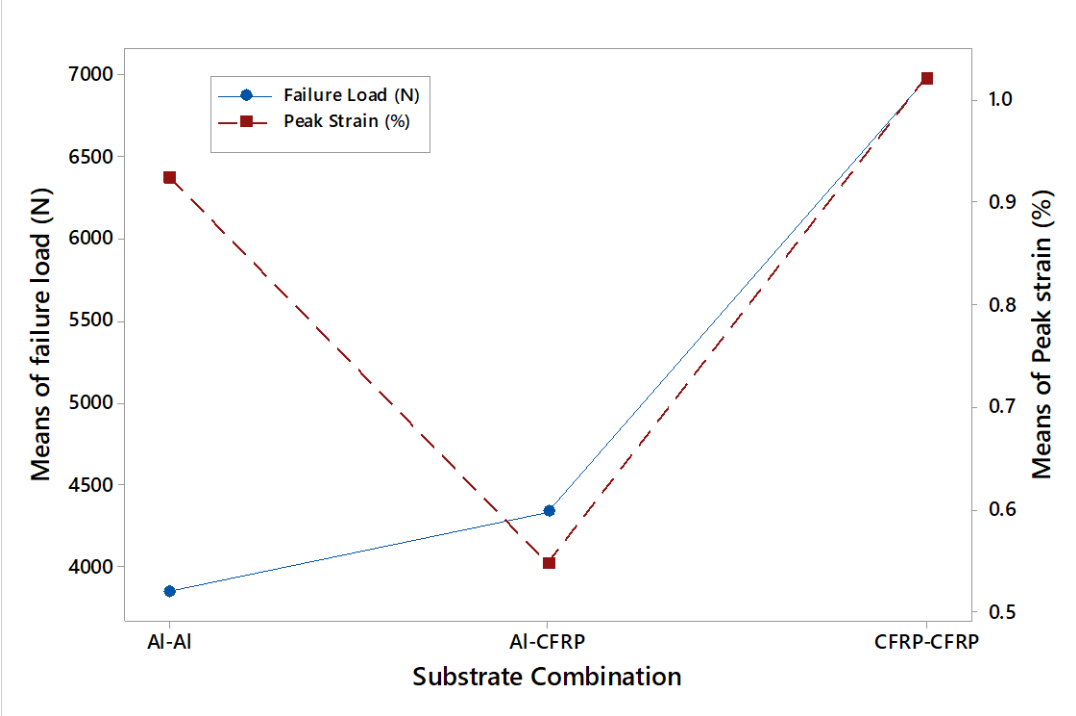


Figure 3.139: Response graph for the main effect of substrate combination.

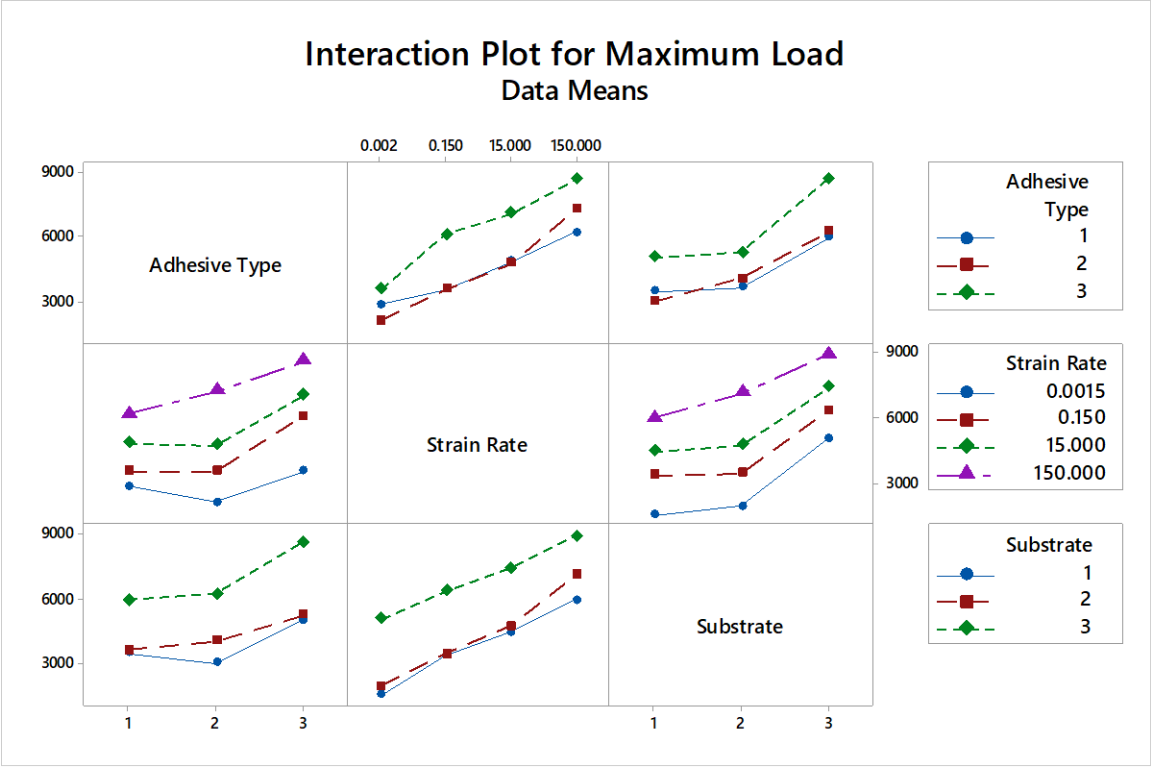


Figure 3.140: Interaction plot for the maximum load with respect to all of the variables.

# Chapter 4. Conclusions

The manufacturing and characterization of different adhesive with similar and dissimilar adherends was studied to understand the behavior of metal-metal, metal-composite and composite-composite joints. Two brittle adhesives and one ductile adhesive were chosen for bonding the joints. The joint fabrication and surface preparation were investigated, and a fixture was developed to control the adhesive thickness and to maintain the integrity of the lap joint. Later, these manufactured single lap joints were tested on a universal testing machine under quasi-static tensile loading at strain rates of 0.0015 $s^{-1}$ and 0.15 $s^{-1}$. The local and global strain deformation in the adhesive bond line was monitored using digital image correlation. Furthermore, dynamic testing was performed under tensile loading conditions at a strain rate of 15 $s^{-1}$ and 150 $s^{-1}$ using mechanical testing unit and the image sequence was captured using high speed cameras (APX-Photron) and examined with 2D Digital image correlation technique. The effect of adherend yield strength, adhesive type and test speed on the nominal shear strength, failure mode and peak strain were investigated using experimental setup. For the conditions tested, the following conclusion were drawn:

- In the initial study, it was found that the lap shear strength decreased when the adhesive thickness increased from 1 mm to 1.5 mm.
- The lap shear strength depends on the adherend yield strength of both the substrates and with the increase in yield strength of substrate combination there was an increase in shear strength (31.74% of contribution).
- The lap shear strength and peak strain is significantly higher when a flexible adhesive was used compared to brittle adhesive at higher strain rates.
- The thermal residual stresses induced in the aluminum and composite adherend when bonded with high strength epoxy had an effect on the lap shear strength.
- DIC investigations highlighted the strain localizations and distributions and its variations with strain rate. It was observed that the peak strain at failure decrease

with the increase in strain rate except when urethane-based adhesive is used to bond aluminum joints.

- Low magnification optical microscopy images of the fracture surface have revealed the failure modes and its variation with the strain rate. It was observed that with the increase in strain rate the cohesive failure within the substrate was more prominent in composite joints. In similar manner, the effect of strain rate in aluminum joints bonded with urethane-based adhesive has shifted from cohesive failure in adhesive to adhesive failure. Here, it was understood that this adhesive behaves in brittle nature at higher strain rates.
- All the adhesives used in this research project exhibited higher compatibility with the composite substrates resulting in higher peak loads and shear stresses.
- Finally, an ANOVA analysis highlighted the effect of stain rate on peak loads and adhesive type on peak strain.

# References


1. Yi, Xiao-Su, Du, Shanyi, Zhang, Litong (2017) Composite Materials Engineering, Volume 2: Different Types of Composite Materials [Book], 617.

2. NPTEL, Engineering Applications of Composite Materials, https://nptel.ac.in/courses/105108124/pdf/Lecture_Notes/LNm11.pdf

3. Composites lab (2016), ACMA, http://compositeslab.com/benefits-of-composites/strength/

4. Dobrzanski, Leszek & Włodarczyk, A & Adamiak, Marcin. (2005). Structure, properties and corrosion resistance of PM composite materials based on EN AW-2124 aluminum alloy reinforced with the Al2O3 ceramic particles. Journal of Materials Processing Technology. 162. 27-32.

5. V. Markova, A & F. Savin, V & B. Zharinov, Yu & Blaznov, A. (2011). Corrosion Resistance Tests of Strained Rods from Polymer Composite Materials. Inorganic Materials. 47.

6. Sutherland, Leigh. (2018). A review of impact testing on marine composite materials: Part III - Damage tolerance and durability. Composite Structures. 118.

7. Cantwell, W.J. & Morton, J. (1991). The impact resistance of composite materials - a review. Composites. 22. 347-362.

8. Premix (2009), advantages of composites, https://www.premix.com/why-composites/adv-composites.php.

9. NPTEL, Composite materials, https://nptel.ac.in/courses/Webcourse-contents/IISc-BANG/Composite%20Materials/pdf/Lecture_Notes/LNm1.pdf.

10. Mallick, P. K. (1993). Fiber-reinforced composites: Materials, manufacturing, and design. New York: M. Dekker.

11. A. Ibrahim, I & Mohamed, Farghalli & Lavernia, Enrique. (1991). Paniculate Reinforced Metal Matrix Composites—A Review. Journal of Materials Science. 26

12. Ramnath, Vijaya & Elanchezhian, C & Annamalai, R.M. & Aravind, S & Sri Ananda Atreya, T & Vignesh, V & Subramanian, C. (2014). Aluminium metal matrix composites - A review. Reviews on advanced materials science. 38. 55-60

13. Ru-Min Wang, Shui-Rong Zheng and Ya-Ping Zheng (2011) Polymer Matrix Composites and Technology, 2011, book, Woodhead Publishing, 568

14. J.M.G. Cowie and V. Arrighi, Professor Ian M. Ward (2009) Polymers: Chemistry and Physics of Modern Materials, 3rd edition, by Contemporary Physics, 50:6, 670

15. Amin, Salman & Amin, Muhammad. (2011). Thermoplastic elastomeric (TPE) materials and their use in outdoor electrical insulation. Reviews on Advanced Materials Science. 29.

16. Engels, Thomas. (2012). Thermoset adhesives: Epoxy resins, acrylates and polyurethanes.

17. Polymer science learning center (2003), Epoxy Resin, https://www.pslc.ws/macrog/epoxy.html

18. Zhou, Hengshi & Xu, Shi-Ai. (2014). A new method to prepare rubber toughened epoxy with high modulus and high impact strength. Materials Letters, 121, 238-240.

19. National Center for Biotechnology Information (2019) PubChem Compound Database; CID=114729, https://pubchem.ncbi.nlm.nih.gov/compound/114729

20. Park SJ. (2018) History and Structure of Carbon Fibers. In: Carbon Fibers. Springer Series in Materials Science, vol 210. Springer, Singapore.

21. Thermosets and Composites (2014) Material Selection, Applications, Manufacturing and Cost Analysis, Book, 2nd Edition

22. The Aluminum Association, Inc, December (1998) Aluminum Alloy Selection and Applications

23. Mechanica Technical Solutions (2014) Mechanical Fastening, https://www.mechanicatech.com/Joining/mechanicalfastening.html. [Online]

24. McCarthy, C & McCarthy, Michael. (2015). Design and failure analysis of composite bolted joints for aerospace composites, Polymer Composites in the Aerospace Industry, 11, 295-334

25. A Dzenis, Yuris & Qian, Jie. (2001). Analysis of Microdamage Evolution Histories in Composites. International Journal of Solids and Structures. 38. 1831-1854.

26. Chan, W. S., & Vedhagiri, S. (2001). Analysis of Composite Bonded/Bolted Joints Used in Repairing. Journal of Composite Materials, 35(12), 1045–1061.

27. Lucas F. M. da, Silva, Andreas O¨, chsner and Robert D., Adams, Handbook of Adhesion.

28. M. Moya-Sanz, Elena & Ivañez, Inés & García-Castillo, Shirley. (2016). Effect of the geometry in the strength of single-lap adhesive joints of composite laminates under uniaxial tensile load. International Journal of Adhesion and Adhesives. 72, 23-29.

29. State-of-the-art-adhesive-technology, https://www.theengineer.co.uk/supplier-network/product/state-of-the-art-adhesive-technologies-for-the-automotive-industry/.

30. Schneberger G.L. (1990) Adhesives in the Automobile Industry. In: Skeist I. (eds) Handbook of Adhesives. Springer, Boston, MA.

31. Diez de Ulzurrun I, Lopez F, Herreros MA, Suarez JC. Test of desk-to-hull.

32. Jun Cao, Joachim L. Grenestedt (2004) Design and testing of joints for composite sandwich/steel hybrid ship hulls, 35, 9, 1091-1105.

33. Godzmirski J (2002) The static strength of structural adhesive joint. Warsaw: Scientific and Technical Publishers.

34. Abdel Wahab, Magd. (2015). Joining composites with adhesives: theory and applications, Book.

35. James Renton, W & Vinson, Jack (1975) The Efficient Design of Adhesive Bonded Joints. Journal of Adhesion - J ADHES, 7, 175-193.

36. Ribeiro, T.E.A. & Campilho, Raul & Silva, L.F.M. & Goglio, Luca. (2016). Damage analysis of composite-aluminium adhesively-bonded single-lap joints. Composite Structures. 136. 25-33.

37. Sébastien Genty, Jean-Baptiste Sauvage, Philippe Tingaut, Maëlenn Aufray (2017) Experimental and statistical study of three adherence tests for an Poxyamine/ aluminum alloy system: Pull-Off, Single Lap Joint and Three-Point Bending tests International Journal of Adhesion and Adhesives, 50-58.

38. Yao, Mingxia & Zhu, Deju & Yao, Yiming & Zhang, Huaian & Mobasher, Barzin. (2016) Experimental Study on Basalt FRP/steel Single-lap joints under Different Loading rates and Temperatures, Composite Structures, 145, 68-79.

39. CHO, J. U (2013) High-strain-rate fracture of adhesively bonded composite joints in DCB and TDCB specimens, International Journal of Automotive Technology, 1127-1131.

40. Uday K. Vaidya, Abhay R.S. Gautam, Mahesh Hosur, Piyush Dutta (2006) Experimental–numerical studies of transverse impact response of adhesively bonded lap joints in composite structures, 26, 3, 184-198.

41. Halliday, S.T., Banks, W.M. and Pethrick, R.A (2000) Dielectric studies of adhesively bonded CFRP/epoxy/CFRP, Composites Science and Technology, pp. 197-207.

42. Banea, M & Silva, L.F.M. & Campilho, Raul. (2014). The Effect of Adhesive Thickness on the Mechanical Behavior of a Structural Polyurethane Adhesive. The Journal of Adhesion. 91.

43. Banea, M & Rosioara, M & Carbas, Ricardo & Silva, L.F.M. (2018). Multi-material adhesive joints for automotive industry. Composites Part B: Engineering. 151.

44. Ghanbari, Esmaeil & Sayman, Onur & Pekbey, Yeliz & Özdemir, Okan. (2015). Experimental analysis of single-lap composite joints with two different adhesives at various conditions, Journal of Composite Materials, 50.

45. Challita, Georges & Othman, Ramzi & CASARI, Pascal & Khalil, Khaled (2011) Experimental investigation of the shear dynamic behavior of double-lap adhesively

bonded joints on a wide range of strain rates. International Journal of Adhesion and Adhesives, 31, 146-153.

46. F. Stazi, M. Giampaoli, M. Rossi, P. Munafo (2015) Environmental ageing on GFRP pultruded joints: Comparison between different adhesives, 133, 404-414.

47. Anyfantis, Konstantinos & Tsouvalis, Nicholas (2013) Loading and fracture response of CFRP-to-steel adhesively bonded joints with thick adherents – Part I: Experiments. Composite Structures, 96, 850–857.

48. Yi-Ming Jen, Chih-Wei Ko. 2 (2010) Evaluation of fatigue life of adhesively bonded aluminum single-lap joints using interfacial parameters, International Journal of Fatigue, 32, 330-340.

49. Rachana Bhanushali, David Ayre and Hamed Yazdani Nezhad, Procedia (2017) Tensile Response of Adhesively Bonded Composite-to-composite Single-lap Joints in the Presence of Bond Deficiency, 139-143.

50. Akhavan-Safar, A., Silva, L.F.M. da and Ayatollahi, M.R (2014) An investigation on the strength of single lap adhesive joints with a wide range of materials and dimensions using a critical distance approach, International Journal of Adhesion and Adhesives, 248-255.

51. W R,Grower, M R L. (2001) Preparation and testing of adhesive joints. Broughton, Measurement Good Practice Guide No. 47.

52. Lucas. F.M.da Silva, R.J.C. Carbas, G.W.Critchlow, M.A.V. Figueiredo, K.Brown (2009) Effect of material, geometry, surface treatment and environment on the shear strength of single lap joints, International Journal of Adhesion & Adhesives, 29, 621-632.

53. Silva, L.F.M. & Adams, R. (2006). Techniques to reduce the peel stresses in adhesive joints with composites. Int J Adhes Adhes, 27, 3, 277-235.

54. Adhesive & Sealants overview, https://www.adhesives.org/adhesives-sealants/adhesives-sealants-overview.

55. S, Ebnesajjad (2009) Adhesives Technology Handbook - Second Edition. Norwich, NY: William Andrew Publishing, Book.

56. Banea, M. D., and da Silva L.F.M. (2009) Adhesively Bonded Joints in Composite Materials: An Overview. Proceedings of the Institution of Mechanical Engineers, 223, 1-18.

57. ASTM D5573-99(2012) Standard Practice for Classifying Failure Modes in Fiber-Reinforced-Plastic (FRP) Joints, ASTM International, West Conshohocken, PA, 2012.

58. Tae-Hwan Kim, Jin-Hwe Kweon, Jin-Ho Choi (2008) An Experimental Study on the Effect of Overlap Length on the Failure of Composite-to-Aluminum Single-Lap Bonded Joints, 10, 27, 1071-1081.

59. ASTM International (2010) ASTM D1002-10, Standard Test Method for Apparent Shear Strength of Single-Lap-Joint Adhesively Bonded Metal Specimens by Tension Loading (Metal-to-Metal). West Conshohocken, PA.

60. ASTM International (2014) ASTM D5868-01, Standard Test Method for Lap Shear Adhesion for Fiber Reinforced Plastic (FRP) Bonding. West Conshohocken, PA.

61. Araújo, Helder, André Moreira (2016) Impact and damping behavior of composite adhesive joints.

62. YingYan, Jianfeng Li n, Zhang, Taotao and Liang, Zudian (2015) Experimental study of adhesively bonded CFRP joints subjected to tensile loads. International Journal of Adhesion & Adhesives, 95-104.

63. A. Ilionia, C. Badulescu, N. Carrere, P. Davies, D, Thevenet (2018) A viscoelastic-viscoplastic model to describe creep and strain rate effects on the mechanical behaviour of adhesively-bonded assemblies. International Journal of Adhesion and Adhesives, 82, 184-195.

64. Louise A. Powell, William E. Luecke, and Matthias Merzkirch (2017) High Strain Rate Mechanical Characterization of Carbon Fiber Reinforced Polymer Composites Using Digital Image Correlations, SAE Journal.

65. Debora C Moreira, Luiz CS Nunes (2014) Experimental analysis of bonded single lap joint with flexible adhesive, Applied Adhesion Science.

66. B. Riggs, A. Benatar, B. T. Alexandrov, R. Xu (2017) Experimental Validation of Damage Zone Models for Lap Shear Brazed Joints Using DIC, American Welding Society, 96, 421-428.

67. A.J. Comer, K.B.Katnam, W.F.Stanley, T.M.Young (2013) Characterizing the behavior of composite single lap bonded joints using digital image correlation. International Journal of Adhesion and Adhesives, 40, 215-223.

68. Guangyong Suna, Xinglong Liua, Gang Zhenga, Zhihui Gonga, Qing Lib (2018) On fracture characteristics of adhesive joints with dissimilar materials – An experimental study using digital image correlation (DIC) technique, 201, 1056 - 1075.

69. Manes, Andrea & Pagani, M & Saponara, Matteo & Mombelli, Davide & Mapelli, C & Giglio, Marco (2014) Metallographic characterisation of Al6061-T6 aluminium plates subjected to ballistic impact, Materials Science and Engineering, 608, 207–220.

70. Mc Master Carbon Fiber, sheet, https://www.mcmaster.com/8181k34.

71. Apache license (2018) Digital image correlation, digitalimagecorrelation.org.

72. GOM optical measuring techniques (2009) ARAMIS v6.1 and higher, Aramis User Manual- Software.

73. Ahmadreza Hedayat, Suleiman Ashur (2015) Digital image correlation and its application in an undergraduate Civil Engineering Materials Laboratory.

74. Yan, B & Kuriyama, Y & Uenishi, A & Cornette, D & Borsutzki, M & Wong, C. (2006). Recommended Practice for Dynamic Testing for Sheet Steels - Development and Round Robin Tests.

75. Venkata Naga Prakash Mallik Pariti (2017) Mechanical Behavior of Carbon and Glass Fiber Reinforced Composite Materials Under Varying Loading Rates, Master's thesis, University of Michigan, Dearborn.

76. Deju Zhu, Barzin Mobasher, and Subramaniam D. Rajan (2011) Dynamic Tensile Testing of Kevlar 49 Fabrics, Journals of materials in Civil Engineering, 3, 23.

77. Abbott, Steven (2015) Adhesion Science: Principles and Practice, DEStech Publications, Inc, 328.

78. Jumbo, F., Ruiz, P. D., Yu, Y., Swallowe, G. M., Ashcroft, I. A. and Huntley, J. M. (2007), Experimental and Numerical Investigation of Mechanical and Thermal Residual Strains in Adhesively Bonded Joints, 43: 319-331.

79. Hausmann, Joachim & Naghipour, Paria & Kotzur, Karola. (2013). Analytical and Numerical Residual Stress Models for Fiber Metal Laminates – Comparison and Application. Procedia Materials Science, 2, 68–73.

80. Wang, Changchun & Yue, Guidong & Zhang, Jiazhen & Liu, Jianguang & Li, Jin. (2016). Formation and the effects of the thermo-residual stress on mechanical properties of the thermoplastic composites. Advances in Intelligent Systems Research, volume 136.